Spring 1-1-2012

First Order Feasibility Evaluation of a Water-Based Freezable Heat Exchanger for Use in Human Spacecraft Thermal Control

Joshua B. Hecht
University of Colorado at Boulder, jinxerjb@gmail.com

FIRST ORDER FEASIBILITY EVALUATION OF A WATER-BASED FREEZABLE HEAT EXCHANGER FOR USE IN HUMAN SPACECRAFT THERMAL CONTROL

by

JOSHUA B. HECHT

B.S., University of Colorado, 2011

A thesis submitted to the

Faculty of the Graduate School of the

University of Colorado in partial fulfillment

of the requirement for the degree of

Master of Science

Department of Aerospace Engineering

2012

SIGNATURE PAGE

This thesis entitled:
First Order Feasibility Evaluation of a Water-Based Freezable Heat Exchanger for Use in Human Spacecraft Thermal Control
written by Joshua B Hecht
has been approved for the Department of Aerospace Engineering

Dr. David Klaus

Dr. James Nabity

Date: 12/7/12

The final copy of this thesis has been examined by the signatories, and we find that both the content and the form meet acceptable presentation standards of scholarly work in the above mentioned discipline.

ABSTRACT

Hecht, Joshua B. (M.S., Aerospace Engineering Sciences, 2012)

First Order Feasibility Evaluation of a Water-Based Freezable Heat Exchanger for Use in Human Spacecraft Thermal Control

Thesis directed by Associate Professor David M. Klaus

A spacecraft thermal control system must keep the cabin and electronic equipment within operational temperature ranges by transporting heat out of the spacecraft. This process is generally accomplished via a series of air-to-liquid heat exchangers with ultimate dissipation to space via radiator panels, and requires various flow regulation schemes to maintain the desired thermal balance. In contrast, a proposed self-regulating freezable heat exchanger is designed to passively maintain and regulate thermal control through water ice buildup within the heat exchanger structure. In order to determine the feasibility and effectiveness of this technology, an integrated analysis of the thermal loads encountered by an orbital spacecraft was conducted. The analysis determines the expected internal and external heat loads on the spacecraft, outlines potential implementation of the hardware into the thermal control system, and predicts the expected performance of the technology. The results attained partially validate the capability of the self-regulating freezable heat exchanger to reject the anticipated range of heat loads. Additional testing will be conducted to further asses the full capabilities of the design. The full test and subsequent results will allow a detailed performance analysis to ultimately establish the feasibility of and options for incorporating the

self-regulating freezable heat exchanger into a spacecraft thermal control architecture.

ACKNOWLEDGMENTS

I would like to acknowledge Dr. David Klaus for providing invaluable guidance in the research. The assistance he provided in the creation of this document, and the accompanying presentations was tremendous.

I would like to acknowledge Dr. James Nabity for providing me the characteristics, descriptions, and understanding of his technology. He was always at the ready to assist me in my understanding, and provided excellent suggestions in terms of research and how to proceed with the analysis.

I would like to acknowledge Dr. Jeffery Thayer for his presence on my thesis committee, and for being my thermodynamics instructor in 2008. His class provided a solid foundation for the research on this technology.

This work was funded by a NASA STTR Phase 1 (T6.01-9863: A Self-Regulating Freezable Heat Exchanger for Spacecraft) under subcontract to TDA Research Inc.

CONTENTS

TABLES

Table

FIGURES

Figure

CHAPTER I

INTRODUCTION

Spacecraft typically experience a wide range of heat loads during the course of a full orbit. A spacecraft in the sunlit (dayside) portion of the orbit will experience a hot thermal environment, due to the energy transfer from the incident solar radiation combined with Earth's albedo and infrared (IR) energy. The same spacecraft in eclipse (nightside) will experience a cooler thermal environment, since the Earth eclipses the solar radiation from the spacecraft surface. This pattern of variable heat loads is typical of spacecraft in Low Earth Orbit (LEO), since most (but not all) LEO spacecraft go between Sun and eclipse throughout a full orbit. The cyclical heat loads can cause the spacecraft temperature to vary from well below freezing to warmer than room temperature. The change in temperature is related to the magnitude of the incoming heat loads, as well as the spacecraft's size, shape, and thermal properties (Brown, 2002). Since spacecraft must keep the cabin air and avionics within a narrow range acceptable of operational temperatures, the thermal balance must be controlled while on orbit around the Earth.

One of the primary factors to consider in spacecraft design is thermal control. Thermal control is a means of regulating the heat load into and out of the spacecraft cabin boundary. The heat load must be regulated to keep the crew, electronics, and payloads within operational temperature limits. The spacecraft maintains thermal control by utilizing processes that absorb, transport, and ultimately reject heat from the spacecraft (Bylander, 2010). A spacecraft in a variable thermal environment

should have hardware that is capable of providing variable rates in its heat rejection system.

Spacecraft Application of a Variable Output Heat Exchanger

Thermal environments are defined by the heat loads going into and out of the spacecraft (Akin, 2009). As the heat loads are absorbed by the spacecraft, portions of the spacecraft build up thermal energy and will increase in temperature, unless the heat is rejected. Heat rejection is the transfer of thermal energy away from the spacecraft. If the heat rejected from the spacecraft equals the amount of heat coming into the spacecraft, the net heat flux is zero. This condition is called "thermal equilibrium" and is achieved when all temperatures of interest in the spacecraft remain within specified tolerances throughout the mission profile (Kondepudi, 2008).

Human rated spacecraft must maintain a nearly stable cabin temperature, since humans are relatively sensitive to temperature changes. With most LEO spacecraft, the heat load is variable, which can cause rapid increases or decreases in temperature if not controlled. In order to keep the spacecraft within specified temperature limits, an Active Thermal Control System (ATCS) is required to actively manage the heat loads. The ATCS regulates the heat loads through heat exchanger and heat sink technology onboard the spacecraft. In this study, a variable output heat exchanger was evaluated in its capability to maintain thermal equilibrium onboard a human rated spacecraft under varying thermal environments.

Heat Exchanger

Heat is rejected out of the spacecraft through heat exchanger and heat sink technology. The ATCS is responsible for transferring thermal energy from regions of high temperature to regions of low temperature (Bulut, 2008). The final regions of low temperature are called "heat sinks", and are used to absorb and reject the heat loads from the spacecraft (Bulut, 2008). While there are many options for heat sink technology, the analysis will be primarily focused on radiators and Phase Change Materials (PCM).

If the heat sinks dissipate heat equal to the incoming heat load, the spacecraft has attained thermal equilibrium. The ATCS transfers heat loads to heat sinks through heat exchangers. Liquid-based heat exchangers are typically used in human rated spacecraft (Wieland, 2005). Liquid-based heat exchangers absorb the heat loads into a working fluid, and transport the accumulated energy to heat sinks.

Most heat exchangers contain a working fluid that remains in its liquid phase as it transports heat. If the liquid freezes, it could block the flow path of the heat exchanger, preventing the heat from being transported. If the liquid evaporates, the pressure buildup could rupture the heat pipe (Leimkuhler et. al, 2010). Therefore, the melting and freezing points of the working fluid must be considered in conjunction with the environment the fluid is exposed to. Designs such as the International Space Station (ISS) and Space Transportation System (STS) use two heat exchangers with two separate working fluids, one for the hotter

interior, and one for the cold radiator surface. The properties for each system are listed in Table 1 (Hanford, 2006).

Table 1: Heat Exchanger Working Fluids

System	Working Fluids	Freezing Points (°C)	Boiling Points (°C)	Specific Heat Capacities (J/g*C)
ISS	Water/Ammonia	0 / -78	100 / -33	4.18 / 4.52
STS	Water/Freon	0 / -183	100 / -37	4.18 / 0.87

Water is used on the interior of both systems, since it has a high heat capacity, is non-toxic, and stays in its liquid phase when exposed to the relatively hot (~20 °C) cabin (Hanford, 2006). The heat from the water is absorbed by the fluid within the secondary loop. The secondary loop contains fluid with properties that prevent freezing when exposed to the relatively cold (~ -50 °C) radiator (Hanford, 2006). The secondary loop transports the heat load to the heat sink to be rejected by the spacecraft radiators.

Self-Regulating Freezable Heat Exchanger

Though the majority of heat exchangers contain a liquid phase working fluid, a new design has been developed that allows for the working fluid to freeze within the heat exchanger without blocking the fluid from flowing through. TDA Research, Inc. has created a Self-Regulating Freezable Heat Exchanger (SRHX) utilizing a water-based PCM within the heat exchanger (Nabity, 2008). The SRHX is unique in that water is simultaneously used as the working fluid and the PCM within the tube. In most heat exchangers, the water freeze is undesirable since it would block the flow path, and the expansion would rupture the heat exchanger pipe. The SRHX

allows for water to continue flowing even with ice formed in the loop by including an insulated path that prevents freezing in that portion of the SRHX (Nabity, 2008). The design allows for the volumetric expansion of ice without structural damage.

The ice freeze leads to three consequences. First, thermal energy is stored within the ice, which can be harnessed to buffer excess heat loads from the spacecraft when it is re-melted. Secondly, the ice reduces the net flow area the water is allowed to pass through, causing an increase in pressure across the heat exchanger. Lastly the ice freeze covers up a portion of the fins inside the heat exchanger, thereby regulating the conductive transfer of heat out of the working fluid to the outer shell.

The ice buildup occurs passively within the SRHX as a function of the inlet temperature, heat load and flow rate. For this reason, the SRHX is described as "self-regulating" since it controls the amount of heat absorbed without any active control components needed. The ice buildup occurs as a function of the net thermal balance, with more ice forming in cold conditions where a minimal amount of heat needs to be rejected from the spacecraft, and with no ice present in maximal heat loads (Nabity, 2008).

The properties of the SRHX could be utilized in a human rated spacecraft either as a thermal buffer or a passive water flow regulator. For human rated spacecraft in an orbit that experiences an eclipse, a variable external heat load will be imposed. Since the SRHX is self-regulating, thermal equilibrium can be passively maintained for a variety of heat flux values, thus simplifying the design. Also, since

the SRHX utilizes water as the working fluid, it offers a safe option that can be used within the cabin and in the external environment, potentially eliminating the need for a second fluid loop in the system. Finally, the ice-water phase change provides a thermal energy storage buffer that may allow the radiator size to be reduced, thus potentially decreasing the total mass of the spacecraft as a consequence.

Purpose

Determine if the self-regulating freezable heat exchanger is a *feasible* and *effective* technology to implement in a spacecraft active thermal control system.

The two keywords within the purpose statement are: feasible and effective. The feasibility of the SRHX is based on the capability of utilizing water as the working fluid, and the SRHX capability to self-regulate its heat rejection through ice buildup. The feasibility of using water will be determined if the SRHX hardware can reject heat loads across the expected range of thermal environments while remaining undamaged during its freeze and thaw cycles. The self-regulation aspect is evaluated through the steady state heat rejection capabilities of the SRHX. This will be assessed through the following aims:

Aim 1. Determine the typical heat load of a human rated spacecraft in LEO

The thermal loads were established for typical LEO profiles with representative metabolic and avionic heat loads. The predicted thermal loads were used to determine the range of heat loads that the SRHX must reject.

Aim 2. Evaluate the possible means of implementing the SRHX into the spacecraft ATCS

The orbital heat loads were used to predict the theoretical temperatures and mass flow rates through the SRHX as the spacecraft propagates through its orbit. The hardware limitations were used to determine where the SRHX can be implemented within the ATCS architecture.

Aim 3. Theoretically predict the steady state outputs of the SRHX

The steady state prediction applies constant inputs to the SRHX model until a constant output is maintained. The inputs to the model are: mass flow rate of water flowing through the SRHX, inlet temperature of the water, and outer wall temperature of the SRHX. The outputs of the model are the water outlet temperature, ice presence within the SRHX, and pressure difference. The inputs used to predict the SRHX outputs were based off the ATCS architecture predictions, the range of the predicted thermal loads, and the required cabin air temperature. Four sets of SRHX outputs were predicted, based on required heat load rejection, thermodynamic equilibrium, and previous testing data. The four sets of data are compared to one another to show the variable range in results from the different methods.

Aim 4. Compare the SRHX model versus test results under theoretical Scenarios to assess feasibility

The SRHX hardware was to be physically tested with the same inputs as the theoretical models to compare the test outputs the predicted results. However, the

full tests were not completed by the time of writing of this thesis. Only a set of preliminary tests were conducted with the desired hardware, and the inputs to the preliminary tests were used as inputs to the theoretical models. The outputs of the physical test and the corresponding predictions were compared to one another.

Once the full set of tests are complete, the difference between the actual and predicted results can potentially be used for an efficiency, or weighting factor in the models. Based on the full test results the feasibility of the SRHX can be validated for the predicted LEO heat loads and ATCS inputs.

Aim 5. Evaluate the effectiveness of utilizing the SRHX within the spacecraft

The effectiveness of the SRHX was based on whether the SRHX provides a net benefit to the ATCS (and overall spacecraft) versus existing technology. The benefit can be in mass savings, simplifying the overall architecture, or by making the system safer and more reliable. Mass savings can occur either through heat exchanger alternate architectures that potentially eliminate the need for a second external coolant flow loop, or through radiator size reduction. The size of the radiator can potentially be reduced by using the water as a PCM to buffer a portion of the heat load that would otherwise be rejected by the radiator. Simplifying the overall ATCS architecture occurs by removing or downsizing the baseline ATCS components if the SRHX is implemented in an alternative ATCS architecture. The ATCS might be considered safer if ammonia mass is reduced, or taken out entirely of the ATCS architecture. A preliminary equivalent system mass (ESM) was created

to compare the mass, complexity, and safety of each potential architecture for SRHX use. The ESM was used to determine whether the SRHX provides sufficient benefits to consider it an effective technology to implement in a spacecraft ATCS

After the steady state testing is complete, the self-regulation aspect will be assessed by dynamically varying the inlet temperature or mass flow rate. This will be used to determine the rate of ice melt and formation, and how it affects the rate of heat rejected from the SRHX.

Scope

For purposes of simplification, the evaluation will focus on spacecraft in low Earth orbit (LEO). Most human rated spacecraft to date have been designed for use in LEO (NASA, 2005). Heat loads in LEO can vary greatly, especially in orbits where the spacecraft goes into eclipse for a portion of the orbit. The SRHX accounts for this variability by allowing the heat rejection to be regulated through ice melt and freeze.

This study assumes that the spacecraft is in a circular, polar orbit around the Earth. These assumptions allow for evaluation of a typical range of heat loads encountered by a LEO spacecraft, both in the Sun and in eclipse, to be predicted for parametric analysis. Originally, the intent was to assess orbits from 250 kilometers to 750 kilometers, and beta angles from 0 º to 90 º. However, time constraints and limited hardware testing availability indicated that only one orbit would be necessary to model expected performance from the SRHX as a first order assessment, as long as the orbit demonstrated maximal heat load variability.

Therefore, the scope was limited to one orbit at a height of 350 kilometers, and a beta angle of 0 º.

Common ATCS architectures utilize water and ammonia as the working fluids for heat transfer. Water is the working fluid with the SRHX, and ammonia is a representative coolant that may be utilized in a secondary heat exchanger external to the crew habitat. While other working fluids have been used in past designs, water and ammonia are likely to be utilized in future missions, due to their low toxicity and high specific heat (Hanford, 2006).

For this study, only human rated spacecraft will be evaluated for SRHX use. The SRHX could conceivably be used for unmanned satellite thermal control as well, but the focus here is limited to the temperature ranges, heat loads, and ATCS architectures typical of human rated spacecraft.

Data Limitations

The orbital analysis was limited to LEO circular polar orbits. The effectiveness of the SRHX will not be based on eccentricity, even though the amount of time in eclipse and Sunlight can be significantly altered with non-circular eccentricities (Curtis, 2005). The assumed eccentricity of zero provides typical orbital parameters for human rated spacecraft (Wertz and Larson, 1999). Inclinations other than 90º will not be evaluated either. A polar inclination was originally chosen for iterative purposes, but was kept limited to single-orbit analysis. The inclination (mostly) does not affect the heat loads, nor the time in the

Sunlit or eclipse portions of the orbit. (Wertz and Larson, 1999). Therefore, a polar orbit is suitable for use in predicting variable orbital heat loads

The study did not take atmospheric heating into account. While spacecraft drag and heating is a factor in LEO, it is assumed that these loads are insignificant compared to the environmental heat loads (Wertz and Larson, 1999).

The heat load sources are considered to have a constant intensity, though the heat flux from the Sun, Earth, and internal heat loads can vary in time (Williams and Palo, 2006).

Extra vehicular activities, interplanetary transfers, and reentry conditions will not be evaluated for SRHX use. It has been hypothesized that the SRHX could be utilized in these applications as well, however characterizing the heat loads and PCM response from those conditions is outside the scope of the analysis.

The thermal mass of the spacecraft was not taken into account during the study. This assumption allows for the heat load coming into the spacecraft to be instantaneously transported to the cabin environment and transferred to the heat sink. In reality, there would be thermal lag associated with the heat loads on orbit, which creates a temperature gradient as the heat flows through the spacecraft (Van Outyrve, 2008). For the purposes of heat exchanger design, the heat was assumed to instantaneously pass through the spacecraft.

A limited number of dynamic tests were run to characterize the response of the SRHX to various conditions. While the data did give enough information to refine the analysis, and to modify the theoretical response, only the steady state

response was studied. Ultimately, detailed dynamic tests are needed to fully verify the use of the SRHX under variable heat load conditions.

Other Limitations

The heat transfer efficiencies throughout the ATCS are material and spacecraft dependent, and cannot be accurately modeled with a generic spacecraft as used for this study. The test results will provide representative values for the SRHX technology to be evaluated against, but all other spacecraft efficiencies must be assumed.

Arrangement of Thesis

The thesis begins with a background description of spacecraft heat load modeling and dissipation processes. The background also describes the dynamics of the SRHX through freezing and melting, along with potential means of SRHX implementation.

The parametric system analysis provides the methodology and results of orbit modeling, and architecture implementation. The results are compared to previous data to validate the models. The performance equations for the outlet temperature and pressure change from SRHX testing are investigated and presented.

The testing and analysis section describes the test plan and preliminary results of the SRHX hardware evaluation. The testing environment, conditions, and outputs are described, along with the results of the predicted performance of the SRHX. Test data are compared to the theoretical results to help determine if the SRHX is a feasible technology to implement in a spacecraft ATCS under these

conditions. A simplified equivalent system mass analysis is presented, which discusses the potential net mass impact, complexity, and safety considerations for each architecture option described. This approach is suggested to determine whether the SRHX is an effective technology to implement in a spacecraft ATCS.

The thesis is concluded by summarizing the results of the analysis and testing, and suggesting further research and possible improvements to the hardware and test protocol.

CHAPTER II

BACKGROUND

The primary forms of heat transfer are identified and discussed. The LEO thermal environment is modeled to determine the theoretical heat flux into a predefined spacecraft. The heat flux is dissipated out of the spacecraft through ATCS component selection. Each heat sink component has pros and cons that pertain to its particular mission environment. The primary heat sink technology of interest is via spacecraft radiators with potential PCM buffering within the SRHX. The SRHX structure and fundamental capabilities are described, along with its unique self-regulating thermal control. Potential architectures where the SRHX can be implemented are considered and compared to other human rated spacecraft.

Heat Transfer

Heat is defined as the transfer of energy over time by thermal interaction (Incropera, et al. 1985).

$$Q = \frac{dE}{dt} \tag{1}$$

"Q" is the heat flux, and the dE/dt expression is the change in energy over time (both expressed in units of J/s or W). The transfer of energy causes changes in temperature, depending on the properties of the material absorbing the energy (Incropera, et al. 2007). Temperatures can increase or decrease at a given location, depending on the environment and means of heat transfer.

There are three primary means of heat transfer: conduction, convection, and radiation. Conduction is the transfer of energy within and between two solid objects

in physical contact. The two objects must have different temperatures for heat transfer to occur. When evaluating conduction, the following equation is used to describe the heat flux (Incropera, et al. 2007).

$$Q = -k\nabla T A_s \tag{2}$$

In the equation, "Q" is the amount of energy transferred per unit time (in J/sec, or W). The "k" term is the conductivity of the material, and is in units of W/(m*K). The "∇T" term is the temperature gradient across the two conducting materials (K/m). Lastly, the A_s term is used to describe the surface area (m^2) of the two materials in contact with one another.

Convection is the transfer of energy through a fluid. Moving fluid can be used to transfer heat between the fluid and another object as it flows past. The following equation describes the heat transfer to an object through convection (Incropera, et al. 2007).

$$Q = -hA_s\Delta T \tag{3}$$

In the convection equation, "Q" is the heat flux (W). The "h" term is the convective heat transfer coefficient, and describes the amount of energy required to change the temperature of the fluid (W/m^2*K). The "A_s" term is the surface area of the object in contact with the fluid (m^2). The "ΔT" term is the difference in temperature between the object and the convective flow (^oK).

Radiation is the transfer of heat through electromagnetic waves traveling through space, emanating from a hot body exposed to a colder environmental sink. The following equation describes radiation from an object (Incropera, et al. 2007).

$$Q = \varepsilon \sigma A_{rad} T^4 \quad (4)$$

In the radiation equation, "Q" is the heat flux (W). The "ε" term is the emissivity of the object radiating energy (unitless coefficient). The "σ" term is the Stefan-Boltzmann constant (W/m^2*K^4). The A_{rad} term is the surface area of the radiating body (m^2). The "T" term is the temperature of the radiating body (K). The radiation is actually a function of the difference between the radiating body and its surroundings. The radiator is assumed to be perfectly pointed towards deep space (0^oK), with no obstruction or heat reflected back to the spacecraft which is why only one temperature term is used.

Low Earth Orbit Heat Loads

The heat loads into the spacecraft are driven by two sources: external heat loads from orbital environments, and internal heat loads driven by crew and avionics (Wertz and Larson, 1999). External heat loads vary based on the position of the spacecraft relative to the heat load sources. Internal heat loads can vary depending on workload and mission operations, but are near constant for most missions (Hanford, 2006). Heat dissipation is also a function of the space environment, primarily occurring through radiative transfer to deep space by the spacecraft radiators, with 'heat leak' from the spacecraft body neglected.

Heat is transferred to a spacecraft in LEO through four primary sources. First, solar radiation heats up the spacecraft in the dayside portions of the orbit. During the dayside portion of the orbit, some Sunlight reflects off of the Earth's atmosphere, creating an albedo heat load to the spacecraft. The Earth itself

provides a heat load through blackbody radiation. Lastly, the crew and avionics onboard create an internal heat load from the inside of the spacecraft (Williams and Palo, 2006). The total heat into the spacecraft cabin environment is characterized by the following equation.

$$\sum Q_{in} = Q_{sun} + Q_{albedo} + Q_{IR} + Q_{internal} \tag{5}$$

The heat load due to radiation is described in the following equation (Williams and Palo, 2006).

$$Q_{sun} = \alpha A_{\perp} I_{sun} \tag{6}$$

The "α" term is used to describe the absorbtivity of the spacecraft (unitless coefficient). The "$A_{\perp}$" term is the area of the object perpendicular to the Sun (m^2). The "I_{Sun}" term is the solar intensity of the Sun (W/m^2).

The albedo heat load is from the same source as the solar heat load, but only a portion of the Sunlight is reflected off the Earth (Williams and Palo, 2006).

$$Q_{albedo} = \alpha a A_{\perp} Fs I_{sun} \tag{7}$$

The albedo heat load equation utilizes the same "α" term and "$A_{\perp}$" term are the same as in Equation 6. There is an "a" term to describe the amount of reflectivity of the Earth's atmosphere (unitless). The "Fs" term is the view factor of the spacecraft in relation to the Sun's reflection off the Earth's surface (unitless).

The Earth infrared heat load is due to blackbody radiation from the Earth (Williams and Palo, 2006).

$$Q_{IR} = \alpha A_{\perp} I_{earth} \tag{8}$$

The "α" term and the "$A_{\perp}$" term are the same as in Equation 6. The "I_{Earth}" term is a constant used to describe the infrared intensity of the Earth's blackbody radiation.

The internal heat load is defined based on the mission and spacecraft the spacecraft is created for. The heat load from crew and avionics can vary depending on workload and mission operations. However, the variation is not predictable without taking a specific design and operations into account, so it is assumed as an average constant for this analysis (Wertz and Larson, 1999).

$$Q_{Internal} = constant \tag{9}$$

Active Thermal Control System Components

The ATCS is responsible for collecting, transporting, and rejecting heat from the spacecraft. As the heat loads enter the spacecraft, the thermal energy is collected and transported to various locations. For purposes of simplification, all incoming heat loads will be considered transported as one sum source into a "black box heat collector". The incoming heat loads are absorbed by the heat exchangers, to be moved towards the heat sinks. The heat sinks reject the heat loads from the spacecraft. The components and technology involved with the absorption, transfer, and rejection of heat are evaluated below.

Heat Absorption Components

When thermal radiation from LEO strikes a spacecraft, the incident energy can be absorbed, reflected, or transmitted through the spacecraft. In most cases, the spacecraft is opaque and no heat is transmitted through (Hanford, 2006).

$$\alpha+\varsigma=1 \quad (10)$$

In Equation 10 the absorbtivity (α, unitless) and the reflectivity (ς, unitless) add up to 1, since both are fractions of the total radiation to the spacecraft. The reflected heat load is not absorbed by the spacecraft (Hanford, 2006). The absorptivity coefficient is the only term considered in the calculation of the heat load to the spacecraft (see Equations 6-8). The absorptivity of multiple spacecraft coatings is listed below (Hanford, 2006).

Table 2: Absorbtivity and Emissivity of Typical Spacecraft Coatings

Material	**α**	***ε***
Silverized Teflon	0.07	0.80
Aluminized Teflon	0.12	0.80
Ortho Fabric	0.18	0.84
Beta Cloth	0.26	0.90
A276 White Paint	0.28	0.87
Clear Anodized Aluminum	0.38	0.83
Gold Anodized Aluminum	0.55	0.81
Black Anodized Aluminum	0.81	0.88
Alodine Aluminum	0.45	0.35
Bare Stainless Steel	0.42	0.11
Sand-Blasted Stainless Steel	0.58	0.38
Bare Titanium	0.52	0.12
Tiodized Titanium	0.82	0.51

White paint is typically used onboard spacecraft, due to its low absorbtivity, and high emissivity (NASA, 1995). For the purposes of the thesis analysis, it will be assumed that spacecraft will be coated with A276 white paint.

Heat Transfer Components

Liquid based heat exchangers provide a means of transporting a heat load from a hot location to a cool location through conduction and convection. It is assumed that counter flowing heat exchangers are the sole heat exchangers used in the ATCS architecture. Counter flowing heat exchangers are composed of two highly conductive heat pipes in contact with one another with fluids flowing through in opposite directions. The hot fluid transfers the heat energy to the pipe structure through convection. The hot pipe transfers heat to the cold pipe through conduction, and the heat is then absorbed by the cold fluid through convection (Kakac, et al. 2012). Figure 1 shows a basic schematic of a counter-flowing heat exchanger.

Figure 1: Counter Flowing Heat Exchanger (Hot Pipe on Top Cold Pipe on Bottom)

In Figure 1, the red lines represent the heat pipe containing the hot working fluid, and the blue lines represent the heat pipe containing the cool working fluid. The opposite facing arrows indicate the direction of the flow. A counter flowing heat exchanger has the liquids flow in opposite directions in order to maximize the

amount of heat transferred between the two liquids (Kakac, et al. 2012). The heat (Q_{HX}) is transferred from the hot side to the cold side as the two fluids flow past each other. The fluid temperature coming into the hot side ($T_{in(hot)}$) loses heat until it reaches its coldest temperature on the opposite side ($T_{out(hot)}$). The fluid temperature entering the cold pipes ($T_{in(cold)}$) increases to its maximum temperature ($T_{out(cold)}$) as it absorbs the heat from the hot pipes. The overall temperature trend over the length of the heat exchanger is shown below in Figure 2.

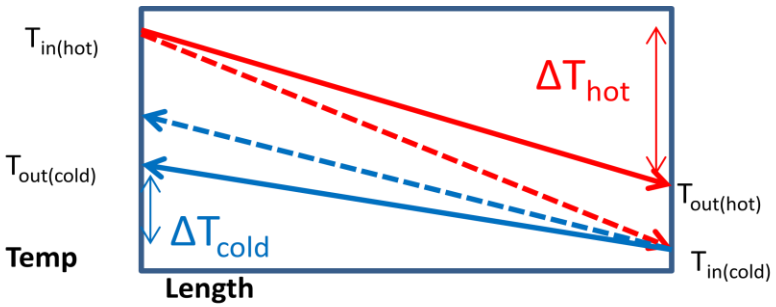

Figure 2: Actual and Ideal Temperature Trends for a Counter Flowing Heat Exchanger

The solid lines show the actual temperature changes over the length of the heat exchanger. The dotted lines show the ideal temperature change from the heat exchanger. Inefficiencies and length constraints cause the difference between the ideal and the realistic temperature trends (Kakac, et al. 2012).

Heat Rejection Components

To maintain thermal equilibrium, the heat coming into the spacecraft must be rejected from the spacecraft at the same rate. The method of heat rejection can be either passive or active. Passive heat rejection dissipates heat without the use of any moving parts in the thermal control system (Sozbir, et al. 2008). Passive heat

rejection for spacecraft is due to thermal emissivity from the surface of the spacecraft and is assumed to be negligible compared to the primary heat sink technology (Akin, 2009).

Active heat rejection technology utilizes the heat exchangers onboard the spacecraft to transfer the incoming heat loads to the heat sink (Mills-Alford, 2008). A heat sink is a technology used to reject heat loads. To maintain thermal equilibrium, the heat sinks must reject a heat load equal to the amount of heat coming into the spacecraft. The method of heat rejection is dependent on the heat sink technology, of which there are four primary categories: sublimators/evaporators, ablatives, radiators, and PCM.

Sublimators and evaporators are consumable driven heat sinks that reject heat through gaseous phase changes of the consumable (Alvidres and Hoetger, 1995). Sublimators transfer the heat load to a solid consumable, utilizing the energy to transform the material into its gaseous form. The gaseous form of the material is rejected into space, and is not recovered. The evaporator is utilized in the same fashion, with a liquid to gas phase change instead. This technology is advantageous because it is not environmentally driven, allowing the technology to be attitude independent. Also, the technology utilization requires no moving parts to transfer the heat load to the consumable (Stephan, 2011). However, the technology requires consumables for heat rejection. This is a limiting factor for most missions, unless there is an excess of the consumable onboard. In the case of the STS, the shuttle produced excess water onboard via fuel cells, providing the consumables for the

evaporator. However, spacecraft with limited consumable mass would likely not choose this technology.

Ablative heat sinks are passive systems that are used to absorb extreme heat loads, primarily during reentry (Stephan, 2011). The extreme heat load on the outside of the spacecraft is dissipated through the ablative material, so that the inside of the spacecraft can stay within mission requirements. The ablative technology is a passive system that absorbs heat, and rejects the heat by "flaking" off the spacecraft structure. However, this form of heat rejection cannot be used while on orbit, since the thermal heat loads are too low for the ablative material to flake off. Therefore, ablative materials are not considered for on orbit thermal control.

The most common form of heat sink for an LEO spacecraft is through radiator technology. A radiator rejects heat via thermodynamic radiation to an environment of colder temperature. This is useful in LEO, since the radiator can be pointed to deep space (assumed to be 0 ^{o}K) in both dayside and eclipse to maximize the amount of heat rejection (Wertz and Larson, 1999). Radiators are typically used due to their infinite sink capacity throughout the mission, since no consumable mass is required. However, radiators require specific attitude control to point to deep space, and the degradation of the material on orbit reduces the efficiency of the technology through the course of the mission (Wertz and Larson, 1999). Radiators also have a high mass and area requirement, making them a heavy and bulky technology to implement on a spacecraft (Wertz and Larson, 1999).

The last category of heat sinks is with PCM technology. A PCM can transform between its solid and liquid form to absorb heat loads from the spacecraft during the hot portions of orbit. Unlike sublimators and evaporators, a PCM remains onboard after it is melted, so it can be frozen to its solid phase again during the cold portions of orbit. Therefore, the PCM has a benefit in that it is a regenerable consumable (Quinn et al, 2011).

A PCM is typically used in conjunction with another heat sink technology onboard the spacecraft, usually a radiator (Lillibridge, 2011). PCMs have historically been used to regulate the heat rejection, or to buffer the heat loads, rather than reject the entire heat load. Both uses are beneficial, since the PCM utilization can decrease the mass and complexity of other systems. However, a PCM is limited in its buffer capacity, since it can only be used to absorb excess heat loads until the entire solid PCM is melted (Quinn, et al. 2011).

The PCM can be integrated into the ATCS in multiple ways. In the past, wax PCM were used on the outside of heat exchanger loops to absorb excess heat loads (Lillibridge and Navarro, 2011). An alternative means to implement the PCM is to directly place the PCM within the heat exchanger loops, by utilizing the working fluid as the PCM. This is the means by which TDA Research, Inc. has implemented the PCM within their heat exchanger.

Self-Regulating Heat Exchanger Characterization

TDA Research, Inc. has created the SRHX to utilize a water PCM within the hardware. Utilizing water as a working fluid is a fairly unique aspect of the

hardware. Water is safe to the crew, minimizing leak risk if the SRHX is used in the cabin. Water also has a high heat capacity (4.18 J/gK), making it an excellent working fluid to absorb heat from the cabin (Lide, 1990). Water makes a good PCM since it has a high heat of fusion, 334 kJ/kg (Nabity, 2008). In other words, water is an excellent coolant in its liquid phase.

However, water has some notable downsides. Water has a high freeze point compared to other fluids (0 ºC), meaning it freezes up easier in the cold environment of space (Lide, 1990). This is undesirable because the ice may block the flow path, preventing heat transfer. Also, water expands upon freezing, which may damage or destroy the heat exchanger tubes if the heat exchanger is not designed for this event.

The TDA Research Inc. SRHX is capable of using water as the working fluid since the hardware has been constructed to withstand the 9.3% volumetric expansion as the water freezes to ice (LaPlaca and Post, 1960).

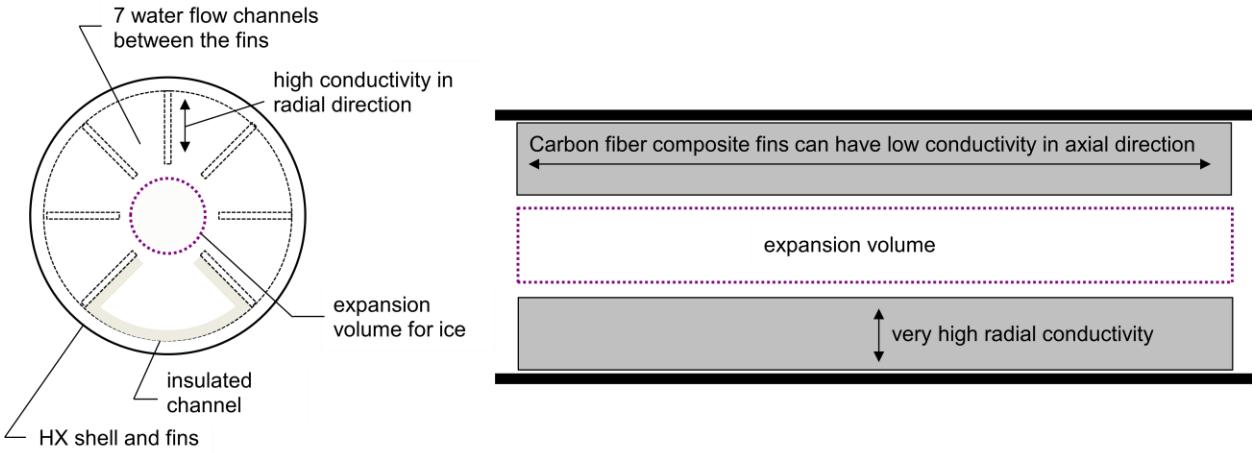

Figure 3: Cross-sectional Views of the SRHX

The configuration shown in Figure 3 is a layout for a 7-finned SRHX, though the number of fins can be varied. The configuration in Figure 3 is the test apparatus used for heat transfer analysis and testing. The fins extend from the tube surface toward the center of the SRHX.

The thermal conductivity of the fins and shell are material dependent. The tube used during testing is constructed of Al6061-T6 aluminum, with a thermal conductivity of 167 W/m-K (Aluminum Standards and Data, 2001). The fins transfer the heat to the SRHX shell, which conductively transports the heat to the radiator or ammonia loop. Two fin types were planned to be utilized during testing, aluminum (Al6061) and K-1100 carbon fiber. The fins are aligned so that there is high conductance in the radial direction to transport heat from the water to the shell. The Al6061 fins have an isotropic thermal conductivity of 167 W/m-K and the carbon fiber fins are assumed to have a conductivity of 540 W/m-K in the radial direction and 20 W/m-K in the axial direction (Metals Handbook, 1990). However, at the time of writing, only the aluminum finned SRHX was used for analysis and testing.

The fins absorb the heat from the water as it flows by. If the water temperature drops to below 0 ºC, the water changes its phase to ice. Since the fins are colder near the shell of the SRHX, the ice freezes up from the SRHX tube towards the middle of the SRHX (Nabity, 2008). To prevent the cross-sectional area from being fully blocked in cold conditions, the SRHX has a thermally insulated flow channel that remains open in nearly all operating scenarios (Nabity, 2008).

The water flow through this channel will thaw the other ice-filled channels as the heat load increases.

The ice freeze will reduce the flow area of the SRHX. The change in area of the SRHX will increase the pressure as the fluid flows through. This change in pressure (ΔP) can be used to regulate the amount of mass flowing through the SRHX if a bypass tube is attached. The bypass tube allows for a variable mass flow rate by diverting a portion of the working fluid through a separate pipe. The separate pipe will absorb no heat loads from the working fluid, allowing the working fluid to retain its heat load in cold portions of the orbit. In this fashion, the heat transfer is regulated by preventing a portion of the working fluid from rejecting its heat through the SRHX.

An alternative configuration is to use the SRHX without a bypass tube. Without the bypass tube, the ΔP will still be present through the SRHX, but it will not be used to regulate the mass flow rate. The hardware will simply be constructed to withstand the ΔP forces. With no change in mass flow rate, the SRHX must regulate its heat rejection in another fashion.

The SRHX can regulate its heat load by changing the amount of conductive surface area exposed within the SRHX. If the fins absorb more heat from the water than heat coming into the cabin, the water will freeze within the SRHX. The ice freeze within the SRHX will cover up the fins, reducing the area of the fins exposed to the fluid flow. The reduction of fin area in contact with the fluid reduces the amount of heat transfer out of the working fluid, since water primarily transfers

heat through highly conductive fins as opposed to a negligible amount of conduction through the ice (Nabity, 2008). In the opposite scenario, where the SRHX fin area is too little to reject all the heat from the working fluid, the excess heat load melts the ice. The ice melt will increase fin exposure, allowing more heat to be transferred through conduction.

The ice freeze and melt is used to regulate the efficiency of the SRHX, so that during cold portions of an orbit the SRHX will be limited in its heat rejection from the working fluid, and during hot portions of an orbit, the SRHX will be capable of rejecting all heat.

Another advantage of the SRHX is that the technology can reduce the mass of the ATCS system by augmenting or replacing other portions that might be utilized in an equivalent system. For instance, the SRHX might replace the water loop in a typical ATCS. The possible alternative architectures are evaluated in Chapter III.

Lastly, the water PCM can be used to absorb excess heat loads. As ice is melted from the fins, a portion of the heat load is absorbed from the working fluid through the phase change fusion process. The portion of heat spent in fusion no longer needs to be rejected by the radiator. Therefore, the radiator size can be reduced if the heat rejection to melt ice is used in parallel heat rejection. Likewise, if the radiator is oversized for a given heat load, the excess heat rejection can be used to re-freeze the PCM within the SRHX.

The additional mass, complexity, and safety from SRHX implementation must be considered in evaluating the effectiveness of the technology. The

effectiveness was determined through a preliminary ESM analysis. An ESM analysis is a means of comparing two similar systems by only changing out a single component between the two. The preliminary ESM is evaluated in Chapter IV.

CHAPTER III

PARAMETRIC SYSTEM ANALYSIS

A parametric system analysis is a means by which one takes a complex model and breaks it into individual components to be analyzed. There are three main components analyzed in integrating the SRHX with an ATCS. The first component of analysis was to accomplish Aim 1: determining the range of LEO heat loads a spacecraft absorbs through its orbit. Next, Aim 2 is accomplished by evaluating the possible means of transferring the heat loads through the spacecraft ATCS architecture. Lastly, Aim 3 is accomplished by theoretically predicting the SRHX hardware response to heat loads in a steady state and dynamic environment.

LEO Heat Load Modeling

The first aim (Aim 1) of the thesis was to determine the heat flux into a typical LEO spacecraft. The four heat load sources in LEO—Sun, albedo, Earth, and internal—are summed into a singular heat input into the spacecraft.

$$Q_{in} = Q_{sun} + Q_{albedo} + Q_{IR} + Q_{internal} \tag{11}$$

The Sun (Q_{Sun}) and albedo (Q_{albedo}) heat loads are dependent on the spacecraft's position on orbit (Akin, 2009). The internal heat load ($Q_{internal}$) and infrared radiation from the Earth (Q_{IR}) are considered constant on all points on orbit (Akin, 2009). The summation of all heat loads affecting the spacecraft is the overall heat load into the spacecraft (Q_{in}). The spacecraft orbit is defined and propagated in order to model the individual components of heat flux at each

position. The spacecraft properties are specified, and determine how much of the heat flux is absorbed into the spacecraft.

Orbit Modeling

The spacecraft orbit is assumed to be in LEO with an eclipse. The analysis assumes a height of 350 kilometers since this was the typical height profile of the STS mission (NASA, 2005). The spacecraft is assumed to be in a polar (inclination=90 º) and circular orbit (eccentricity=0) around the Earth. These assumptions were introduced to allow for an iterative analysis of the beta angle, though this analysis ultimately only looked at a beta angle of 0º. The beta angle is defined as the angle between the spacecraft's orbital plane and the Sun-Earth vector. A beta angle of 0 º indicates the spacecraft is located directly between the Sun and the Earth at orbit noon, and directly behind the Earth at orbit midnight. A beta angle of 90º represents a spacecraft orbital plane perpendicular to the Sun-Earth vector.

To calculate the orbit of the spacecraft, the initial position and velocity of the spacecraft are specified. The orbital model assumes a modified Earth Centered Earth Fixed (ECEF) frame, with the Sun being directly located along the X-axis. The modified ECEF frame, along with an example spacecraft, is shown in Figure 4.

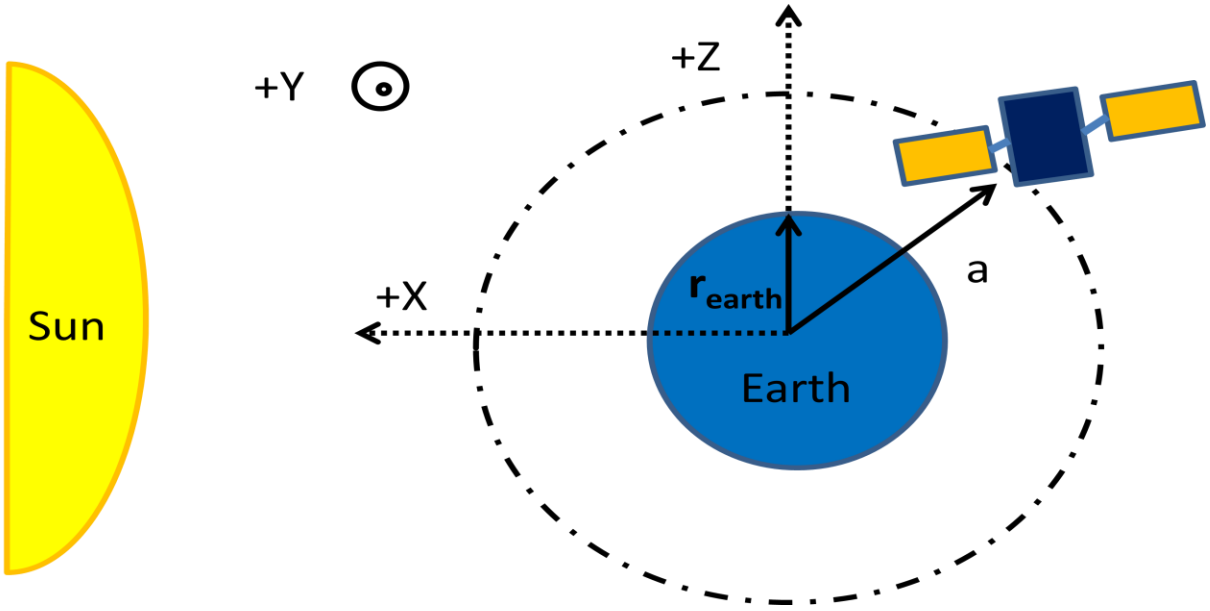

Figure 4: Modified ECEF Frame and an Orbiting Spacecraft

The spacecraft's initial position is assumed to be at orbit noon, where the Z component of the ECEF is 0. In the modified ECEF frame, orbit noon is described in vector form in Equations 12-14 (Curtis, 2009).

$$pos\,(0)=[\cos(ß)*(a),\ \sin(ß)*(a),\ 0] \tag{12}$$

$$a= R_{Earth}+height_{s/c} \tag{13}$$

$$R_{Earth}=6378.1\ km \tag{14}$$

In Equation 12 pos(0) is the initial position of the spacecraft (km), and ß is the beta angle of the spacecraft (degrees). The "a" term is the semi-major axis of the spacecraft (km), R_{Earth} is the average radius of the Earth (km) and $height_{s/c}$ is the height of the spacecraft (km).

Since the spacecraft is in a polar circular orbit, the spacecraft is going directly North, or directly South at orbit noon. The direction is inconsequential to heat loads, so the analysis assumes that the spacecraft is traveling Northward at

orbit noon. The magnitude and vector of the initial velocity can be represented with the following equations (Curtis, 2009).

$$\text{vel}(0)=[0,0,v] \tag{15}$$

$$v = sqrt(\frac{\mu_{earth}}{a}) \tag{16}$$

In the equations, vel(0) is the vector form of the initial spacecraft velocity (km/sec). The "v" term is the magnitude of the velocity of a circular orbit (km/sec), "a" is the semi-major axis of the spacecraft (km), and μ_{Earth} is the standard gravitational parameter of Earth (km^3/s^2).

A two-body orbit is assumed for the spacecraft orbiting around Earth. The equations associated with a two-body orbit allow propagation of the spacecraft through its orbit. By using the propagation, the location of the spacecraft can be determined for each point on orbit (Curtis, 2009).

The computer program MATLAB is used to iterate the position of the spacecraft each second after the initial point. The MATLAB program uses a function called "ode45" to iterate through the orbit, given a set of equations used to find the change in position for each time step. For each second in the orbit, the following equations are used to give a new position and velocity of the spacecraft (Curtis, 2009).

$$pos(i+1) = [posx\ i\ + velx(i),\ posy\ i\ + vely(i),\ posz\ i\ + velz(i)] \tag{17}$$

$$vel(i+1) = [velx\ i\ +\ -\mu * \frac{posx\ i}{a^3}\ , vely\ i\ + (-\mu * \frac{posy\ i}{a^3}), velz(i) + (-\mu * \frac{posz\ i}{a^3})] \tag{18}$$

The terms within Equations 17 and 18 are the same as Equations 12-16. The iteration begins at i=0, and ends at i=30,000. The code simulates the orbit for

30,000 seconds, which allows for 5-6 orbits worth of position and velocity data to be collected and saved. The position data can then be correlated to incoming heat loads at each second.

Heat Load Boundary Conditions

Once the orbit is specified, the thermal loads can be specified for each position. The internal and Earth infrared heat loads are considered constant for each position throughout the orbit. The Sun and albedo heat loads need to be represented with equations that describe the heat load with respect to spacecraft position.

The Sun is assumed to be radiating at a constant intensity, providing a constant heat load whenever the spacecraft is exposed to the Sun. The heat load from the Sun is considered to be zero if the spacecraft is shaded by the Earth in eclipse. The code does not account for umbra or penumbra partial eclipse; full eclipse is assumed whenever the Earth is between the spacecraft and the Sun. The code determines whether the spacecraft is in eclipse by using the basic logic in Equations 19-20.

If -6378.1 km > posx(t) > 6378.1 km

And

If -6378.1 km > posz(t) > 6378.1 km

Then

$$Q_{sun} = \alpha_B A_{\perp} I_{sun} \tag{19}$$

Else

$$Q_{sun} = 0 \tag{20}$$

In Equation 19, α_B is the absorbtivity of the spacecraft coating (unitless). This term dictates how much of the thermal environment is absorbed into the spacecraft body. The $A_{\perp}$ term is the cross sectional area of the spacecraft relative to the Sun (m^2). The I_{Sun} term is the heat flux of the Sun. The logic determines if the spacecraft is in the shadow of the Earth by checking if the position of the spacecraft is within the coordinates of the shadow's volume cast by the Earth. The shadow is assumed to be cylindrical, stretching out from the edges of the Earth, away from the Sun, as seen in Figure 5.

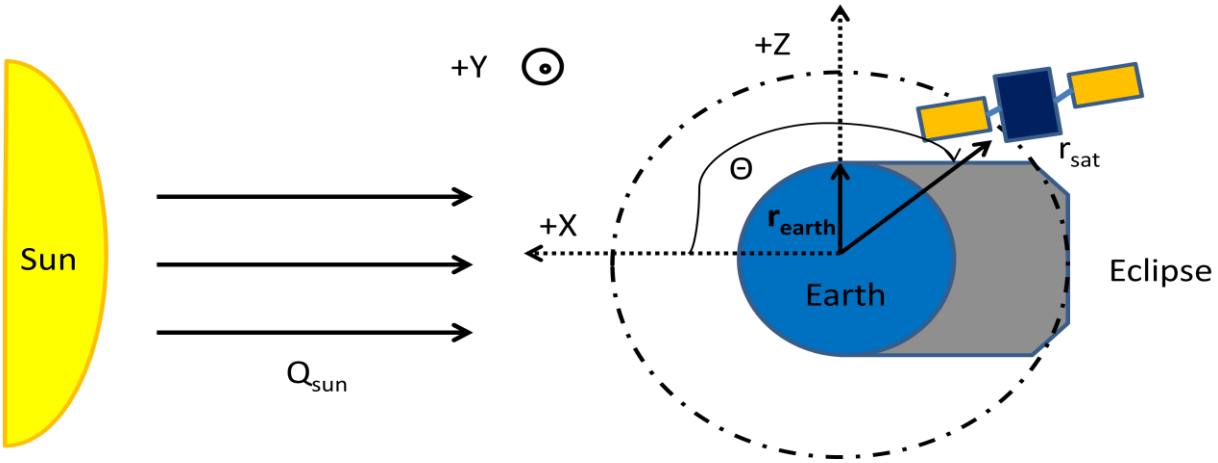

Figure 5: Spacecraft Orbit and Eclipse

Figure 5 shows the position of the spacecraft relative to the modified ECEF frame. The position of the spacecraft is represented trigonometrically by setting "Θ" to be the angle of the spacecraft relative to the +X axis. The grey portion stretching from the Earth on the opposite side of the Sun is the portion of orbit where the spacecraft will be in eclipse.

The albedo heat load is the solar flux reflecting off of the Earth's atmosphere. The reflectance is assumed to heat the spacecraft when the spacecraft is between the Sun and the Earth, since the Sunlight needs to reflect off of the Earth's surface before touching the spacecraft. The view-factor coefficient, F_s, is the term which describes the amount of the albedo heat load that strikes the spacecraft. The Sunlight reflects off of the Earth's atmosphere most strongly at orbit noon, since the view factor is highest when the albedo heat load vector is entirely along the Sun-Earth vector. The albedo heat load, and the corresponding view factor is described below in Equations 21-23.

$$Q_{albedo}(t)=\alpha a A_{\perp} I_{Sun} F_s(t) \tag{21}$$

$$Fs(t) = Fs*\cos(\Theta)*\cos(\beta) \qquad -90^o < \Theta < 90^o \tag{22}$$

$$Fs(t) = 0 \qquad 90^o < \Theta < -90^o \tag{23}$$

In Equation 21, the "a" term is the albedo reflectance factor (unitless), which describes the reflectivity of the atmosphere. The Fs(t) term is the view-factor coefficient of the spacecraft at its specified position (unitless). Θ is the position of the spacecraft relative to the +X axis (degrees). "ß" is the beta angle of the orbit (degrees). The Θ and ß terms are used to determine the view-factor coefficient at each point on orbit.

Heat Loads Absorbed by Spacecraft

The equations for each heat load source are combined into one summed heat load, as shown in Equations 24 and 25.

$$Q_{in} = Q_{sun} + Q_{albedo} + Q_{IR} + Q_{internal} \tag{24}$$

$$Q_{in} = \alpha_w A_\perp I_{sun} + \alpha_B a A_\perp F_s I_{sun} + \alpha_B A_\perp I_{IR} + Q_{internal} \quad (25)$$

The list of terms and relative values for the heat load are listed below in Table 3.

Table 3: Variables Used in Heat Load Calculation

Symbol	Variable Definition	Value Source	Value
α_B	Spacecraft Absorptivity	Known	0.22
μ	Standard Gravitational Parameter	Known	398,600 km^3/s^2
$A_\perp$	Perpendicular Area	Known	3.14 m^2
I_{Sun}	Solar Heat Flux	Known	1365 W/m^2
a	Earth Albedo Coefficient	Known	0.22
F_s	View Factor s/c to Earth	Known	1
I_{IR}	Infrared Intensity of Earth	Known	275 W/m^2
$Q_{internal}$	Internal Heat Load	Define	1000 W

The values listed in Table 3 are determined assuming an average thermal output from the Sun, Earth, and albedo (Williams and Palo, 2006). The values associated with the spacecraft itself are determined by assuming the spacecraft is a one meter radius, spherical spacecraft. This is similar to the shape and size of the Crew Exploration Vehicle (CEV) (NASA, 2005). White paint is assumed to cover the entire surface of the spacecraft as is typical of spacecraft in LEO (Hanford, 2006). By utilizing the propagated orbit, along with the specified equations and values, the absorbed heat loads into the spacecraft can be determined.

Results

The analysis iterates through various orbits and beta angles. To give an overall impression of the heat load modeling, a heat load for a 350 km, 0 beta angle

orbit, with a 1m radius, white coated spacecraft is chosen as a representative case. The heat loads absorbed into the spacecraft over the course of 6 orbits is shown below in Figure 6. (The code used to calculate and plot Figure 6, and any following MATLAB figures can be found in APPENDIX A).

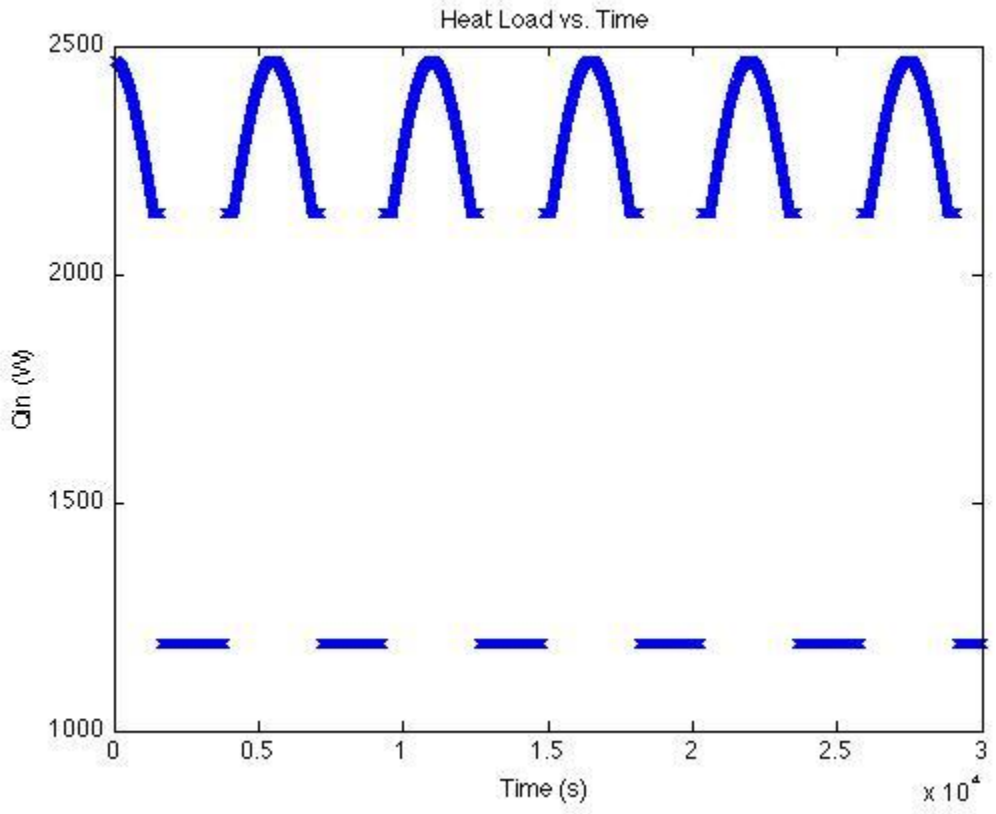

Figure 6: Heat Load over 6 orbits for a 1m Radius Spherical Spacecraft

The heat load shows three noticeable trends. Initially, the heat load is at its maximum, 2463.7 Watts, since the spacecraft starts at orbit noon where all four heat load sources are at their maximum. The heat load decreases from orbit noon, since the albedo heat load decreases as the spacecraft moves away from directly between the Earth and the Sun. There is a flat portion after the curved portion of the trend. The flat portion is the heat load without albedo, 2133.5 Watts, when the spacecraft moves behind the Earth but is still exposed to the Sun. The trend then

drops to an 1190.1 Watts heat load input. This is the heat load of the spacecraft in eclipse, when the Sun's heat load is blocked by the Earth. After the spacecraft exits eclipse heat load increases back to the non-albedo, dayside heat load. The heat load begins to trend upwards when the spacecraft moves between the Earth and Sun, and the albedo heat load strikes the spacecraft. The heat load continues to increase until orbit noon, where the trend repeats orbit to orbit.

Validation of Heat Load Trends

The trends shown above in Figure 6 are validated by looking at previous analysis done in past research. The image below is the spatial distribution of the Earth orbital temperature (Stephan, 2011).

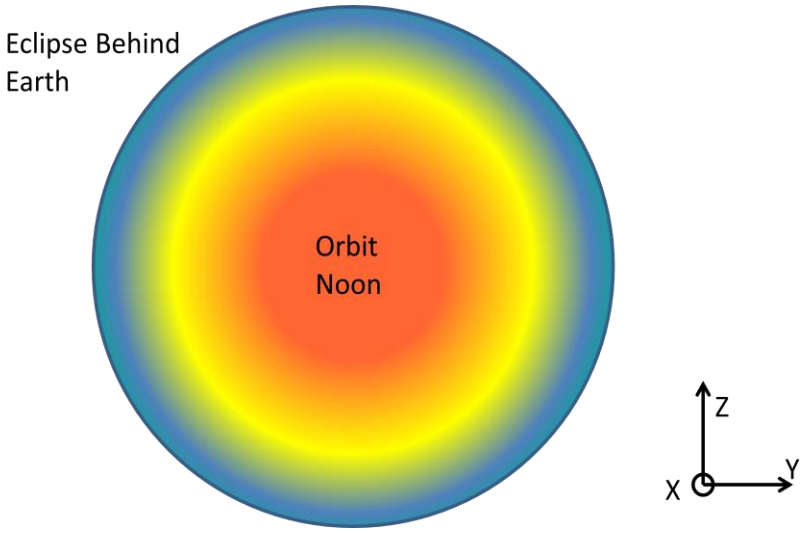

Figure 7: Heat Load Distribution in LEO

Figure 7 shows Earth as viewed from the Sun. The red portion at orbit noon indicates the highest heat load. The blue portion indicates lower heat loads, with the minimum behind the earth in eclipse. The figure shows a gradual change in colors from orbit noon towards eclipse, indicating lower heat loads away from orbit

noon. The decrease in heat loads is due to the decrease in reflectivity from albedo heat loads away from orbit noon. Ultimately, the trend shown by Figure 7 affirms the trending shown in Figure 6.

Another validation source comes from the thermal analysis of a small spacecraft. During the study, the heat load was modeled for a similar, low beta angle orbit in LEO. The overall heat load absorbed by the spacecraft is represented below in Figure 8 (Khaniki, 1994).

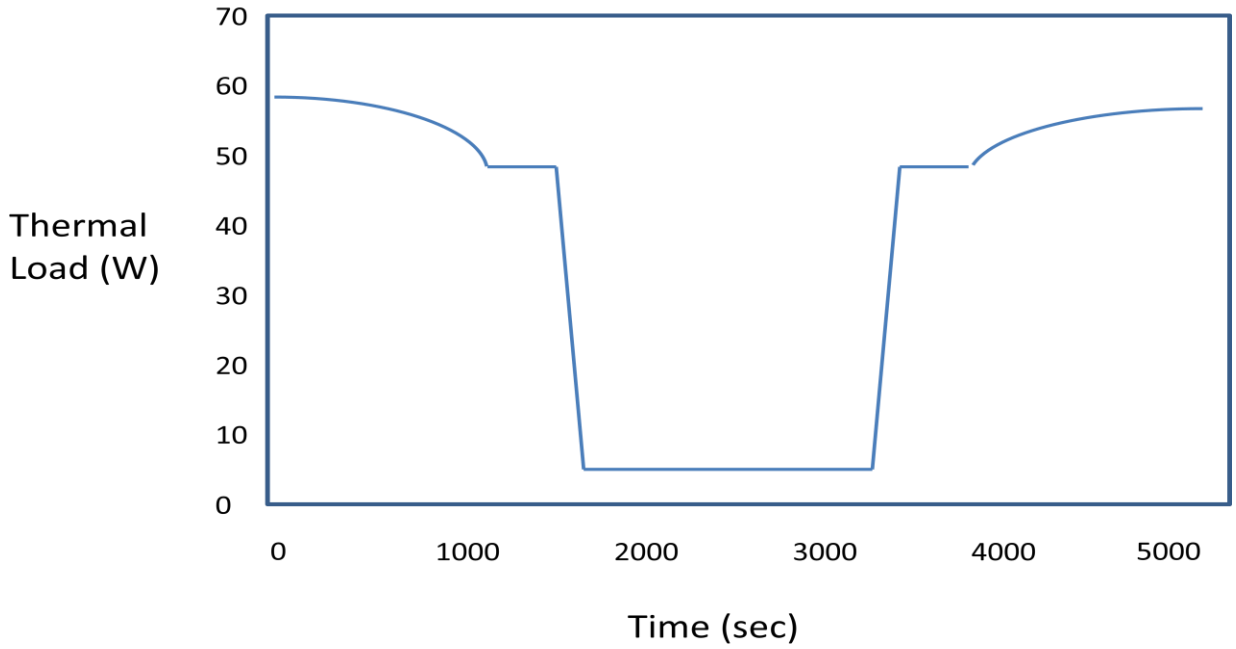

Figure 8: Thermal Load Versus Time for a Small Spacecraft

The model in Figure 8 is for a cubesat, which has a much lower surface area than the one meter spacecraft modeled in Figure 6. This accounts for the much smaller range in the thermal heat load along the y-axis. The overall trends between the two models match up fairly well, other than the heat load range. Khaniki's analysis shows the albedo heat load decreasing after orbit noon, and also shows the flat portion of heat load as the spacecraft travels behind the Earth, but is still

exposed to the Sun. The heat load drops rapidly in the middle portion of the figure, indicating that the spacecraft has entered eclipse. As the spacecraft exits eclipse, the increase in temperature from albedo heat loads matches the trend shown in Figure 6. The time scales for one orbit of both Figure 6 and 8 are similar as well. Therefore, the heat load model shown in Figure 6 is in line with previous studies.

Architecture Options

The second aim (Aim 2) of the thesis was to evaluate the possible means of implementing the SRHX into the spacecraft ATCS. The SRHX can be implemented within a typical ATCS architecture by replacing or augmenting portions of the baseline architecture. The baseline architecture is assumed to contain two (non-freezable) heat exchanger loops: an internal air-to-water heat exchanger, and a second, external water-to-ammonia heat exchanger. Air is circulated throughout the cabin to collect and transport the heat loads to the water loop, which is located within the spacecraft to prevent the water from freezing. The water loop transfers the heat to the externally located ammonia loop, which dissipates the absorbed heat to space via a radiator.

Multiple configurations were evaluated to implement the SRHX into the baseline architecture. Ultimately, three alternate architectures were determined to be feasible configurations to implement the SRHX. The first alternate architecture uses the SRHX to replace the entire water-to-ammonia loop, such that the SRHX is used to reject the heat load coming into the spacecraft directly to the radiator. A second architecture involves replacing the air-to-water loop with the SRHX. The third alternate architecture is a variation of the second, which is intended to

'augment' the water loop rather than replace it. The baseline architecture and the three alternative architectures for SRHX incorporation are described below.

Baseline Architecture

The baseline architecture assumes a two loop heat exchanger system in the ATCS, with water and ammonia as the working fluids. Two heat exchangers are used instead of one to transfer the heat, because each contains a separate working fluid, with unique properties. The properties of water and ammonia are listed in Table 4 (Lide, 1990).

Table 4: Thermal Properties of Water and Ammonia

Working Fluid	Specific Heat Capacity	Melting Point	Boiling Point	Toxicity
Water	4.18 J/g*K	0 °C	100 °C	None
Ammonia	4.71 J/g*K	-77.73 °C	-33.34 °C	Minor

The two working fluids need to stay within their liquid phase to flow through the heat exchangers. The water is used internally to absorb heat from the cabin, since the cabin operates at 15-25 ºC, which is too hot for ammonia (Hanford, 2006). Since the internal heat exchanger is located in the habitable environment, a non-toxic fluid is preferable in case of a leak. Ammonia is used to externally transport the heat from the water to the radiator, since the radiator typically operates in temperature ranges from -20ºC to -80ºC in LEO, which is too cold for water (Wertz and Larson, 1999). The specific heat capacity describes the amount of energy that needs to be absorbed by a unit mass to increase the temperature by one degree Celsius. Both water and ammonia have a relatively high heat capacity, making both

good working fluids to transport heat. It is assumed that the heat capacity of each working fluid will remain at a constant value for all environments.

For the baseline architecture, the incoming heat load to the cabin is entirely absorbed by the water (H20) loop. The water loop transfers all heat to the ammonia (NH3) loop, where the heat is dumped to the radiator and is rejected. A schematic of the baseline architecture is shown below in Figure 9.

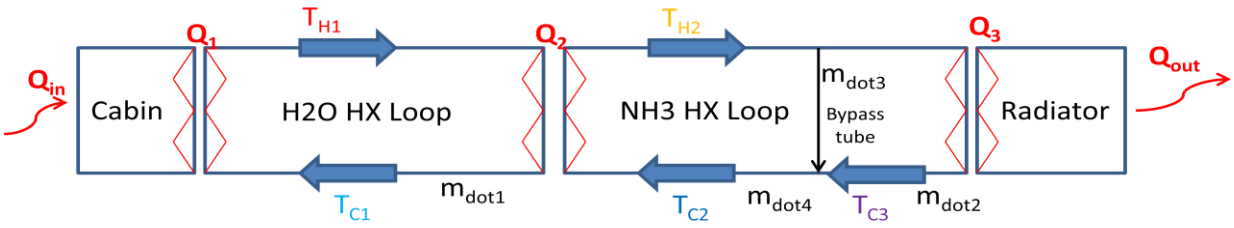

Figure 9: Baseline Architecture Schematic

In Figure 9, the heat enters the cabin, where the air-to-water heat exchanger allows the water to absorb the heat load. The water increases in temperature depending on the heat load in, and the mass flow rate, as described in Equations 26-27.

$$Q_{in}=Q_1 \tag{26}$$

$$Q_1 = (m_1 * c_{p_{H20}} * [T_{H1} - T_{C1}]) \tag{27}$$

The heat transferred from the cabin air to the water heat exchanger is described as Q_1, and is equal to the amount of heat absorbed to the spacecraft. The m_1 term is the mass flow rate of water (kg/sec). The c_{p_H20} term is the specific heat capacity of water, shown in Table 4. T_{C1} and T_{H1} are the respective temperatures of the water before and after the heat transfer (ºC). The heat is then transferred to the ammonia working fluid in a very similar fashion, as described in Equations 28-29.

$$Q_{in}=Q_1=Q_2 \tag{28}$$

$$Q_2 = (m_4 * c_{p_{NH3}} * [T_{H2} - T_{C2}]) \tag{29}$$

The heat transferred to the ammonia is described as Q_2, and is equal to the amount of heat absorbed to the water. The m_4 term is the mass flow rate of ammonia. The c_{p_NH3} term is the specific heat capacity of ammonia, shown in Table 4. T_{C2} and T_{H2} are the respective temperatures of the ammonia before and after the heat transfer. The heat is then rejected to the heat sink, which is assumed to be a radiator. The amount of heat rejected out through the radiator is described in Equations 30-31.

$$Q_{in}=Q_1=Q_2=Q_{out} \tag{30}$$

$$Q_{out} = (m_2 * c_{p_{NH3}} * [T_{H2} - T_{C3}]) \tag{31}$$

The heat rejected from the ammonia is described as Q_{out}, and is equal to the amount of heat absorbed to the ammonia loop. The heat rejection can be turned down if the ammonia travels through the bypass tube where no heat is rejected (m_3). The flow that does not go through the bypass tube goes through the radiator instead (m_2), where heat is rejected from the fluid. The c_{p_NH3} term is the specific heat capacity of ammonia. T_{C3} and T_{H2} are the respective temperatures of the ammonia before and after the heat rejection. This allows for the radiator to only output the amount of heat required to maintain thermal equilibrium.

The temperature trends for the baseline architecture depend on the heat loads coming into the spacecraft. The temperature trends for a typical orbit are shown in Figure 10.

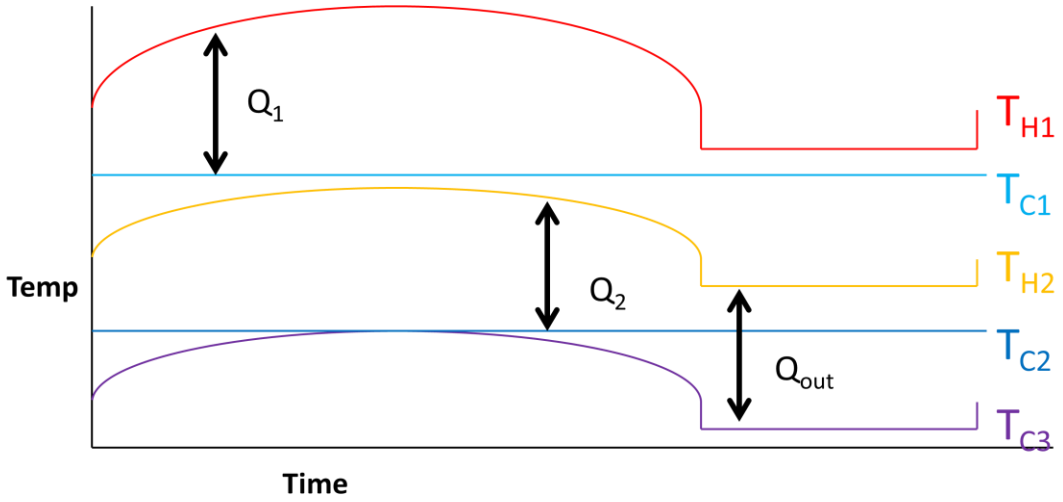

Figure 10: Temperature Profiles of the Baseline Architecture Through LEO

All terms in Figure 10 are the same as Equations 26-31. Q_1 is measured as the heat transfer due to the temperature difference between the T_{C1} and T_{H1}. Q_2 is measured as the heat transfer due to the temperature difference between the T_{C2} and T_{H2}. Q_{out} is measured as the heat transfer due to the temperature difference between the T_{C3} and T_{H1}. The T_{C3} temperature goes down below the T_{C2} temperature whenever the heat rejection from the radiator needs to be bypassed. Since the radiator is sized for the worst case heat load in the baseline architecture, the ammonia is bypassed for all other times except for orbit noon (the peak of the heat load). The temperature values are a function of the mass flow rates. Since the mass flow rate is a variable design parameter, no set value was chosen for the analysis, and only the general temperature trends are shown in Figure 10.

The trends in Figure 10 assume that the spacecraft is exiting eclipse at the beginning of the timeline. The heat load increases as the spacecraft nears orbit noon, shown by the peak of the temperature curves. As the heat load absorbed into

the spacecraft increases, Q_1, Q_2, and Q_{out} heat loads must increase as well. After orbit noon, the heat load decreases, as do the temperature changes from Q_1, Q_2, and Q_{out}. The drop at the end of Figure 10 is due to the spacecraft entering eclipse, where the heat load is at its minimum. The eclipse is where the maximum amount of heat has to be bypassed, which accounts for the minimum T_{C3} values.

SRHX Implementation

The baseline architecture can be modified within the SRHX in three potential alternative architectures. The first alternative architecture replaces both the water and ammonia loop with the SRHX. The second alternative architecture replaces the water loop with the SRHX, while keeping the baseline ammonia loop.

The third alternative architecture involves augmenting the water loop with the SRHX.

Alternative Architecture 1

Alternative architecture 1 is the ATCS with both the ammonia and water loops replaced by the SRHX and a bypass tube. If both the water and the ammonia loop are replaced by the SRHX, all incoming heat is absorbed by the water working fluid as it flows through the cabin. The water then rejects heat to the radiator, and to the phase change material within the SRHX. A schematic of the first alternate architecture is shown below in Figure 11.

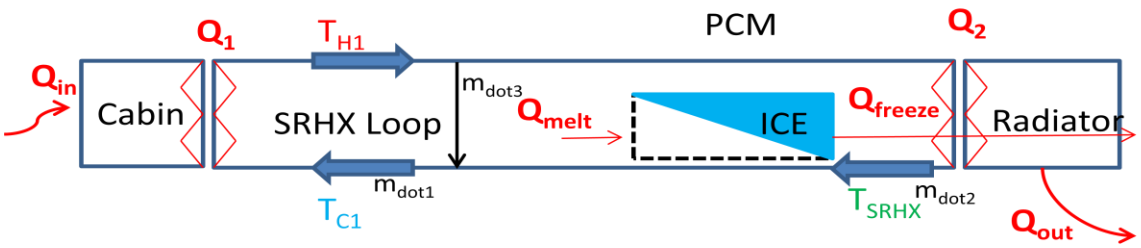

Figure 11: Alternative Architecture 1 Schematic

In this alternative architecture, the ice within the SRHX acts as the PCM for the heat rejection. A bypass tube is shown on the left hand side of the figure, and is included to regulate heat rejection through diverting mass flow. The bypass tube is not required if dynamic test results demonstrate the SRHX can provide sufficient heat rejection regulation without a bypass tube. Since this is not known at this point, the bypass tube is assumed to be included. The equation describing the heat transfer through the SRHX is shown in Equation 32.

$$Q_1 = Q_2 = Q_{Fins} + Q_{PCM} = (m_2 * c_{p_{H2o}} * [T_{H1} - T_{SRHX}]) \quad (32)$$

Q_1 and Q_2 are equal to achieve thermal equilibrium. Q_2 is the sum of the heat rejected by the PCM and through the SRHX fins. Q_{fins} is the amount of heat being transferred out through the heat exchanger structure. Q_{PCM} is the amount of heat transferred to the ice PCM. Q_{PCM} can be either positive or negative, depending whether the PCM is being melted, or frozen. If the PCM is absorbing the heat load, the Q_{PCM} value is positive and is labeled as Q_{melt}. If the fins are rejecting more heat than is coming into the spacecraft, the water freezes up. In this case, Q_{PCM} is negative and is labeled as Q_{freeze}. The T_{H1} and T_{SRHX} terms are the temperatures

going into and out of the SRHX. The temperature trends for the first alternative architecture are shown in Figure 12.

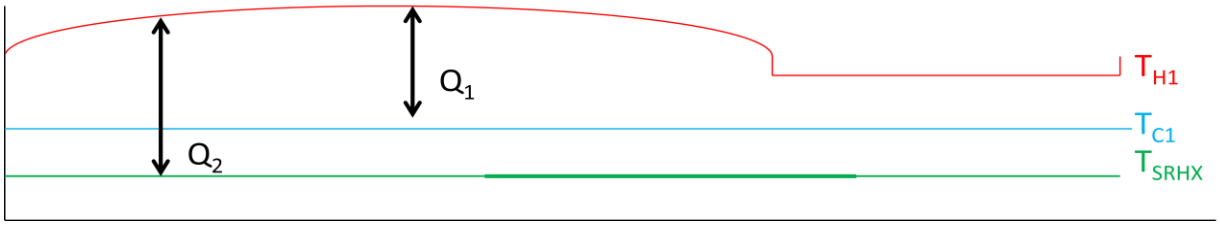

Figure 12: Alternative Architecture 1 Temperature Trends

All terms in Figure 12 are the same as Equation 32. As with Figure 10, the temperature range is a function of the unspecified mass flow rate. For this reason, only the general temperature trends are shown Figure 12. Q_1 is measured as the heat transfer due to the temperature difference between the T_{C1} and T_{H1}. Q_2 is measured as the heat transfer due to the temperature difference between the T_{SRHX} and T_{H1}. Q_2 is a summed term dictating the heat rejected by both the fins and the ice melt/freeze.

While the temperature changes due to Q_1 and Q_2 are different, the Q_1 and Q_2 values remain equal by having variable mass flow rates compared to one another. The mass flow rate through the Q_1 heat exchanger will remain constant, but the mass flow rate through the Q_2 section will be similar to that shown in Figure 13.

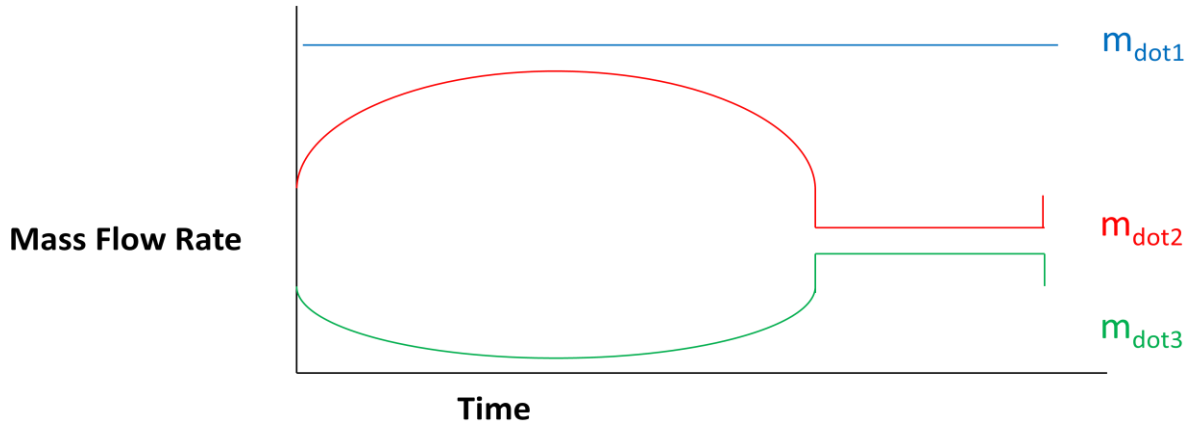

Figure 13: Mass Flow Rate in Alternative Architecture 1

In Figure 13, m_{dot1} is the mass flow rate through the air/water internal heat exchanger, m_{dot2} is the mass flow rate through the SRHX/radiator heat exchanger, and m_{dot3} is the mass flow rate bypassed from the SRHX. The bypassed mass flow does not change temperature until it encounters the colder, T_{SRHX} temperature fluid. The T_{SRHX} temperature is lower than the T_{C1} temperature since the cold water from the SRHX heat rejection meets up with the hotter, bypassed water to combine into the T_{C1} temperature.

Alternative Architecture 2

Replacing both the water and ammonia heat exchanger loops is one method of changing the architecture. The other two alternative options modify solely the baseline water loop, and keep the ammonia loop unchanged. The second alternative architecture option is to replace the entire water loop with the SRHX. This architecture is shown in Figure 14.

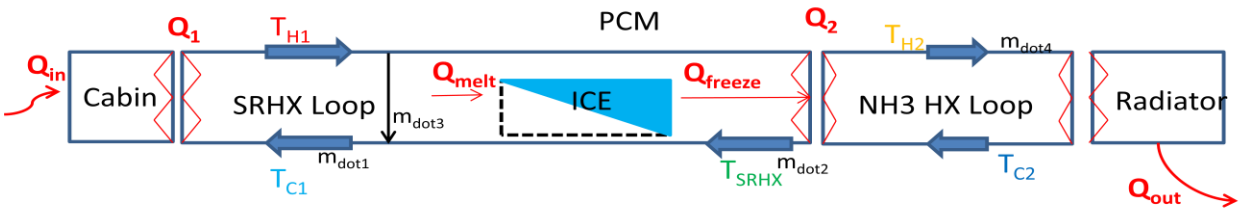

Figure 14: Alternative Architecture 2 Schematic

The architecture changes two main things from the baseline architecture. First, the water loop is now the SRHX loop, since the water is allowed to freeze at the Q_2 heat exchange point. The ice freeze allows for heat load buffering, since the ice can be used to absorb the heat load in the hot portions of orbit. The second change comes from moving the bypass valve from the ammonia loop to the SRHX loop. The bypass valve allows for heat rejection regulation through changing the mass flow rate through the SRHX, though it is possible that the bypass valve can be removed entirely if the SRHX fin size reduction through ice buildup is sufficient to regulate the heat load rejection itself. The temperature trends for alternative architecture 2 are shown in Figure 15.

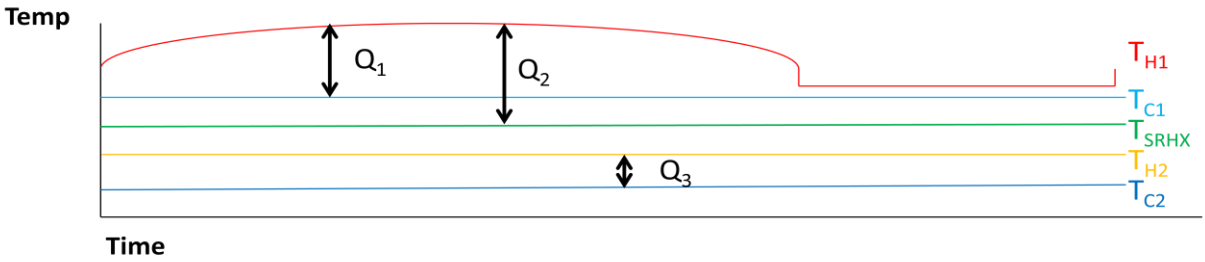

Figure 15: Temperature Trends for Alternative Architecture 2

All terms in Figure 15 are the same as Equations 26-31. As with Figures 10 and 12, the temperature range is a function of the unspecified mass flow rate. For this reason, only the general temperature trends are shown, and not set values. Q_1

is measured as the heat transfer due to the temperature difference between the T_{C1} and T_{H1}. Q_2 is measured as the heat transfer due to the temperature difference between the T_{SRHX} and T_{H1}. Q_2 is a summed term dictating the heat rejected by both the fins and the ice melt/freeze. Q1 and Q2 are both large during orbit day (beginning portion of Figure 15), and decrease significantly during eclipse (latter portion of Figure 15).

The T_{SRHX} temperature is lower than the T_{C1} temperature since a portion of heat rejection from to the SRHX is bypassed. The amount of water bypassed follows the same trend shown in alternative architecture 1. This bypassed mass flow meets back up with the fluid exiting the SRHX to return to the constant T_{C1} value. The T_{H2} and T_{C2} temperatures stay at constant values, since a constant amount of heat is rejected by the radiator into deep space. In the hot portion of the orbit (first portion of the graph) Q_3 is less than Q_1, meaning that ice melt has to buffer the heat load. In the cold portion of the orbit (the latter part of Figure 15) Q_3 is greater than Q_1, meaning that the excess heat rejection goes into freezing up the ice.

Alternative Architecture 3

The last alternative architecture is to augment the water loop by placing the SRHX on the side of the water loop. For alternative architecture 3, a bypass valve is placed on the outside of the H2O loop that leads towards the separate SRHX hardware. This bypass valve is required to allow the water to flow into the SRHX if heat buffering is needed. In the H20 HX loop, the water will remain in its liquid phase, since the H2O heat exchanger tubes are not built to withstand ice freeze.

Since the working fluid in both the H2O HX and the SRHX are the same, the water can be diverted directly to the SRHX when heat buffering is required.

The SRHX can either be put on the hot side (after Q_1) or on the cold side (after Q_2) of the H2O heat exchanger loop. Both locations for the SRHX augmentation will be analyzed. The first location for the SRHX augment to the baseline water loop is shown below in Figure 16.

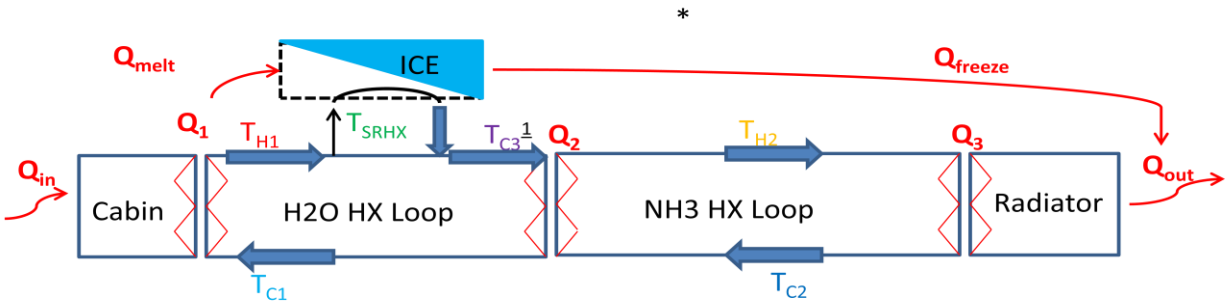

Figure 16: Alternative Architecture 3 Schematic

The ammonia loop is unaffected by the SRHX implementation into the water loop, since the PCM is independent of the ammonia heat exchanger. T_{SRHX} is the temperature of the water coming out of the SRHX, and T_{C3} is the combined temperature coming from T_{SRHX}, and the T_{H1} temperature, before the heat is transferred to the ammonia. The temperature trends for the third alternative architectures are shown in Figure 17.

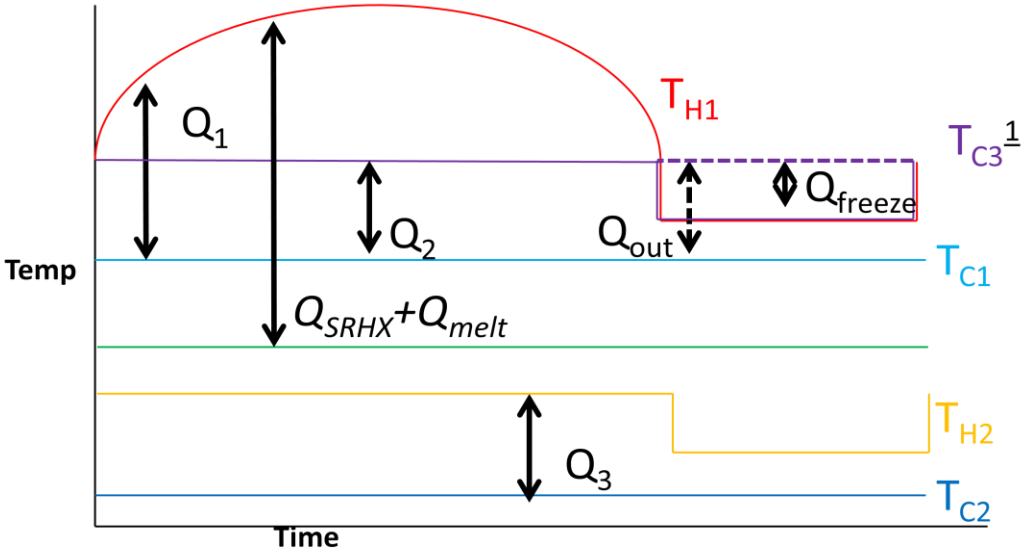

Figure 17: Alternative Architecture 3 Temperature Trends

The temperature trends are similar to that seen in Figures 10 and 15. In this architecture, the water is bypassed to the SRHX in the hot portion of the orbit, creating the temperature change from T_{H1} to T_{SRHX}. This cooled water combines with the T_{H1} temperature to bring the water temperature down to T_{C3} before the water/ammonia heat exchange takes place. The water/ammonia heat exchange cause the temperature changes shown by Q_2 and Q_3. In the cold portion of the orbit, no water is diverted towards the SRHX, and T_{H1} equals T_{C3}. By not diverting hot water towards the SRHX, the water within the hardware is allowed to freeze, so as to buffer the heat load during the hot portion of the orbit when the spacecraft exits eclipse. In the cold portion of the orbit, the ammonia has to be bypassed from the radiator to reduce the heat rejected, since the SRHX is no longer buffering the heat load.

The second location to augment the water loop is to place the SRHX on the cold side of the water loop. Putting the SRHX in this location would cool the water before reaching the air/water heat exchanger, rather than the water/ammonia heat exchanger. This alternative architecture is shown in Figure 18.

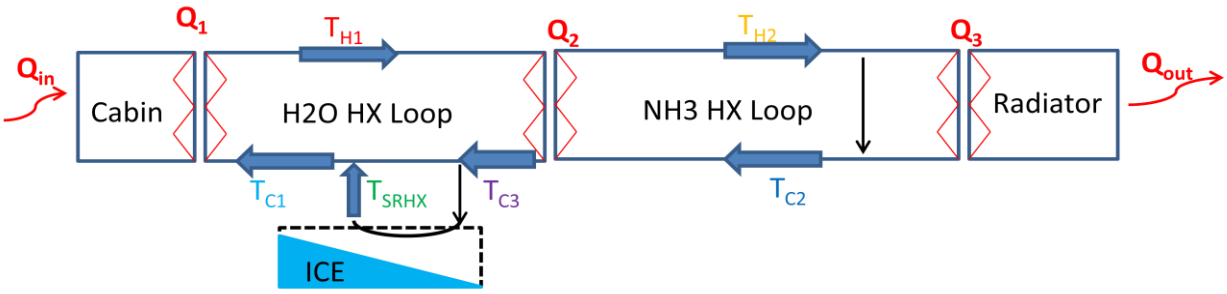

Figure 18: Alternative Architecture 3 Schematic, Augment Location 2

The architecture shown in Figure 18 is very similar to the other augmented option, shown in Figure 16. With the SRHX on the cold side of the H2O heat exchange loop, the SRHX works to cool down the water temperature before coming in contact with the air/water heat exchanger. The temperature trends for this alternate architecture are shown below in Figure 19.

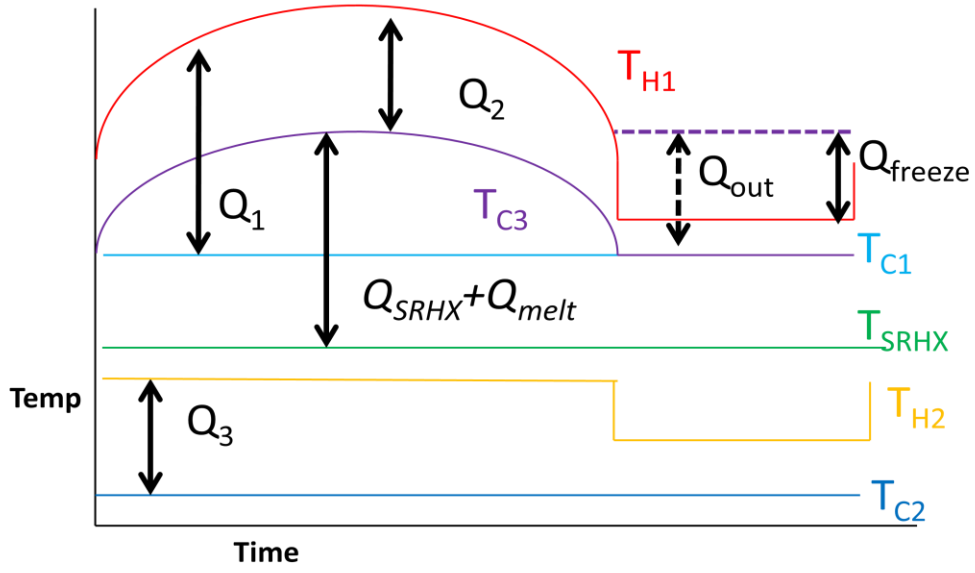

Figure 19: Alternative Architecture 3b Temperature Trends

The temperature trends are similar to that seen in Figures 10, 15, and 17. In this architecture, the water again is bypassed to the SRHX in the hot portion of the orbit, creating the temperature change from T_{C3} to T_{SRHX}. This cooled water combines with the T_{C3} temperature to bring the water temperature down to T_{C1} before the water/ammonia heat exchange takes place. The water/ammonia heat exchange causes the temperature changes shown by Q_2 and Q_3. In the cold portion of the orbit, no water is diverted towards the SRHX, and T_{C1} equals T_{C3}. By not diverting hot water towards the SRHX, the water within the hardware is allowed to freeze, so as to buffer the heat load during the hot portion of the orbit when the spacecraft exits eclipse. In the cold portion of the orbit, the ammonia has to be bypassed from the radiator to reduce the heat rejected, since the SRHX is no longer regulating the heat load.

Non-Viable Alternative Architectures

The SRHX was considered to replace or augment the ammonia loop. It was determined that the SRHX should not replace the ammonia loop, since a water/water-PCM connection in the architecture would be a redundant and inefficient way to transport heat. The SRHX was also considered as an augmentation to the ammonia loop. There were two locations considered for augmenting the ammonia heat load: placing the SRHX on either the hot side, or on the cold side of the ammonia heat exchanger. Neither location would allow for the ammonia to flow through the SRHX while being used (like in alternative architecture 3) since the ammonia and water PCM cannot mix without the fluid combining and changing the properties of both fluids. The only way to implement an augmentation was for the ammonia to flow beside the SRHX in a separate pipe to dissipate the heat load without the two fluids being mixed.

The ultimate reason why the SRHX could not be augmented on the ammonia loop side was due to the fact that ammonia would never be in the appropriate temperature range to utilize the heat of fusion for heat load buffering. The PCM can only be used to absorb heat if the temperature goes below the melting point of the PCM. Since ammonia has effective temperature ranges of -33 ºC to -78 ºC, and water does not melt until 0 ºC, the ammonia would never be hot enough to melt the PCM. Therefore, implementing the SRHX on the ammonia loop would not allow for heat regulation, or heat load buffering since the two fluids cannot mix, and ammonia has the wrong temperature range.

Validation of Architecture Trends

The ATCS used for previous human-rated missions varies depending on the regulations and technology available at the time. Spacecraft data for the International Space Station (ISS) and the Space Transportation System (STS) are based on functional hardware values, ever since the missions achieved spaceflight. Lunar based data comes primarily from the Orion and Altair projects, but since the missions were canceled in 2009 the data is theoretical. Mission data for each spacecraft thermal control systems was collected and is presented in Table 5 (Hanford and Ewert, 1996).

Table 5: Architecture Trends for Other Missions

System	Fluid(s)	No. of Loops	Line Dia (in)	Q_{max} (kW/loop)	m_{dot} (kg/s)	T_H (K)	T_C (K)	Total A_R (m^2)
ISS	Water/ NH_3	2	Not given	11.7	0.003 to 0.159	281 to 311	180 to 269	129.8
STS	Water/ Freon 21	2	Not given	18.8	0.2835 to 0.378	283 to 322	248 to 280	140.4
CEV	Propylene Glycol	1	Not given	6.25	0.05653	308	275	28
Lunar Lander	Water/ NH_3	1	Not given	16	0.0624 to 1.0239	276 to 301	Not given	116.1
Lunar Base	Water/ NH_3	3	1.0	16.7	0.4254 to 0.6807	278	Not given	651 (day) 217 (night)
Mars Lander	Water/ NH_3	3	1.0	10	0.34	278	Not given	353

The "fluids" category describes the working fluids that work within the ATCS. The "number of loops" describes the amount of heat exchanger loops within

the ATCS. The "line diameter" is the cross sectional width of the heat exchanger tubes. The "Q_{max}" is the maximum amount of heat that can be rejected via the ATCS. The mass flow rates of the working fluids are shown in the "m_{dot}" column. The "to" term between the values means the first value corresponds to the first loop, and the second value corresponds to the second loop. "T_H" and "T_C" are the temperatures of the working fluid before and after heat is transferred out. Lastly, the "A_R" column describes the area of the radiator used to reject the heat.

The working fluid selection is important to analyze when comparing architecture trends. The STS has Freon 21 in one of the loops. While Freon 21 has a high specific heat and acts as an effective working fluid, the material is highly toxic, and is no longer used in human-rated ATCS architectures. Therefore, STS trends are not compared to the SRHX trends. The ISS data is relevant since the two working fluids are the same fluids that are to be used in SRHX implementation architectures. The CEV utilizes a Propylene Glycol and water mixture as its only working fluid (NASA, 2005).

While slightly toxic, Propylene Glycol has a high heat capacity, and a low freezing point. Utilizing the Propylene Glycol allows for the working fluid to drop below the freezing point of water (273 ^{o}K) without the working fluid freezing up in the heat pipes. Since Propylene glycol is similar to ammonia, the CEV trends are a valid comparison to the SRHX architecture trends. The three interplanetary landers rely on a water and ammonia loop system, much like the ISS. However, the performances of the landers were idealized, since they were only in their conceptual

phase at the time of publication, so they were not included in comparison to the SRHX architecture trends. The SRHX architecture values were compared to those missions with similar characteristics.

Table 6: ATCS Specifications for Alternative Architectures

System	Fluid(s)	No. of Loops	Line Dia (in)	Q (kW/loop)	m_{dot} (kg/s)	T_H (K)	T_C (K)
ISS	Water/ NH_3	2	Not given	11.7	0.003 to 0.159	311 to 281	269 to 180
CEV	Propylene Glycol	1	Not given	6.25	0.05653	308	275
Baseline	Water/ NH_3	2	1	2.46-1.19	.101 to (0.159-0.077)	(304-286) to (223-227)	280 to 220
SRHX	Water PCM	1	1	2.46-1.19	.101-0.488	296-279	273
SRHX/ NH_3	Water PCM/ NH_3	2	1	2.46-1.19	(0.101-0.488) to 0.159	(296-279) to 205	273 to 200
H20/SRHX/ NH_3	Water/ PCM/ NH_3	3	1	2.46-1.19	.101 to (0-0.260) to 0.159	(304-286) to 273 to (223-227)	280 to 233 to 220

In Table 6, the terms in parenthesis show the range of mass flow rates and hot temperatures an individual loop will encounter. For instance, the baseline ammonia loop will vary the mass flow rate from 0.159 kg/sec to 0.077 kg/sec from orbit noon to eclipse, and the hot side temperature of the ammonia will vary from 223-227 ºK. The "Q" value for the architectures was determined based on the maximum and minimum heat loads from the orbital models. The mass flow rates for the baseline and alternate architectures were chosen based on test points for the SRHX (described in detail in Chapter IV). The outlet temperature (T_C) was assumed to be constant for each model. The water loop outlet temperature was assumed to be 280 ºK in non-SRHX loops to prevent the water from freezing. The outlet

temperature for the SRHX was assumed to be 273 ºK for the SRHX, since the water is allowed to freeze within. The 273 ºK outlet temperature is an idealized condition that can be achieved through a sufficiently long heat exchanger, but sense the SRHX is only twelve inches long, the outlet temperature will likely be below the idealized point. The outlet temperature for the ammonia loop was assumed to be 220 ºK to prevent the ammonia from freezing the water at the water/ammonia heat exchanger. In the SRHX/NH3 configuration the ammonia has a lower outlet temperature (200 ºK) just above the ammonia freezing point. The lower temperature is chosen because the ammonia loop is allowed to freeze the water in the SRHX. The hot temperature range is calculated from the increase in temperature needed to reject the heat loads.

Overall, the outputs for the hot temperatures are similar to the ISS and CEV temperature trends. The heat loads and mass flow rates are different between the missions, but the predicted increase in temperatures follow similar trending. It is difficult to validate the temperature trends from the SRHX, since neither the ISS nor the CEV contain a PCM to buffer the heat loads. Overall, the similar trends validate the temperature change calculations for each architecture in the maximum and minimum heat load conditions.

SRHX Hardware Modeling

The third aim (Aim 3) of the thesis was accomplished through modeling the SRHX outputs with specified steady state and dynamic test conditions. The following section describes the equations used to predict the SRHX outputs, and the

unique features enabled by the water freeze within the SRHX that determine whether / how this component might be utilized within a spacecraft ATCS.

For purposes of analysis, it was assumed that the SRHX would be capable of rejecting all of the heat absorbed by the air/water heat exchanger. The performance of the SRHX is described and calculated below. The results cannot be validated through heuristics since this is a new and unique technology. Instead, the results are used to predict the performance of the hardware, which will be compared to the actual results from the physical hardware characterization tests (Chapter IV).

SRHX Equations

The SRHX utilizes both the material properties of the hardware, and the energy stored within the PCM to regulate the heat loads. The physical setup of the SRHX interior is shown below.

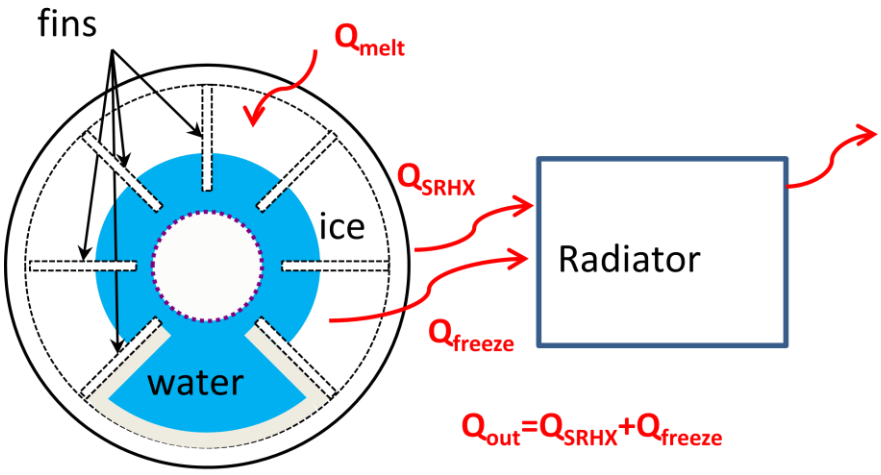

Figure 20: Cross Sectional View of the Modeled SRHX and Ice Buildup

In Figure 20, the black lines represent the physical SRHX hardware. The white portion represents the ice freeze within the SRHX. The blue portion is the

flow path for the working fluid to travel through. Figure 20 shows seven fins, though this number can be varied depending on the chosen hardware. The radiator is shown as a white box, connected to the outer shell of the SRHX.

To maintain thermal equilibrium, the incoming heat load to the cabin must be transported through the SRHX or rejected through melting of the PCM.

$$Q_{in}\ t\ = Q_{SRHX}(t) + Q_{melt}(t) \tag{33}$$

The ice melt, represented by a positive Q_{melt} (W), occurs when the SRHX surface area exposure is undersized, and cannot absorb all of the heat from the water. In this case, the heat of fusion from the ice melt is used to absorb the excess heat load. The SRHX absorbs heat from the water through the following equation:

$$Q_{SRHX}(t) = \frac{k*[Ti-Tw]*A_s(t)}{2*[n_{fins}-1]*r_{fin}} \tag{34}$$

Equation 34 is a modification of the general conductive heat transfer, described in Equation 2. The Ti term in the numerator is the temperature of the water coming into the SRHX (^oK). The Tw term is the temperature of the SRHX wall (^oK). The As(t) is the amount of SRHX surface area exposed to the working fluid at time 't' (m^2), and r_{fin} is the length of the SRHX fins (m). The n_{fins} term is the number of fins present absorbing heat. This term is subtracted by one to account for one side of two fins being insulated. The 2 coefficient in the denominator is to indicate that both sides of the fins are absorbing heat.

The heat rejected from the radiator (Q_{out}) is equal to the amount of heat transported through the SRHX, and the amount of heat used to freeze up the PCM.

$$Q_{rad} = Q_{out} = Q_{SRHX}(t) + Q_{freeze}(t) \quad (35)$$

In Equation 35, Q_{freeze} is assumed to be a negative term, since it is absorbing excess heat rejection from the radiator. The amount of heat rejected from the radiator is assumed constant, while the amount of heat transported out of the SRHX (Q_{fins}) and into the water is dependent on the amount of ice within the SRHX. The water will only freeze if the incoming heat load is less than the amount of heat rejected from the spacecraft. If the fins are undersized for an incoming heat load, the heat load is partially absorbed by the PCM.

$$Q_{in}\ t\ = Q_{fins}(t) + Q_{melt}(t) \quad (36)$$

The excess heat load that goes into melting the ice (Q_{melt}) is not transferred to the radiator, since that heat was spent in the phase change process. Q_{melt} is considered to be a positive term, since it is absorbing the incoming heat load. All terms are time dependent, relative to orbital heat load conditions and ice buildup within the SRHX. The Q_{freeze} and Q_{melt} terms can be combined into a single term, Q_{PCM} that describes the dynamics of the PCM fusion.

$$Q_{PCM}\ t\ = \frac{Q_{fins}(t) - Q_{out}}{\frac{dm_{ice}}{dt} * H_{fus}} - \frac{Q_{in}(t) - Q_{fins}\ t}{(\frac{dm_{ice}}{dt} * H_{fus})} \quad (37)$$

In Equation 37, H_{fus} is the amount of energy that must be absorbed to melt a given mass of the substance (kJ/kg). The rate of ice formation (dm_{ice}/dt) is the rate of mass of ice melted or frozen (kg/sec). The rate of ice formation can be positive, or negative, depending on if the ice is melting or freezing. The change in mass will be greatest when the fins are most drastically over or undersized, most likely when the spacecraft is going into eclipse, or coming out.

SRHX Heat Rejection Modeling

The SRHX heat rejection modeling is used to demonstrate the conjunction of the SRHX material conduction and the PCM fusion. The model assumes that the SRHX is able to maintain thermal equilibrium through the variation of orbital heat loads. The heat loads shown in Figure 6 are used as an input estimate for the SRHX to absorb and reject. The modeling of the SRHX hardware involves estimating the amount of ice and fin size exposed within the SRHX, based on the thermodynamic equations of heat transfer. The heat loads into the spacecraft, and ideal response of the SRHX are shown below in Figure 21.

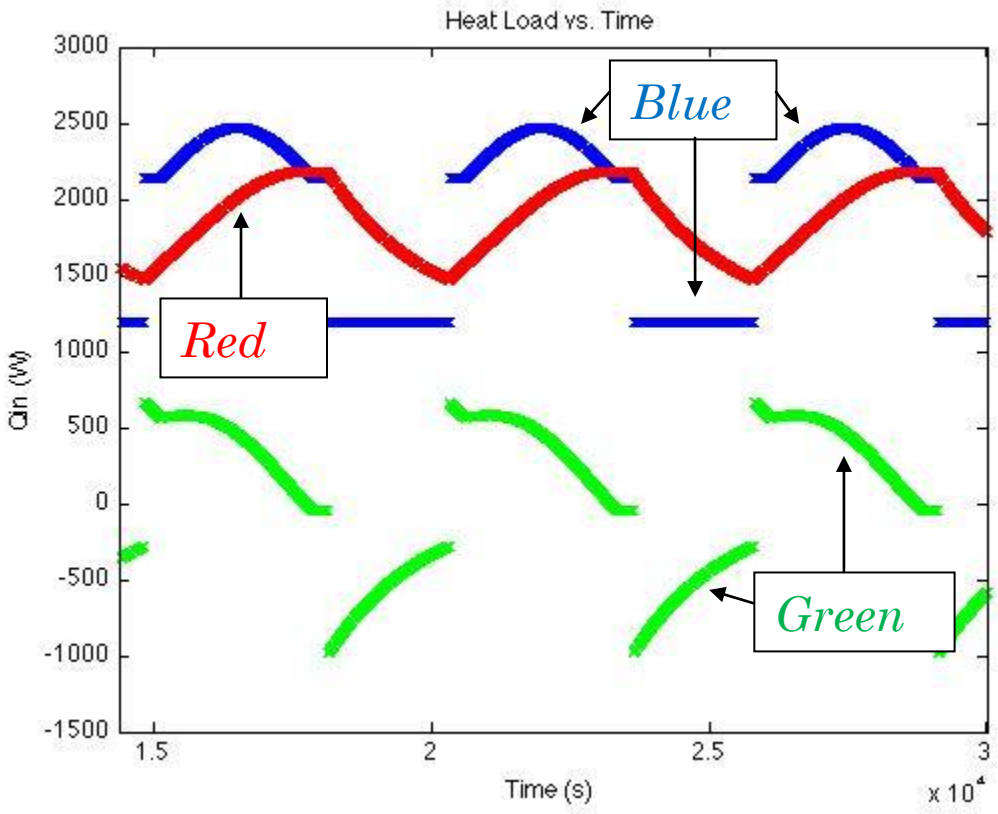

Figure 21: Heat Loads Into and Out of a Spacecraft in Thermal Equilibrium

The blue line is the heat coming into the spacecraft. The red line is the amount of heat rejected through the fins. The green line is the amount of heat rejected through the PCM melt. Whenever the red line is lower than the blue line, the fins are undersized for the heat load condition, and the heat of fusion from the ice melt must make up for the difference in order to maintain thermal equilibrium. As the ice melts, more fin size is exposed, leading to more heat rejection through the fins. As the heat load decreases, the fins become oversized for the heat load coming into the spacecraft. In this case, the difference between the blue and red line is the heat used to freeze up the water (hence the negative values).

While the results look similar to that expected from SRHX performance, there is no way to tell how accurate the model is without testing the hardware itself. Unfortunately, the validation of trends shown in Figure 21 require detailed measurements of the dynamic change in ice formation, heat loads, and fin exposure. The scope of the thesis only allowed for steady state tests of the SRHX to be performed in the time allotted. Therefore, the predictions shown in Figure 21 have not been verified.

SRHX Temperature Modeling

For the SRHX temperature analysis, the SRHX will be assumed to be in a steady state configuration. The steady state configuration implies that the SRHX will maintain a constant outlet temperature for constant test conditions. The test conditions include inlet temperature, mass flow rate, and SRHX wall temperature.

These inputs are the test points used for the steady state testing of the SRHX. The description of each term, along with the input range is described in Chapter IV.

The temperature change caused by the SRHX is due to the heat transfer out of the water. Assuming all heat from the cabin is transferred into the working fluid, the heat must be then rejected from the fluid on the other side of the ATCS to maintain thermal equilibrium. The water loses temperature based on the heat transfer shown in Equation 27, shown again below.

$$Q_{wf} = (m * c_{p_{H20}} * [T_{H1} - T_{C1}]) \tag{27}$$

Given a constant mass flow rate (m), a constant inlet temperature (T_{H1}), and a known specific heat (c_{p_H20}), there are only two terms in Equation 27 left unknown: the overall heat load (Q_1) and the outlet temperature (T_{c1}). The outlet temperature and heat transfer can be calculated through three methodologies.

Working Fluid Equations

The working fluid methodology assumes a heat load, and solves for the required outlet temperature. The assumed heat loads are based on the orbital heat load modeling: eclipse heat loads (1190.1 W), dayside heat loads with no albedo (2133.5 W), and dayside heat loads in full albedo heat load exposure (2463.7 W). These three heat loads correspond to the range expected from a typical LEO spacecraft, as seen in Figure 6. The SRHX is expected to reject these heat loads in order to maintain thermal equilibrium onboard the spacecraft. By setting the heat load, the outlet temperature can be solved with simple algebra.

$$T_{C1} = T_{H1} - \frac{Q_1}{m_1 * c_{p\_H20}} \tag{38}$$

This model does not take the radiator temperature into account. The heat load is assumed to be a function of solely mass flow rate and inlet temperature. These assumptions are good for a first round analysis, but the results predict a solution (Q_1) rather than trying to solve for it. Ideally, the performance of the SRHX should be predicted based on the input parameters, rather than a desired output. To accomplish this, thermodynamic equations are used to obtain solutions based solely on input conditions.

Thermodynamic Equations

The second means of calculating the outlet temperature is by way of looking at the thermodynamics involved in the heat transfer. The heat transferred out of the working fluid is equal to the convective heat transfer out of the water flowing through the SRHX. The equations were broken down into their individual components for calculations.

$$m * c_{p\_H20} * \Delta T = h * A_s * \Delta T \tag{39}$$

The first term is the heat transferred from the working fluid, and the second term is the convective heat transferred from the working fluid. The ΔT terms in Equation 39 are assumed equal. The mass flow rate and specific heat are given, and the surface area (A_S) is calculated by the following equation.

$$A_s = m * \frac{c_p}{h} \tag{40}$$

The primary term that needs to be calculated is the convective heat transfer coefficient (h). The convective heat transfer coefficient needs to be calculated individually for the fins, and the tube. The convective heat transfer coefficient for

the fins is calculated based on the Churchill-Chu correlation, assuming a uniform temperature vertical configuration (Churchill and Chu, 1975).

$$h_{fin} = \frac{k}{L}(0.825 + \frac{0.387Ra^{\frac{1}{6}}}{[1+[\frac{0.492}{Pr}]^{\frac{9}{16}}]^{\frac{8}{27}}})^2 \quad (41)$$

In Equation 41, "k" is the thermal conductivity of the fin, "L" is the characteristic length of the SRHX fins, Ra is the Rayleigh number of the water, and Pr is the Prandtl number of the water. The thermal conductivity and characteristic length of the fins are given through hardware specifications. Only the Rayleigh number and the Prandtl number are left to be to be calculated. The Prandtl number is calculated through Equation 42.

$$Pr = c_{PH20} * \frac{\mu}{k_{H2O}} \quad (42)$$

In Equation 42 "μ" is the dynamic viscosity of the water, assumed to be a constant 0.001002 Pa*s (Watson, et al. 1980). The k_{H2O} term is the thermal conductivity of water at 290 °K, assumed to be a constant 0.60 W/m*K. The Rayleigh number in Equation 41 can be calculated in two ways. One means of estimating the Rayleigh number is through the following equation (Qiu and Tong, 2001).

$$Ra = (11.76Re)^{2.198} \quad (43)$$

In Equation 43, "Re" is the Reynolds number of the fluid, calculated through Equation 44.

$$Re = \frac{\rho V D_i}{\mu} \quad (44)$$

The Reynolds number is calculated by taking into account the density (ρ), velocity (V), and dynamic viscosity of water (μ), along with the effective diameter of the SRHX (Di). The cross sectional area is calculated through Equation 45.

$$A_c = \pi(\frac{Di}{2})^2 \tag{45}$$

In Equation 45, Di is the inlet diameter of the SRHX (m). The velocity of the water is calculated through Equation 46.

$$V = m\rho^{-1}A_c \tag{46}$$

From Equations 41-46, the convective heat transfer coefficient can be found for the fins. However, Equation 43 is only used as an estimate for the Rayleigh number. The Rayleigh number estimate only takes the mass flow rate into account, while ignoring the effects of the water temperature and SRHX wall temperature. A more robust equation can be used for calculating the Rayleigh number, which takes more environmental terms into account (Cengel, 2003).

$$Ra = GrPr \tag{47}$$

Where Gr is the Grashof number, calculated for both the fins and the tube in series.

$$Gr_x = [\frac{1}{Gr_{fin}} + \frac{1}{Gr_{tube}}]^{-1} \tag{48}$$

The Grashof number for the fins is calculated through the following equation (Cengel, 2003).

$$Gr_{fin} = \frac{g\beta[T_{in} - T_{wall}]L^3}{v^2} \tag{49}$$

Where 'g' is the local acceleration due to gravity, T_{wall} is the temperature of the SRHX wall, T_{in} is the temperature of the water entering the SRHX, "L" is the

characteristic length of the fins, and "v" is the kinematic viscosity of the water, and is the volumetric thermal expansion coefficient. The volumetric coefficient is calculated, assuming an ideal fluid, as (Cengel, 2003):

$$\beta = \frac{1}{T_{in}} \tag{50}$$

And the kinematic viscosity is calculated as (Cengel, 2003):

$$v = \frac{\mu}{\rho} \tag{51}$$

The Grashof number for the tube is calculated from the following equation (Cengel, 2003).

$$Gr_{tube} = \frac{g\beta[T_{in} - T_{wall}]D^3}{v^2} \tag{52}$$

With all terms the same as Equation 49, except the 'D' term, which is the diameter of the SRHX tube. With the two means of calculating the Rayleigh number (Equations 43 and 47) the convective heat transfer coefficient for the fins can be found in two separate ways.

The next step is to find the convective heat transfer coefficient of the SRHX tube (Cengel, 2003).

$$h_{tube} = \frac{2k}{D_i * ln(\frac{D_o}{D_i})} \tag{53}$$

In Equation 53, Di is the inlet diameter of the SRHX (m), and Do is the outlet diameter of the SRHX (m), found by taking the thickness into account.

$$D_o = D_i + 2x \tag{54}$$

In Equation 54, "x" is the thickness of the SRHX wall (m).

Having the convective heat transfer coefficient for both the fins and the tube of the SRHX, the overall heat transfer heat coefficient can be calculated by assuming the two objects are working in parallel to dissipate the heat.

$$h = \frac{1}{\frac{1}{h_{fin}} + \frac{1}{h_{tube}}} \tag{55}$$

Now that the convective heat transfer coefficient is found, the outlet temperature of the SRHX can be found by taking the conductivity of the SRHX into account. It is assumed that in the steady state condition, the heat transferred out of the working fluid is equal to the heat transferred into the SRHX metal.

$$Q_{wf} = Q_{conductive} \tag{56}$$

The heat terms can then be broken down further.

$$m * c_{p\_H20} * \Delta T = k * A_s * \nabla T \tag{57}$$

In Equation 57, "∇T" is the radial temperature gradient of the SRHX.

$$\nabla T = \frac{Ti - Tw}{r_{fin}} \tag{58}$$

The terms within Equations 57 and 58 can be separated to solve for the outlet temperature.

$$T_o = T_i - \frac{k*[Ti-Tw]*A_s}{r_{fin}*m*c_p} \tag{59}$$

By replacing As with the terms from Equation 40, one can solve for the outlet temperature with the given inlet parameters.

$$T_o = T_i - \frac{k*[Ti-Tw]}{r_{fin}*h} \tag{60}$$

This equation is further modified to take the number of fins into account, the insulation of two fins, and the amount of ice buildup within the SRHX.

$$T_o = T_i - \frac{k*\ Ti-Tw\ \frac{A_S}{A_{Smaximum}}}{2*\ n_{fins}-1\ *r_{fin}*h} \quad (61)$$

A scaling factor of the ratio of surface area exposed (As) over maximum surface area ($As_{maximum}$) was included to account for the reduction of conduction due to ice presence within the SRHX. This scaling factor reduces the temperature gradient by increasing the wall temperature proportionally to the presence of ice. In doing so, the T_w value goes towards 0 °C as more heat is transferred to the ice, rather than the SRHX wall. The n_{fins} term is the number of fins present absorbing heat. This term is subtracted by one to account for one side of two fins being insulated. The 2 coefficient in the denominator is to indicate that both sides of the fins are absorbing heat.

Previous SRHX Testing Equations

The last means of calculating the outlet temperature of the SRHX is by using the results of previous SRHX testing. The previous testing utilized a 0.75 inch outer diameter, by 8 inch long tube, with six equally spaced fins. The tube was constructed out of Al6061 aluminum, and the fins were constructed with a thermograph 800 carbon composite material (Nabity, 2008). The 8 inch long, .75 inch diameter, 6 fin configuration is a different geometry and material than the SRHX being analyzed in this thesis. The SRHX being analyzed is 12 inches long, with a 1 inch diameter, and contains 7 AL6061 aluminum fins (see Chapter IV). Though the hardware is different, the results from previous testing are assumed to reasonably predict the results from a similar piece of hardware. The results of the

SRHX testing were used to describe the heat transfer to the SRHX by using the following equation:

$$Q_{SRHX} = U_{SRHX} * A_s * LMTD \tag{62}$$

In Equation 62, the LMTD term is the log mean temperature difference of the SRHX. The LMTD expression is calculated by taking the inlet, outlet, and wall temperature of the SRHX into account.

$$LMTD = \frac{((T_{in} - Twall) - (T_{out} - Twall))}{ln(\frac{T_{in} - T_{wall}}{T_{in} - T_{out}})} \tag{63}$$

U_{SRHX} term in Equation 62 is the overall heat transfer coefficient, measured in units of W/m2K. The U_{SRHX} term was determined through numerical results to be the following:

$$U_{SRHX} = 2524 * (A_s * LMTD)^{0.332} \tag{64}$$

By combining Equations 63 and 64, the heat transferred to the heat exchanger can be expressed as:

$$Q_{SRHX} = 2524 * (A_s * LMTD)^{1.332} \tag{65}$$

The heat to the SRHX must equal the amount of heat going out of the working fluid in steady state conditions.

$$Q_{SRHX} = Q_{wf} \tag{66}$$

With Equation 65, the mass flow rate, inlet temperature, and wall temperature are all included, leaving only the outlet temperature as an unknown. By using MATLAB, one can iterate through T_o values until the difference between the heat to the SRHX and out of the working fluid are within .01 Watts of one another.

TDA used past test data on a different SRHX to predict another value for the overall heat transfer coefficient. The previous SRHX test data were collected and used as inputs for an overall model. The temperatures were controlled, and the exposed area was predicted for each test point. The exposed surface area remains one of the biggest points of uncertainty in the calculation. The results gave a functional estimate that allowed the overall heat transfer coefficient to be determined. The test-based overall heat transfer coefficient is presented in Equation 67.

$$U_{SRHX} = 528 * (A_s * LMTD)^{1.33} \quad (67)$$

The integer coefficient for Equation 67 is much lower than that found in Equation 64, and the exponential term has increased. This indicates that for large values of (As*LMTD) Equation 67 will produce a higher overall heat transfer coefficient than Equation 64. However, the (As*LMTD) term is generally a small term since the area is limited within the SRHX to a maximum value of 0.0538 m^2. Therefore, the test-based overall heat transfer coefficient equation leads to a smaller solution in most cases. A graphical representation of the two methods of computing the overall heat transfer coefficient (Equations 64 and 67) is shown below in Figure 22.

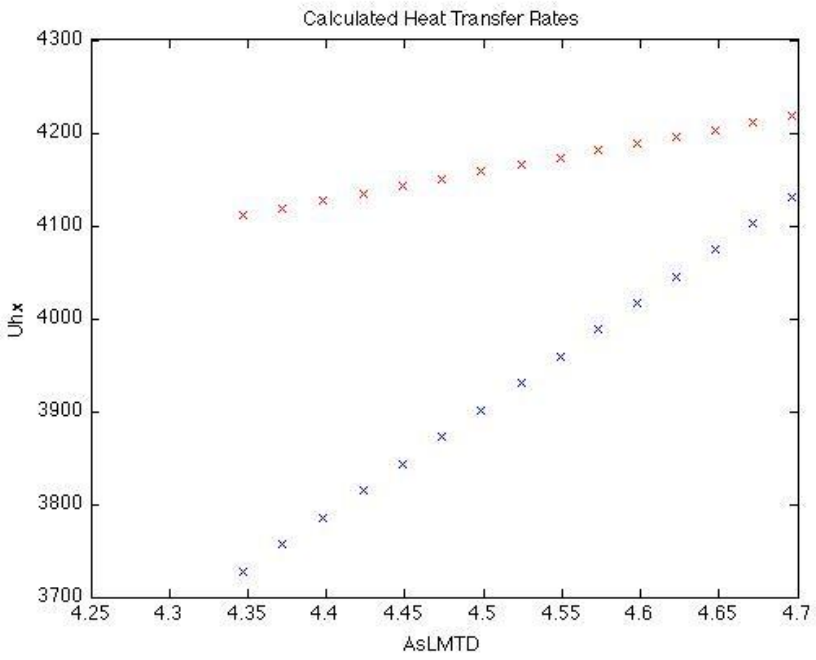

Figure 22: Overall Heat Transfer Coefficient Calculated with Outlet Temperatures from 15-0 Celsius. Blue=Equation 67, Red=Equation 64

In Figure 22, the maximum surface area is assumed to be exposed within the SRHX. The wall temperature of the SRHX is set at -80 ºC, and the inlet temperature is set at 25 ºC. The outlet temperature is iterated from 15 to 0 ºC for both equations. The lower the outlet temperature, the higher the LMTD term, which indicates the lowest T_o term (0 ºC) is on the far right of Figure 21. The blue line approaches, but never reaches the red line, indicating that Equation 67 leads to a lower overall heat transfer coefficient for all conditions than Equation 64 does.

Other test conditions were evaluated, with varying inlet temperatures, wall temperatures and exposed surface area. For all other conditions, the overall conclusion was the same: Equation 67 leads to a lower overall heat transfer coefficient than Equation 64. However, for lower input values, Equation 67 diverges further from Equation 64. Figure 21 was chosen to show the most dramatic

trending comparison between the two equations. Further results for the comparison between the two equations can be seen in APPENDIX B.

It should be noted that both equations used in this approach contain uncertainties. The equations were determined with experimental and computational methodologies, but the volume of experimental data was limited, and the computational program made many assumptions about the hardware performance. More importantly, the equations were based off of a smaller SRHX than the one utilized in the test, and the materials within the two sets of hardware were different. Therefore, while the equations may adequately describe the performance of the 8 inch x .75 inch heat exchanger, the larger, 12 inch x 1 inch SRHX will likely diverge away from the expected trends. The equations for the overall heat transfer coefficient of the 12 inch x 1 inch SRHX need more experimental validation to improve the accuracy of the equations.

SRHX Pressure Difference Modeling

The difference in pressure across the SRHX is the second output to the SRHX test. The change in pressure is used to evaluate the blockage due to the buildup of ice within the SRHX. With a constant mass flow rate, the change in pressure is correlated to flow area reduction within the SRHX due to ice formation. The maximum pressure difference is also used to size the pump output pressure requirements on orbit.

To model the change in pressure at the outlet of the SRHX, some simplifying assumptions were necessary. It was assumed that: the ice melt would be conical, the

water would flow through the center of the heat exchanger, and the ice melts first around the hotter inlet, and then around the colder outlet. The pressure difference is calculated from Bernoulli's equation:

$$\frac{p_1}{g\rho} + \frac{{v_1}^2}{2g} + z_1 = \frac{p_2}{g\rho} + \frac{{v_2}^2}{2g} + z_2 \tag{68}$$

In Equation 68, "p" is the pressure (Pa), 'g' is the acceleration due to gravity (m/s^2), ρ is the density (kg/m^3), 'v' is the velocity of the fluid (m/s), and 'z' is the height (m). The 1 subscript signifies the inlet of the SRHX, and the 2 subscript signifies the outlet. Since the height and gravity are assumed to be the same on both the inlet and outlet sides, the equation simplifies to:

$$p_2 - p_1 = \Delta p = \frac{\rho[v_1^2 - v_2^2]}{2} \tag{69}$$

The velocity terms can be calculated assuming a constant mass flow rate through the SRHX. The mass flow rate can be defined as:

$$m = \rho_1 v_1 A_{c_1} = \rho_2 v_2 A_{c_2} \tag{70}$$

Assuming that the densities are equal throughout the SRHX, Equation 70 can be rearranged to show:

$$\frac{v_1}{v_2} = \frac{A_{C2}}{A_{C1}} \tag{71}$$

The area of the inlet and outlet can be found through determining the radius of the cross sectional flow. The cross sectional area is calculated assuming a circular melt pattern:

$$A_{cx} = \pi {r_x}^2 \tag{72}$$

In Equation 72, the 'x' subscript can be either 1, or 2, depending on whether the inlet or outlet side of the SRHX is being solved for. The radius of the inlet (r_1) is assumed to be one half the maximum diameter of the SRHX if the area exposed on the interior of the SRHX is greater than one half of the maximum SRHX surface area. The outlet radius is calculated by using the following equation:

$$r_2 = ((\frac{D_{inlet}}{2} - r_{between}) * \frac{A_s - .5A_{s_{maximum}}}{.5A_{s_{maximum}}}) + r_{between} \tag{73}$$

In Equation 73, the $r_{between}$ term is the insulated area that is assumed to always be free from ice, allowing for flow to pass by in all conditions. The $\frac{A_s - .5A_{s_{maximum}}}{.5A_{s_{maximum}}}$ term is the ratio for the outlet flow area relative to the maximum flow area. The .5 coefficient before the maximum surface area in the numerator and denominator takes into account the conical melt geometry. If the A_s term is exactly one half the maximum surface area, the first expression in Equation 73 will go to zero. If the A_s term is equal to the maximum surface area, the outlet side will be computed to be fully melted, and equal to the inlet diameter.

The inlet ratio needs to be calculated if the exposed surface area is computed to be less than one half of the maximum surface area. In that case, the outlet radius is assumed to be minimized, and equal to $r_{between}$. The inlet radius can then be calculated as:

$$r_1 = ((\frac{D_{inlet}}{2} - r_{between}) * \frac{A_s}{.5A_{s_{maximum}}}) + r_{between} \tag{74}$$

Equation 74 is similar to Equation 73, except that the numerator of the $\frac{A_s}{.5A_{s_{maximum}}}$ term no longer has half of the maximum surface area subtracted. This is because this calculation is only used if the surface area in the SRHX is less than one half of the maximum surface area already.

Combining Equations 69 through 74 allows for the change in pressure to be calculated. The change in pressure is low for high levels of ice presence and low levels of ice presence, since those are the two conditions where the inlet and outlet areas are similar in size. The configurations for the low changes in pressure are shown below in Figure 23.

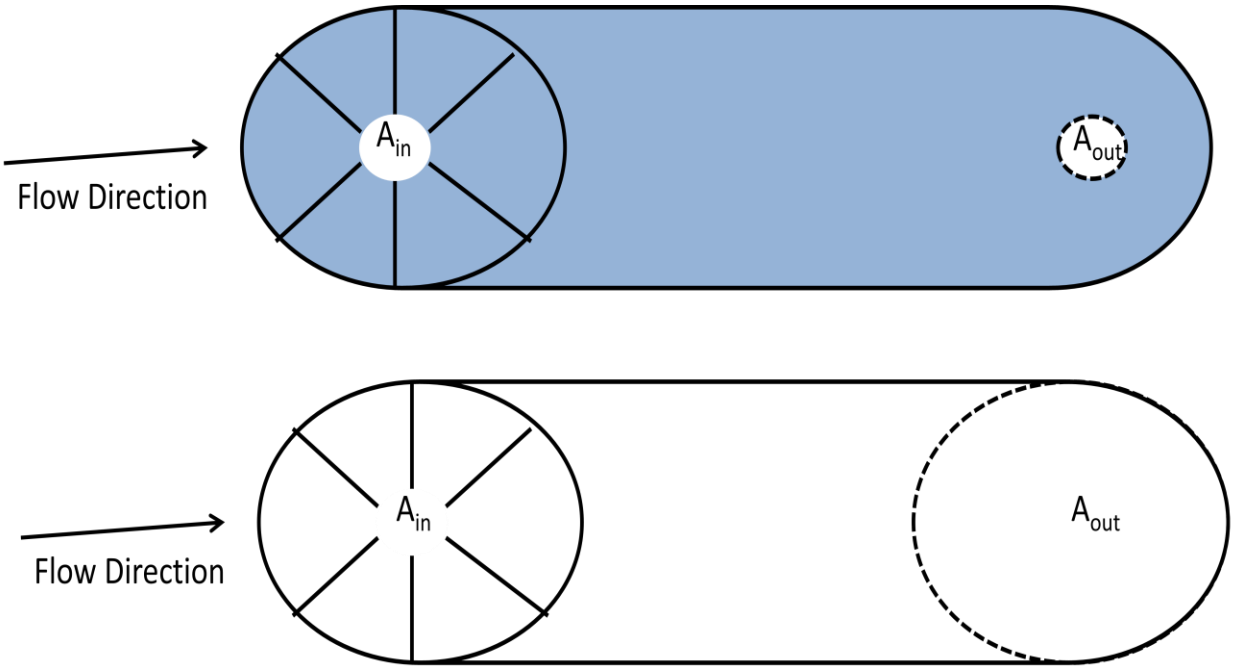

Figure 23: Minimum Pressure Difference Configurations

The black lines in Figure 23 represent a simplified three dimensional model of the SRHX shell and fins. The blue area is the ice, and the lines on the inlet side of

the SRHX are the fins that extend down the interior of the SRHX. In both configurations, the area is similar between the inlet and outlet of the SRHX, meaning the change in pressure is nearly zero.

The maximum pressure change occurs when half of the fin area is exposed. In that case, the ice around the inlet is entirely melted, but the outlet side has yet to experience any ice melt. This creates the largest change in areas from the inlet to the outlet, leading to the highest change in pressure. This configuration is shown in Figure 24.

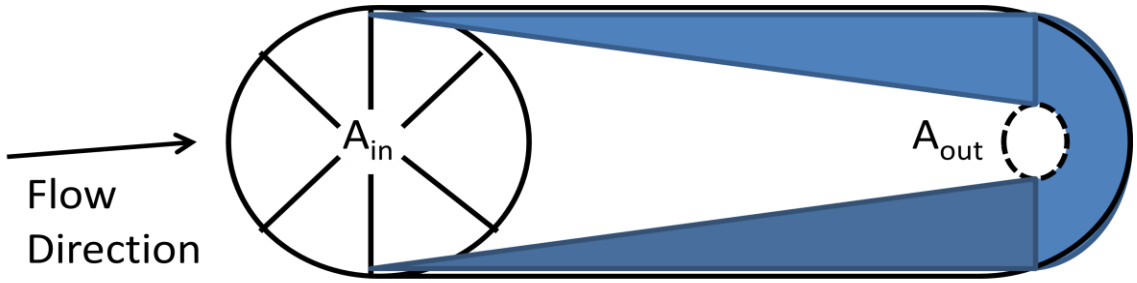

Figure 24: Maximum Pressure Difference Configuration

In Figure 24, the blue area is the ice, and the lines on the inlet side of the SRHX are the fins that extend down the interior of the SRHX. In this configuration, the inlet area is maximized, and the outlet area is minimized. To maintain a constant mass flow rate, the velocity will need to increase through the smaller area on the outlet side of the SRHX, which in turn, increases the pressure.

Though the conical assumption is a reasonable ice melt model for an ice-in-heat-exchanger configuration, the actual hardware does not act in such a fashion. The actual hardware contains insulated channels for the water to pass through

instead of a middle portion for the water to flow through, as seen in Figure 3. The insulated channel and the variable middle area that allows for ice expansion is a difficult geometry to represent through mathematical equations. Though the actual and modeled hardware are not exactly similar, the conical melt assumption matches up with the basic geometry seen in the computational fluid dynamics models that TDA created. Therefore, the conical melt assumption is a reasonable method to utilize in the calculation for pressure difference.

CHAPTER IV

TESTING AND ANALYSIS

The third aim (Aim 3) of the thesis was accomplished using Chapter III equations to obtain theoretical predictions of SRHX output. The fourth aim (Aim 4) of the thesis is to compare the predicted performance of the SRHX against the test results under theoretical scenarios to assess feasibility. The feasibility of the SRHX is based on whether the SRHX can utilize water as the working fluid, and whether the SRHX can self-regulate its heat rejection through ice buildup under the specified thermal conditions. The first set of tests demonstrates the heat regulation capabilities in a steady state condition. After the first set of tests was completed, the original plan was to test the self-regulation capabilities using dynamic inputs. The dynamic tests were to be used to determine the rate of ice melt and formation, and how that affects the rate and regulation of heat rejected from the SRHX. However, the dynamic tests were not able to be accomplished by the time of writing this thesis, so the test data are focused on steady state performance.

To characterize the heat exchanger, a series of steady state heat transfer conditions were tested at the TDA laboratory in Wheat Ridge, Colorado. To achieve steady state conditions during the test, the mass flow rate, inlet water temperature, and wall temperature are kept constant until the outlet measurements are no longer changing in time. When the outlet measurements are constant, the ice formation is no longer changing, and a constant amount of heat is being rejected out

of the water. Since the ice is not being melted or frozen in the steady state condition, all heat transferred out of the water is absorbed through the SRHX itself.

A dynamic test is used to demonstrate the capability of heat rejection through heat of fusion by the PCM, which will only occur during transient thermal conditions. Therefore, the inlet water temperature, the mass flow rate, or both are altered during the test to vary the amount of ice present. With a changing amount of ice within the SRHX, the exposed area will change as well, which demonstrates the dynamic self-regulation capabilities of the SRHX. The theoretical outputs of the dynamic self-regulation test are presented last.

Proposed Test Plan Rationale

The first round of testing is meant to characterize the performance of the 7-finned 12" long by 1" diameter heat exchanger made from Al6061-T6 alloy a series of steady state heat transfer experiments were conducted under thermal loads characteristic of orbital space flight. TDA is also constructing a 7-finned, K1100 carbon fiber material within an Al6061-T6 Aluminum cylinder SRHX, but as of the time of this writing, the construction of the secondary SRHX is incomplete; only the all aluminum heat exchanger was studied. To achieve steady state conditions, the mass flow rate, inlet water temperature, and external wall temperature were kept constant until the outlet water temperature and pressure reach equilibrium. When the outlet measurements are no longer changing, a constant amount of heat is being rejected out of the water. In this steady state condition, all heat transferred out of

the water was rejected through the SRHX structure, and none through PCM melting, which was stabilized.

There are three inputs to the SRHX test and two measured outputs. The three inputs are: inlet water temperature (T_{in}), heat exchanger wall temperature (T_{wall}), and water mass flow rate (m_{dot}). The two test outputs are: outlet water temperature (T_{out}), and delta pressure (ΔP) across the heat exchanger. Three different values were selected for each input, leading to 27 tests overall, and 54 output measurements. The test results were used to determine three conclusions. First, the test characterized the range of heat rejection that can occur through the fins at different conditions (Q_{max} and Q_{min}). This result was used to help determine the spacecraft orbit criteria that for which the SRHX could be effectively utilized within an ATCS. Second, the test results gave an indication of the required wall temperature for the range of heat rejection rates, which corresponds to the radiator temperature onboard a human rated spacecraft. Finally, the efficiency of the SRHX was used to establish the difference between the predicted and empirical T_{out} and ΔP values.

Test Input Definitions

Wall Temperature (Twall)

The SRHX wall temperature will use test points of -20 ºC, -40 ºC, and -80 ºC. This range is representative of typical LEO radiator surface temperatures (Hanford,

2006) and corresponds to the set points used to test the prior SRHX designs that Equations 64 and 67 were based upon (Nabity, 2008).

The wall temperature is maintained by providing a controlled fluid temperature set to the desired test point and immersing the SRHX in the circulating bath. The SRHX wall temperature was allowed to reach equilibrium with the bath. The various water inlet temperatures and mass flow rates were then tested sequentially at the constant wall temperature.

Inlet Temperature (Tin)

The inlet temperatures of the SRHX testing were set at values of 15 ºC, 20 ºC, and 25 ºC. This range is representative of the typical temperature range that was maintained in the space shuttle orbiter cabin atmosphere, which operated between 65-80 ºF (18.3 ºC – 26.6 ºC) (Mills-Alford, 2008). The working transport fluid must be colder than the cabin temperature to allow for heat transfer to occur from the cabin to the water. Therefore, the temperature exiting the air/water cabin heat exchanger must be below this operating value. The minimum inlet temperature of 15 ºC was selected to represent the cold condition onboard the spacecraft where the input heat load is at its minimum. The maximum inlet temperature of 25 ºC was chosen to approximate the maximum operating temperature in the spacecraft (26.6 ºC). The 20 ºC inlet temperature is chosen as a midpoint between the minimum and maximum test points.

Mass Flow Rate (mdot)

The SRHX water mass flow rates were set at 90.7 kg/hr, 181.4 kg/hr, and 362.8 kg/hr for the steady state characterization tests. This range was based on of previous TDA testing (Nabity, 2008) and related to representative spacecraft mission designs (Mills-Alford, 2008; NASA, 2005). The 90.7 kg/hr parameter is chosen based on prior TDA test results, where the previously constructed hardware was capable of rejecting the desired heat load (Nabity, 2008). The second test point, 181.4 kg/hr is double that of the first. This value is close to what is specified for the Crew Exploration Vehicle (CEV), 203.5 kg/hr (NASA, 2005). The last point, 362.8 kg/hr is double that of the CEV or four times that of the initial test point, and is close to that of the space shuttle mass flow rate of 430.92 kg/hr (Mills-Alford, 2008). The preliminary steady state tests were conducted at 40 kg/hr.

Test Output Definitions

Outlet Temperature (Tout)

The outlet temperature is representative of the heat that was transferred out of the working fluid relative to the inlet temperature. By evaluating this change in temperature, the net heat rejected from the SRHX was determined. The predicted outlet temperatures were calculated using the three heat models discussed in Chapter III. The predictions were compared to one another to show the variable range in results from the different methods. The predictions were compared to the physical test results and the differences were analyzed. The difference between the

actual and predicted results could potentially be used for an efficiency, or weighting factor in future models. Large differences between the actual and predicted results were used to indicate that another model entirely is needed to represent the outlet temperature.

Change in Pressure

Delta pressure across the working fluid inlet and outlet is correlated to flow area reduction within the heat exchanger due to ice formation. The maximum pressure difference will be used to size the pump required onboard the ATCS. The predicted pressure differences were calculated using models discussed in Chapter III. The predictions were compared to the physical test results and the differences were analyzed. The difference between the actual and predicted results could potentially be used for an efficiency, or weighting factor in future studies. Large differences between the actual and predicted results were used to indicate that another model is needed to represent the pressure change.

Results and Uncertainties

In this section, the variables involved in the steady state testing predictions are discussed. The uncertainties present in the values will be discussed, along with the methodology of determining the uncertainty. The variables are identified with corresponding values and uncertainties in APPENDIX C. The calculated values for the convective heat transfer coefficient and exposed surface area will be discussed in detail, since they are the primary drivers of the steady state test predictions.

Variable Definitions and Uncertainties

The three methodologies for predicting the outlet temperature and change in pressure were described in Chapter III. The equations were solved given the variables for the test apparatus.

A table of the variables and the associated errors are shown in APPENDIX C. The table also lists the units used for calculation, and how the value is determined. The value is listed if it is known or controlled. If the value is calculated, the number is not displayed, since there are 27 values that it will achieve through the tests. The uncertainty is displayed in the final column. The uncertainty has a set value if the uncertainty of the test equipment is known, or if the parameter changes relative to environmental conditions. The calculated variables have uncertainty percentages, based upon an analytical uncertainty model.

$$Uncertainty = 2sqrt\left(\frac{meas_1}{uncertainty_1}^2 + \cdots + \frac{meas_n}{uncertainty_n}^2 \right) \quad (75)$$

The uncertainty equation calculates the sum of squares for each value, based on the magnitude of the value, and the uncertainty of the value. The summation of each squared value is determined, at which point the square root is taken of the result. The final result is then multiplied by 2, since the uncertainty is an absolute value, and can become either positive or negative when implemented in further equations.

In simple calculations where the absolute uncertainties are known (such as the heat transferred from the working fluid, Q_{wf}) the magnitude of the measurement relative to the uncertainties is fairly low. However, when the Q_{wf} term is used in calculating for another term, the uncertainty quickly increases, especially due to the 2 coefficient before the square root term. As the uncertainty propagates through equations, the uncertainty percentage quickly escalates to high values. This can be most clearly seen with the surface area, convective heat transfer, outlet temperature, and pressure difference calculations

Convective Heat Transfer Coefficient and Surface Area Exposed

Equation 41 describes the method of computing the convective heat transfer coefficient of the fins using the Rayleigh number. By utilizing the Rayleigh number estimation (Equations 43-44), three convective heat transfer coefficients were found for the fins. The convective heat transfer of the fins was combined with the convective heat transfer of the shell (Equation 53) to compute a single term for the convective heat transfer (Equation 55). There were only three estimates, as opposed to the 27 one might expect, since the estimation is only a function of mass flow rate, and neglects the inlet and wall temperature. The values for the convective heat transfer coefficients via Rayleigh number estimation are listed below:

Table 7: Convective Heat Transfer Coefficient Calculation Using Rayleigh Number Estimation

	m_{dot1}	m_{dot2}	m_{dot3}
h (W/m^2K)	75629	108910	150248

In Table 7, as well as all following tables, m_{dot1} corresponds to 90.7 kg/hr, m_{dot2} corresponds to 181.4 kg/hr, and m_{dot3} corresponds to 362.8 kg/hr. The results shown in Table 7 are much higher than typical range of values for water of 500-10,000 W/m^{2}K (Coulson, 1996) Since values in Table 7 are unrealistically high, and did not take the inlet and wall temperature into account, another method was used to find unique convective heat transfer coefficients for each set of the 27 input parameters. The second method utilized a higher order Rayleigh number estimation (Equations 47-53). Each calculation took the mass flow rate, the inlet temperature, and the wall temperature into account. The values for the convective heat transfer coefficients via higher order Rayleigh number are listed below:

Table 8: Convective Heat Transfer Coefficient Calculation at T_{wall}=-20°C Using Higher Order Rayleigh Number Estimation

h (W/m^{2}K)	Ti_1	Ti_2	Ti_3
m_{dot1}	40527	40338	40154
m_{dot2}	42019	41824	41633
m_{dot3}	43377	43176	42979

Table 9: Heat Transfer Coefficient Calculation at T_{wall}=-40°C Using Higher Order Rayleigh Number Estimation

h (W/m^{2}K)	Ti_1	Ti_2	Ti_3
m_{dot1}	45784	45573	45366
m_{dot2}	46865	46650	46438
m_{dot3}	47881	47661	47445

Table 10: Heat Transfer Coefficient Calculation at T_{wall}=-80ºC Using Higher Order Rayleigh Number Estimation

h (W/m^{2}K)	Ti_1	Ti_2	Ti_3
m_{dot1}	52971	52730	52494
m_{dot2}	53695	53451	53212
m_{dot3}	54391	54145	53903

In Tables 8-10, as well as all following tables, T_1 corresponds to 15 ºC, T_2 corresponds to 20 ºC, and T_3 corresponds to 25 ºC. These convective heat transfer coefficient results are high for a water based technology, and are within the bounds of water's typical range of 500-10,000 W/m^{2}K (Coulson, 1996). The high values indicate that the equations predicted an idealized performance for water based testing. This is likely due to the high conductivity of the metal within the heat exchanger. The idealized assumptions can further be seen with the high Prandtl number (7.02), which indicates a strong conductive transfer, and is on the upper end of the typical Prandtl numbers for water of 5.5-7 (Grossman and Lohse, 2002). Also, the Prandtl number calculation did not take ice formation's affect on the SRHX's conductivity into account. In reality, with more ice within the SRHX, the convective heat transfer coefficient will likely decrease, since less surface area is exposed to the working fluid.

By using Equation 40, the surface area can be calculated for each convective heat transfer coefficient. The surface area exposed from Table 7 convective heat transfer coefficients is listed below.

Table 11: Exposed Surface Area Calculation Using Values in Table 7

	h_1	h_2	h_3
As (m^2)	1.39 E-6	9.67 E-7	7.01 E-7

Again, there are only three terms calculated for the surface area estimation, since it is only a function of the three heat transfer coefficients. All area estimates are unrealistically small, due to the large convective heat transfer coefficients in Table 7. The 27 predictions of the surface area exposed from Table 8-10 convective heat transfer coefficients are listed below.

Table 12: Exposed Surface Area Calculation at T_{wall}=-20ºC Using Table 8

'As' (m^2)	T_{i1}	T_{i2}	T_{i3}
m_{dot1}	0.002613	0.002626	0.002637
m_{dot2}	0.005041	0.005065	0.005088
m_{dot3}	0.009767	0.009813	0.009858

Table 13: Exposed Surface Area Calculation at T_{wall}=-40ºC Using Table 9

'As' (m^2)	T_{i1}	T_{i2}	T_{i3}
m_{dot1}	0.002313	0.002324	0.002335
m_{dot2}	0.004520	0.004541	0.004561
m_{dot3}	0.008848	0.008889	0.008930

Table 14: Exposed Surface Area Calculation at T_{wall}=-80ºC Using Table 10

'As' (m^2)	T_{i1}	T_{i2}	T_{i3}
m_{dot1}	0.001999	0.002009	0.002018
m_{dot2}	0.003945	0.003963	0.003981
m_{dot3}	0.007789	0.007826	0.007860

The results show a large change in surface area with increasing mass flow rate, a lesser change with decreasing wall temperature, and a minor change in surface area with increasing inlet temperature. This is expected, because the

magnitude of change in the temperatures is small when considering the change in absolute temperature (Kelvin). For instance, T_{i2} increases by a factor of 1.0174 from the T_{i1} value, since the absolute temperature only increases from 288 to 293 ^{o}K, compared to the factor of 2 increase from m_{dot1} to m_{dot2}.

When conducting the surface area calculations, a check is performed to ensure that the surface area results were within the hardware parameters of the SRHX. In other words, the surface area should never be greater than 0.0538 m^2, since this is the maximum surface area that can be exposed within the SRHX (Nabity, 2012). The lower surface area should never be lower than the surface area within the insulated channel, 0.0088 m^2. If the surface area calculations are outside these bounds, the surface area calculation is highlighted with red text in Tables 12-14.

There are many points that are outside the bounds of the maximum surface area of the SRHX. The surface areas that fall below the 0.0088 m^2 limit are generally associated with low mass flow rates, high wall temperatures, and low inlet temperatures. Previous testing indicates that similar test conditions generally lead to less ice within the SRHX, and a higher surface area exposed, which agrees with the predicted trending. Therefore, while many of the areas are unreasonably small, the overall trends shown in Tables 11-14 conform with previous testing with the SRHX.

Since the surface area calculations agree with the general trending of the SRHX tests, the outputs were used to scale the areas so that they fit within the required SRHX surface area limits. The predated surface area outputs were scaled to the hardware limits assuming that the maximum calculated surface area (0.009858 m^2, from Table 11, T_{i3}, m_{dot3}) was actually the fully exposed surface area in the physical SRHX hardware (0.0538 m^2). This methodology seemed to be the best compromise to maintain the integrity of the equation outputs, while still keeping the areas within hardware limits. The formula used to estimate the scaled surface area is shown in Equation 75.

$$A_{s_{estimate}} = A_{s_{calculated}} * \frac{0.0538}{A_{s_{calculated_{maximum}}}} \tag{75}$$

The scaled surface area predictions were applied to the values within Tables 12-14 and are shown in Tables 15-17.

Table 15: Exposed Surface Area Estimation at T_{wall}=-20°C

'As' (m^2)	T_{i1}	T_{i2}	T_{i3}
m_{dot1}	0.01426	0.01433	0.01439
m_{dot2}	0.02751	0.02764	0.02777
m_{dot3}	0.05331	0.05355	0.05380

Table 16: Exposed Surface Area Estimation at T_{wall}=-40°C

'As' (m^2)	T_{i1}	T_{i2}	T_{i3}
m_{dot1}	0.01263	0.01268	0.01274
m_{dot2}	0.02467	0.02478	0.02490
m_{dot3}	0.04829	0.04852	0.04874

Table 17: Exposed Surface Area Estimation at T_{wall}=-80°C

'As' (m^2)	T_{i1}	T_{i2}	T_{i3}
m_{dot1}	0.01091	0.01096	0.01101
m_{dot2}	0.02153	0.02163	0.02173
m_{dot3}	0.04251	0.04271	0.04290

By utilizing Equation 75, all 27 test points in Tables 12-14 were scaled down by the same amount, and the exposed surface area within the heat exchanger never exceeds 0.0538 m^2 or is lower than 0.0088 m^2. These results maintain the trends shown in Tables 11-14, which match up adequately with the trends predicted by the computational fluid dynamics model run by TDA. With the lowest mass flow rate, inlet temperature, and wall temperature, the area exposed within the SRHX is at a minimum. Conversely, the maximum mass flow rate, inlet temperature, and wall temperature show the largest surface area exposed. This indicates that the scaled surface area predictions are a reasonable estimate for the surface area exposed within the SRHX. While it would have been ideal to find a more suitable equation that did not force the scaling factor to be used, a direct equation to determine the exposed surface area was not encountered in the research.

Steady State Test Predictions

The steady state test outputs were predicted for the SRHX tests as per Aim 3. The predictions for the steady state test results were calculated using the methodologies described in Chapter III. The temperature outlet (T_o) predictions and the rationale for the difference between the results are the focus of discussion, since the change in temperature is the primary means of assessing the heat rejection

capability of the SRHX. The pressure difference predictions are presented, rationalized, and compared along with the test results. A variable sensitivity analysis was conducted with the predictions to demonstrate the relative weighting of the uncertain terms used within the calculations.

Working Fluid Test Predictions

The first methodology used to predict the SRHX outputs involved using the working fluid Equation 27. The working fluid equation required assuming an incoming heat load to calculate the outlet temperature of the SRHX. For the 15 ºC inlet temperature, the spacecraft was assumed to experience the predicted heat loads in eclipse (1190.1 W). The second inlet temperature, 20 ºC, was assumed to be the temperature the heat exchanger would experience in the sunlit portion of the orbit, but with no albedo heat loads (2133.5 W). The final water inlet temperature, 25 ºC, was assumed to be experienced when the spacecraft was in its maximum heat load condition (2463.7 W) with direct Sun and full albedo heat loads. For each condition, the mass flow rates and inlet temperatures were specified, leaving the outlet temperature as the only unknown. The results of the working fluid methodology are listed below in Tables 18-20.

Table 18: Working Fluid Estimates for Outlet Temperature and Pressure Change at T_{wall}=-20°C

	T_{i1}	T_{i2}	T_{i3}
m_{dot1}	148.8 Pa	148.8 Pa	148.8 Pa
	3.8 C	-0.1 C	1.7 C
m_{dot2}	605.7 Pa	605.7 Pa	605.7 Pa
	9.4 C	9.9 C	13.4 C
m_{dot3}	0.7 Pa	0.3 Pa	0.0 Pa
	12.2 C	14.9 C	19.2 C

Table 19: Working Fluid Estimates for Outlet Temperature and Pressure Change at T_{wall}=-40°C

	T_{i1}	T_{i2}	T_{i3}
m_{dot1}	148.0 Pa	148.0 Pa	148.1 Pa
	3.8 C	-0.1 C	1.7 C
m_{dot2}	604.7 Pa	604.7 Pa	604.8 Pa
	9.4 C	9.9 C	13.4 C
m_{dot3}	10.1 Pa	9.5 Pa	9.0 Pa
	12.2 C	14.9 C	19.2 C

Table 20: Working Fluid Estimates for Outlet Temperature and Pressure Change at T_{wall}=-80°C

	T_{i1}	T_{i2}	T_{i3}
m_{dot1}	146.7 Pa	146.8 Pa	146.8 Pa
	3.8 C	-0.1 C	1.7 C
m_{dot2}	603.1 Pa	603.1 Pa	603.2 Pa
	9.4 C	9.9 C	13.4 C
m_{dot3}	32.0 Pa	30.9 Pa	29.9 Pa
	12.2 C	14.9 C	19.2 C

In Tables 18-20, and all following tables, the orange cells represent pressure difference predictions, and the blue cells represent the outlet temperature predictions. The outlet temperature values do not vary based on the wall temperature, since the wall temperature is not involved in the working fluid model. The outlet temperature trends conform to previous test data where the change in

temperature decreases with a higher mass flow rate, and increases with higher heat loads.

The only temperature that seems unusual is the T_{i2} and m_{dot2} test point, where the outlet temperature is predicted to be -0.1 ºC. This is physically improbable since the water cannot exit in its liquid state at a lower temperature than freezing. In reality, the outlet temperature should be limited to 0 ºC. The negative value is listed since the change in temperature required to maintain thermal equilibrium at the given heat load (2133.5 Watts) and mass flow rate is greater than 20 degrees. This result indicates that for the given inlet temperature and mass flow rate, the SRHX would not be able to provide the required 2133.5 W heat rejection.

The working fluid equations have the greatest uncertainty in outlet temperature prediction due to the fact that a heat load was assumed for each of the test conditions, rather than using the hardware inputs. This model is useful since the hardware could be tested to determine what input parameters allow for thermal equilibrium at the given heat loads. However, this method only shows what outputs are required to allow the hardware to meet specific heat loads, rather than using the test inputs to model the outputs. This is especially evident with the non-changing estimations between each wall temperature.

Though the wall temperature did not affect the output temperature, the change in wall temperature did cause a change in pressure for the working fluid

equations. The change in pressure was calculated by using the predicted surface areas presented in Tables 15-17 and the associated mass flow rate.

The pressure changes were compared to previous SRHX test results. The highest change in pressure came from the T_{i3} and m_{dot2} test point in the T_{wall2} test condition, where the pressure was calculated to be 603.2 Pa, which is only 0.08745 PSI. Previous testing. This is far below the minimum value recorded for the previous testing, where the results of the smaller SRHX tests showed pressure differences from 0.9 PSI at 90.7 kg/hr to 5.9 psi at 907 kg/hr (Nabity, 2008). This indicates that the pressure difference estimations are likely not an accurate representation of the actual SRHX performance.

The pressure differences shown for the working fluid model will be the same as the other three methods of calculation. This occurs because the exposed area was assumed to be the same for each of the three models. Each model follows the same pressure difference calculations given the mass flow rate and exposed surface area. Since the surface area and mass flow rate are the same for each model, the pressure differences are the same as well. Since all pressure difference outputs are the same for the four sets of estimates, the pressure difference will not be discussed further in this section.

Thermodynamic Test Predictions

The second methodology for predicting the SRHX output involves using the thermodynamic Equations 38-61. With the thermodynamic equations, the

convective heat transfer coefficient is used to determine the amount of heat that can be absorbed from the fluid passing by a heat exchanger fin. The equations take all test variables into account in calculating the change in pressure and outlet temperature readings. Therefore, this methodology is a more robust means of calculating the predicted test outputs compared to the working fluid equations, where a heat load had to be assumed, and the SRHX wall temperature was ignored. The results from the thermodynamic equations are listed below in Tables 21-23.

Table 21: Thermodynamic Estimates for Outlet Temperature and Pressure Change at T_{wall}=-20°C

	T_{i1}	T_{i2}	T_{i3}
m_{dot1}	148.8 Pa	148.8 Pa	148.8 Pa
	5.0 C	9.8 C	14.5 C
m_{dot2}	605.7 Pa	605.7 Pa	605.7 Pa
	8.1 C	12.9 C	17.6 C
m_{dot3}	0.7 Pa	0.3 Pa	0.0 Pa
	13.4 C	18.3 C	23.1 C

Table 22: Thermodynamic Estimates for Outlet Temperature and Pressure Change at T_{wall}=-40°C

	T_{i1}	T_{i2}	T_{i3}
m_{dot1}	148.0 Pa	148.0 Pa	148.1 Pa
	5.7 C	10.5 C	15.2 C
m_{dot2}	604.7 Pa	604.7 Pa	604.8 Pa
	7.9 C	12.7 C	17.5 C
m_{dot3}	10.1 Pa	9.5 Pa	9.0 Pa
	12.0 C	16.8 C	21.6 C

Table 23: Thermodynamic Estimates for Outlet Temperature and Pressure Change at T_{wall}=-80°C

	T_{i1}	T_{i2}	T_{i3}
m_{dot1}	146.7 Pa	146.8 Pa	146.8 Pa
	6.4 C	11.2 C	16.0 C
m_{dot2}	603.1 Pa	603.1 Pa	603.2 Pa
	7.8 C	12.6 C	17.4 C
m_{dot3}	32.0 Pa	30.9 Pa	29.9 Pa
	10.5 C	15.3 C	20.1 C

With the thermodynamic equations, the outlet temperature predictions do not vary to the extent shown in Tables 18-20. This is especially evident when looking at the small change in outlet temperatures with decreasing wall temperatures. This indicates that wall temperature is not a very large driver of temperature change when using the thermodynamic equations.

The outlet temperature is predicted to increase with increasing mass flow rate when using the thermodynamic equations. However, the magnitude of mass flow rate increase is greater than the magnitude of change in temperature decrease. This indicates that a higher mass flow rate provides more heat rejection than lower mass flow rates, even though the outlet temperature is increased. This is the expected trend, since the water is allotted less contact time with the heat exchanger between the inlet and outlet.

The outlet temperature increases with increasing inlet temperatures. However, the inlet temperatures increase by a larger amount than the increase in outlet temperatures. Therefore, the overall change in temperature (and heat rejected), increases with increasing inlet temperatures. The change in temperature

does not appear to alter significantly from the T_{in2} to T_{in3} test points compared to T_{in1} to T_{in2} for all mass flow rates and wall temperatures. This indicates that the increase in temperature is linearly related to the increase in the amount of heat rejected.

The decreasing wall temperature acts to decrease the outlet temperature for the same mass flow rates and inlet temperatures. This is expected, since a colder wall means the temperature gradient is larger along the SRHX, and more heat can be absorbed. The change in outlet temperatures is not as linear as that seen with increasing inlet temperatures. This is likely due to the reduced temperature gradient as a function of the surface area exposed, as shown in Equation 75.

The thermodynamic equations and methodology predicts unique outputs for each of the 27 test points. This is a more robust solution than that obtained from the working fluid equations, since the thermodynamic equations predict the performance, rather than testing towards a given solution. However, there are some large uncertainties within the thermodynamic calculations, which will be discussed in the variable sensitivity section.

Predictions Based on Previous SRHX Testing

The final means of predicting the test outputs was through using SRHX equations developed from previous SRHX modeling and testing (Equations 64 and 67). The SRHX equations were formulated based on physical testing of a smaller SRHX, with different material properties. However, the hardware is similar enough

so that the predictions for the smaller SRHX are assumed to lead to a reasonable estimate for the outputs of the larger SRHX being tested.

There are two equations used to predict the SRHX overall heat transfer coefficient. The first is based on numerical modeling (Equation 64). The second is based off of previous testing trends (Equation 67). The numerical heat transfer coefficient (Equation 64) is presented first, and the test-based heat transfer coefficient follows in the next set of tables. The output predictions from using Equation 64 are shown in Tables 24-26.

Table 24: Numerical Overall Heat Transfer Coefficient Estimates for Outlet Temperature and Pressure Change at T_{wall1}=-20°C

	T_{i1}	T_{i2}	T_{i3}
m_{dot1}	148.8 Pa	148.8 Pa	148.8 Pa
	14.0 C	18.7 C	23.3 C
m_{dot2}	605.7 Pa	605.7 Pa	605.7 Pa
	12.9 C	17.1 C	21.2 C
m_{dot3}	0.7 Pa	0.3 Pa	0.0 Pa
	10.4 C	13.9 C	17.1 C

Table 25: Numerical Overall Heat Transfer Coefficient Estimates for Outlet Temperature and Pressure Change at T_{wall2}=-40°C

	T_{i1}	T_{i2}	T_{i3}
m_{dot1}	148.0 Pa	148.0 Pa	148.1 Pa
	12.9 C	17.5 C	21.9 C
m_{dot2}	604.7 Pa	604.7 Pa	604.8 Pa
	10.4 C	14.4 C	18.3 C
m_{dot3}	10.1 Pa	9.5 Pa	9.0 Pa
	5.3 C	8.3 C	11.1 C

Table 26: Numerical Overall Heat Transfer Coefficient Estimates for Outlet Temperature and Pressure Change at T_{wall3}=-80°C

	T_{i1}	T_{i2}	T_{i3}
m_{dot1}	146.7 Pa	146.8 Pa	146.8 Pa
	9.9 C	14.2 C	18.5 C
m_{dot2}	603.1 Pa	603.1 Pa	603.2 Pa
	3.6 C	7.2 C	10.6 C
m_{dot3}	32.0 Pa	30.9 Pa	29.9 Pa
	-8.3 C	-6.1 C	-3.9 C

The set of data obtained for the hottest wall temperature (T_{wall1}) shows a wide range of outlet temperature predictions. The outlet temperatures generally increase with increasing inlet temperatures, but the overall changes in temperature increase since the inlet temperatures increase by a larger amount than the increase in outlet temperatures from T_{i1} to T_{i2} and T_{i2} to T_{i3}. This means that the higher inlet temperatures lead to a greater amount of heat rejection from the working fluid.

The increasing mass flow rate causes a decrease to the outlet temperatures, and an increase to the heat rejected. This is the opposite trending seen from the thermodynamic and working fluid based predictions. The decreasing outlet temperature is an unexpected trend, since the water is allotted less contact time with the heat exchanger between the inlet and outlet with higher mass flow rates. The trend is explained by the increase in surface area exposed within the heat exchanger for higher mass flow rates, which allows more conductive rejection of heat from the working fluid.

The decreasing wall temperature causes the outlet temperatures to decrease, as expected. The decreasing wall temperature appears to affect the low mass flow rates most significantly. This can be seen from the decrease in output temperature predictions for m_{dot1} from T_{wall1} to T_{wall3}. This model indicates that for low mass flow rates, the change in wall temperature greatly affects the outlet temperature.

The predictions for some of the outlet temperatures show negative values. This indicates that the analysis predicts an outlet temperature of less than freezing for the set of input parameters. In other words, the equation predicts that additional water will freeze within the SRHX for the given conditions. The negative outlet temperature is improbable for actual results, but with the uncertainties within the equation, the prediction is within the bounds of a realistic output.

Table 24-26 show the output predictions from the numerically-based overall heat transfer coefficient prediction, Equation 67. The final set of output predictions in Tables 27-29 is based off previous test results, shown in Equation 67.

Table 27: Test-Based Overall Heat Transfer Coefficient Estimates for Outlet Temperature and Pressure Change at T_{wall1}=-20°C

	T_{i1}	T_{i2}	T_{i3}
m_{dot1}	148.8 Pa	148.8 Pa	148.8 Pa
	7.0 C	10.5 C	13.9 C
m_{dot2}	605.7 Pa	605.7 Pa	605.7 Pa
	5.7 C	8.9 C	18.9 C
m_{dot3}	0.7 Pa	0.3 Pa	0.0 Pa
	4.2 C	7.2 C	10.1 C

Table 28: Test-Based Overall Heat Transfer Coefficient Estimates for Outlet Temperature and Pressure Change at T_{wall2}=-40°C

	T_{i1}	T_{i2}	T_{i3}
m_{dot1}	148.0 Pa	148.0 Pa	148.1 Pa
	4.9 C	6.1 C	9.5 C
m_{dot2}	604.7 Pa	604.7 Pa	604.8 Pa
	0.4 C	3.6 C	6.7 C
m_{dot3}	10.1 Pa	9.5 Pa	9.0 Pa
	-2.2 C	0.8 C	3.6 C

Table 29: Test-Based Overall Heat Transfer Coefficient Estimates for Outlet Temperature and Pressure Change at T_{wall3}=-80°C

	T_{i1}	T_{i2}	T_{i3}
m_{dot1}	146.7 Pa	146.8 Pa	146.8 Pa
	-6.2 C	-2.8 C	0.8 C
m_{dot2}	603.1 Pa	603.1 Pa	603.2 Pa
	-10.3 C	-7.1 C	-4.0 C
m_{dot3}	32.0 Pa	30.9 Pa	29.9 Pa
	-14.9 C	-12.0 C	-9.2 C

The outlet temperatures increase with increasing inlet temperatures. As with Tables 21-26, the increase in outlet temperature is less than the increase in input temperature. Therefore, the overall change in temperature increases with respect to increases in inlet temperature, as does the amount of heat rejected from the working fluid.

The increase in mass flow rate causes a decrease in outlet temperature. This is the same trending as Tables 24-26, and is most likely due to the increased SRHX surface area exposed to the flow proportional to the increasing convective heat transfer coefficient.

The decreasing wall temperature generally causes the outlet temperatures to decrease for the same mass flow rate and inlet temperatures. This is the expected trend.

Some of the predictions for the outlet temperatures show negative values. This occurs with the coldest wall temperatures, coldest inlet temperature, and the highest mass flow rates. The negative values indicate that the analysis predicts an outlet temperature of less than freezing for the set of input parameters. This is improbable for actual results, but with the uncertainties within the equation, the prediction is within the bounds of a realistic output. The majority of the outlet temperatures are above the freezing point of water, which is a realistic expectation for the results. However, with the uncertainties within the equation, the predictions from Equation 64 cannot be said to be more accurate compared to any of the previous predictions.

Though both Equation 64 and Equation 67 use previous test data to predict the test outputs, there are notable differences between the outlet temperatures. The increases in outlet temperature with respect to inlet temperature are greater in Table 27-29 than that seen in Tables 24-26. Likewise, the decreases in outlet temperature with respect to mass flow rate are less in Table 27-29 than that seen in Tables 24-26. Both of these trends indicate that the change in temperature, and heat rejected is expected to be less with Equation 67 compared to Equation 64.

The set of data in Tables 27-29 shows a narrower range of outlet temperatures than that seen in Tables 24-26. Since all inputs to the two equations were the same, the difference lays in the coefficient and exponential term differences between Equations 64 and 67. In Equation 64, the coefficient is almost five times larger than the coefficient in Equation 67. On the other hand, the exponential term is almost four times as large for Equation 67 compared to Equation 64. Determining which term most affects the outlet temperature comes from looking at the differences in outputs between the two equations. Since the outlet temperatures decrease most significantly in Tables 24-26, it appears the coefficient for the overall heat transfer has a more dramatic effect on the change in temperature than the exponential term for the given set of inputs.

It is conceivable that the larger exponential term in Equation 67 could predict a greater amount of heat rejection with different test inputs. Given a larger surface area or LMTD, the term within the exponent would increase, causing an exponential increase in the outlet temperature calculations from Equation 67. Conversely, the increase in surface area or LMTD would be expected to cause an exponential decrease using Equation 64. Since the surface area was assumed to be the same for both models, only the LMTD would affect the outputs. For the given set of inputs, the LMTD was low enough so that Equation 67 predicted less heat transferred out of the working fluid for all test inputs.

Though Tables 21-26 provide reasonable trends, there is still a large amount of uncertainty in the outputs. One of the largest sources of uncertainty is from the

hardware used to develop the equations. The equations were developed for a different type of heat exchanger than the one being tested. While the equations may conform well to the hardware they were based upon, the validity of the equations does not necessarily transfer to the updated version of the hardware. Therefore, the equations used to model the smaller SRHX performance will likely not match up perfectly with the SRHX being tested. However, since the geometry and layout of the two heat exchangers are similar, it is reasonable to assume that the equations would give similar results between the two pieces of hardware.

Overall Temperature Comparison

The four calculations used to calculate the outlet temperature can be compared to one another by looking at the temperature range of each output side-by-side. Figure 25 displays the temperature range for each wall temperature, calculated through the four equations.

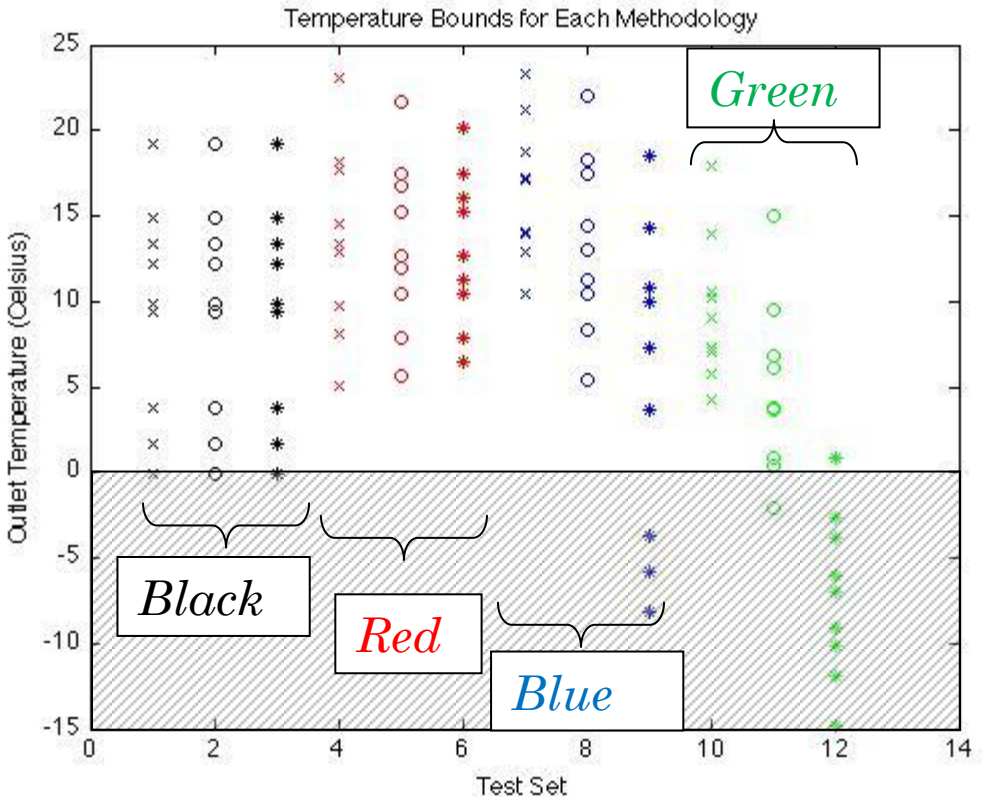

Figure 25: Range of Predicted Outlet Temperatures from Tables 18-29

For each set of data, the leftmost bar ('x') contains the estimates for T_{wall1}, the rightmost bar ('*') is the set of estimates for T_{wall3}, and the middle bar ('o') is the predictions for T_{wall2}. The black section etched out in the bottom portion of Figure 25, and the four following Figures, indicates the section where the water is predicted to exit at a temperature less than the freezing point of water. Predictions that fall within this range are due to the idealized assumptions, errors and uncertainties within the equations. The predictions in this area are unrealistic for physical test results, and indicate that more water would freeze inside the heat exchanger for the particular set of test inputs. The black bars represent the outlet temperature predictions obtained from the working fluid equations (Tables 18-20).

The working fluid equations only solved for a predicted heat input, and did not take wall temperature into account. For this reason, the three sets of wall temperatures all show the same temperature outputs. The range for the working fluid equations is ~20 ºC, indicating a large degree of performance variability in the predicted SRHX performance.

The red bars represent the outlet temperature predictions obtained from thermodynamic model (Tables 21-23). The variability of the outlet temperatures seems to increase slightly as the wall temperatures decrease. However, the average of the three groups does not appear to change very much as the wall temperature decreases. This indicates that the wall temperature affects the range of SRHX heat rejection, but not the average performance. The outlet temperatures show an output range of only ~17 ºC for the predicted test results, indicating the lowest degree of performance variability for the four results.

The blue bars represent the outlet temperature predictions obtained from the test-based overall heat transfer coefficient model (Equation 67; Tables 24-26). The variability of the outlet temperatures appears to increase as the wall temperature decreases, and the average outlet temperature shows a sharp decrease. This indicates that a lower wall temperature increases both the range of the SRHX heat rejection, and the overall performance. The outlet temperatures show a range of ~35 ºC, which is a relatively large range compared to the working fluid, and thermodynamic outputs.

The green bars represent the outlet temperature predictions obtained from the numerically-based heat transfer coefficient calculations (Equation 64; Tables 27-29). The variability of the outlet temperatures does not show much of a change as the wall temperature decreases, though the average outlet temperature decreases significantly as the wall becomes colder. This indicates that a lower wall temperature increases the overall SRHX heat rejection, but does not increase the performance range. This test-based trend (green) generally agrees with the modified heat transfer coefficient calculation trends (blue). The differences show that the Equation 64 estimates a greater heat rejection capacity at lower wall temperatures, while Equation 67 predicts a larger heat rejection range for similar conditions. The outlet temperatures from Equation 64 show a range of ~36 ºC, which is the highest range of all calculation methods, though for a given wall temperature, the range of heat rejection capabilities are not as large as the modified predictions.

Variable Sensitivity Analysis

A sensitivity analysis is a means of determining the contribution of an individual input to the model's output. By varying a single input parameter, the change in output can be related to that isolated input variable. The sensitivity analysis will only focus on the outlet temperature, since that is the best indication of the SRHX heat rejection performance.

Many of the variables within the outlet temperature calculations have a large degree of uncertainty, most notably the exposed surface area, and the convective

heat transfer coefficient. Since the two terms are linearly related to one another, a sensitivity analysis was conducted by modifying the surface area, which equates to an equivalent change in the convective heat transfer coefficient.

A sensitivity analysis was also conducted on each of the three test input parameters: the mass flow rate, the inlet temperature, and the wall temperature. The input sensitivity analysis isolated one of the input parameters and doubled the value, while keeping all other input terms the same. The exposed area was recalculated and modified, as per Equation 75, and the output temperatures were re-calculated and plotted.

By analyzing which of the modified terms created a greater impact on the outlet temperature calculation, it was possible to determine which variable creates the largest change in outlet temperature. The first sensitivity analysis was conducted by halving the estimated surface area (half that shown in Tables 15-17) for each set of test points. The reduction in surface area is expected to increase the outlet temperature, since less conduction occurs with a smaller area. Figure 26 shows the temperature trends of the four methodologies when the exposed surface area is halved.

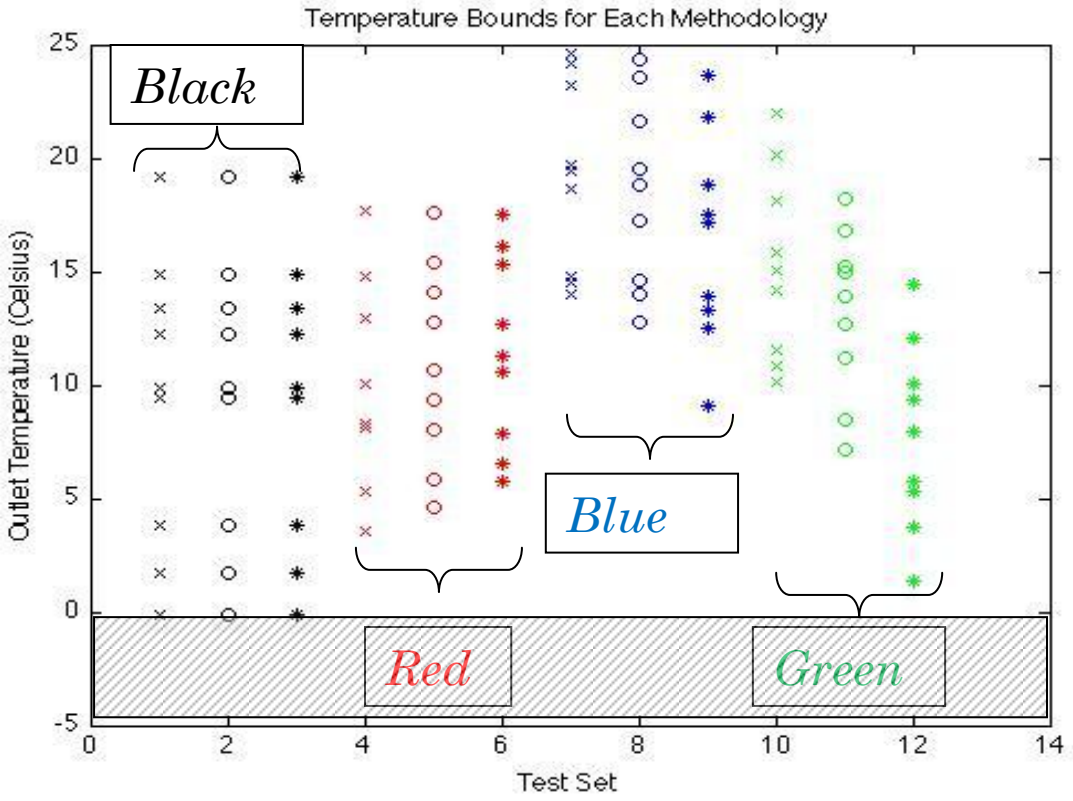

Figure 26: Range of Predicted Outlet Temperatures with One Half the Surface Area in Figure 25

When the exposed area is halved, all outlet temperatures increase aside from the working fluid temperatures. The working fluid temperatures remain the same since the calculations are not a function of the surface area exposed. All of the other three temperature prediction methodologies show higher outlet temperatures, and a lower range of values for the range of input parameters.

The second sensitivity analysis is conducted by doubling the mass flow rate. The increase is expected to decrease the outlet temperature as well, since the trends from Tables 21-29 show decreasing outlet temperature with increasing mass flow

rates. Figure 27 shows the temperature trends of the four methodologies when the mass flow rate is doubled.

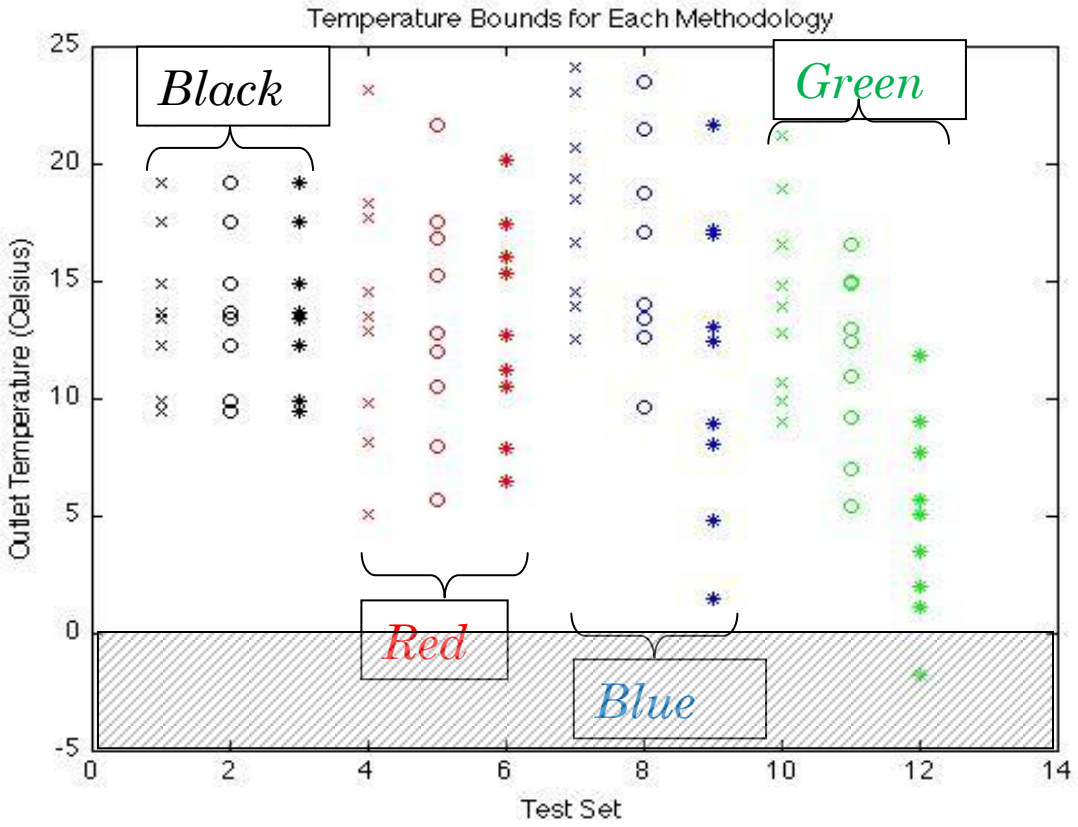

Figure 27: Range of Predicted Outlet Temperatures with Two Times the Mass Flow Rate (0.05038-0.201558 kg/sec) in Figure 25

When the mass flow rate term is doubled, the outlet temperatures show an increase for all temperature trends compared to Figure 26. This trend was expected for the working fluid predictions (black) increase on average, because the predicted heat loads are the same between Figure 27 and Figure 25, and with a higher mass flow rate, a lower change in temperature is required. The increase in outlet temperature was not expected for any of the other three methodologies, since Tables 21-29 show the outlet temperature decrease with increasing mass flow rate.

Another strange trend was the reduction in temperature output range for the three trends. This trend is most likely due to the re-calculation of maximum surface area exposed within the SRHX. With the original maximum flow rate of 0.100779 kg/sec, the maximum surface area was predicted to be 0.009858 m^2. With the increased maximum flow rate of 0.201558 kg/sec, the maximum surface area was predicted to be 0.01955 m^2, almost twice that of the original calculation, With the use of Equation 75, the predicted areas were scaled down twice as much as they were from the values used in Figure 56. Since m_{dot1} and m_{dot2} in this sensitivity analysis are equal to the m_{dot2} and m_{dot3} values used in Figure 56, the scaling causes a significant reduction in the surface area exposed for the same inputs, which reduces the amount of heat transferred from the working fluid. This likely accounts for the reduction in temperature output range for the thermodynamic and overall heat transfer calculation equations.

Overall, it appears that increasing mass flow rates cause a reduction in the range of outlet temperatures. However, since the heat rejected from the working fluid is proportional to the mass flow rate, the increase in temperature does not necessarily mean that less heat was rejected from the working fluid. If change in temperature difference between Figure 25 and 27 is greater than half, more heat is actually being rejected with a higher mass flow rate. The trend appears to be the case in Figure 27, meaning that larger mass flow rates reject more heat from the working fluid.

The next input analyzed for output sensitivity was the inlet temperature. It is expected that the increase of inlet temperature will cause an increase in outlet temperature, but a greater overall change in temperature, since the increased temperature allows for a greater degree of heat reduction from the working fluid. Figure 28 shows the outlet temperature changes when the inlet temperatures are doubled to 30, 40, and 50 °C.

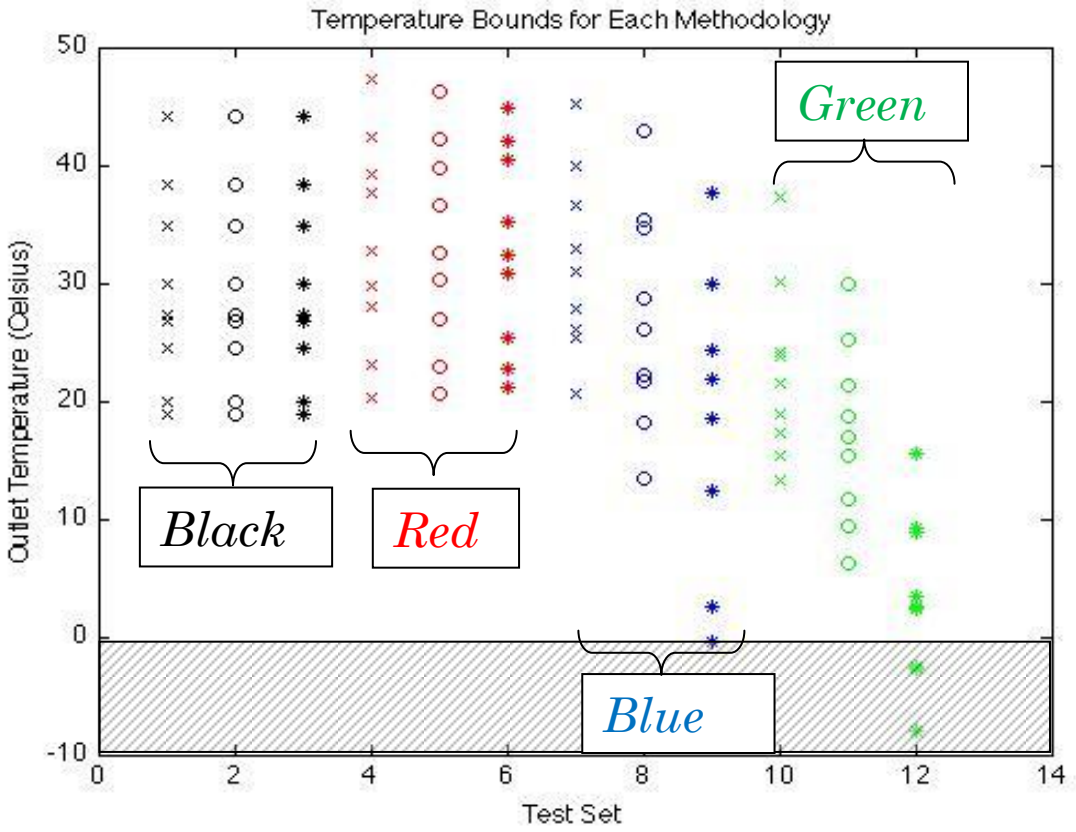

Figure 28: Range of Predicted Outlet Temperatures with Two Times the Temperature Input (30, 40, and 50 °C) in Figure 25

The overall temperatures increase for each of the four methodologies, as expected. The working fluid outlet temperature estimates show an increase of 15-25 °C. This is simply the change in temperature used for the sensitivity analysis,

meaning that the overall change in temperature did not change, because the estimated heat loads and mass flow rates are the same as Figure 25. The thermodynamic and overall heat transfer coefficient estimations for outlet temperatures increase on average (red, blue and green), though the range of outlet temperatures is significantly larger than that shown in Figure 25. This is especially evident with the tes-based overall heat transfer coefficient methodology, where the range increases from ~35 ºC to ~50 ºC. This is likely due to the overall range of the inlet temperatures increasing from 15 ºC used in Figure 25, to the range of 30 ºC used in the variable sensitivity analysis.

The overall heat transfer coefficient models (blue and green) both increase significantly in their output temperature range, though the blue line shows a greater increase in performance than the green line. This is because the blue line is based off the outputs from Equation 67, where the exponent is greater than that in Equation 64. Since the increase in inlet temperature increased the LMTD term, the exponential term had a greater impact in the outlet temperature prediction. For both models, there are still some points that drop below 0 ºC, indicating that even with double inlet temperatures, the models predict a non-probable amount of heat rejected from the water.

Overall, the increase of inlet temperatures causes a greater change in temperature, and a greater amount of heat rejected overall. Unlike the mass flow rate variability, the exposed surface area prediction was not changed very much by the increase in inlet temperature compared to Figure 25. This is expected, because

the surface area calculation is much more affected by mass flow rate than the change in inlet temperature.

The final variable sensitivity analysis was conducted by varying the wall temperature of the SRHX. A colder wall temperature was expected to decrease the outlet temperature predictions, since the temperature gradient is increased with a greater temperature difference from the working fluid to the edge of the SRHX wall. Figure 29 shows the outlet temperature changes when the wall temperatures are decreased to -40, -80, and -160 ºC.

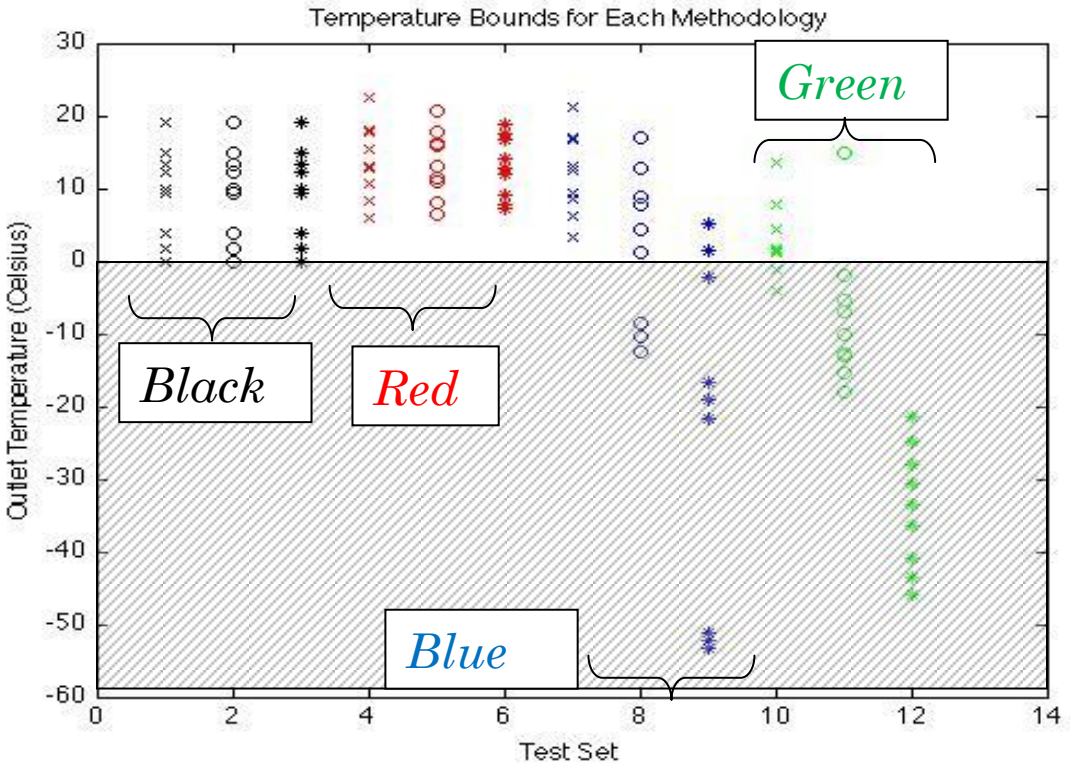

Figure 29: Range of Predicted Outlet Temperatures with Two Times the Wall Temperature (-40, -80, and -160 ºC) in Figure 25

The decrease in wall temperature causes a decrease in all outlet temperatures, aside from the working fluid predictions. This is because the working

fluid equation does not take the wall temperature into account when computing the outlet temperature. The thermodynamic equations (red) show a slight increase in the overall range of outlet temperature predictions compared to Figure 25, and the average temperature decreases slightly on average. The effect of the changing wall temperature is especially evident when viewing the overall heat transfer coefficient predictions (blue and green). Both methodologies are fairly close to the Figure 25 trends for the -40 C wall temperature, but as the wall temperature decreases the average temperature quickly drops, and the range of temperature greatly increases. This is due to the LMTD term within the exponential of the overall heat transfer coefficient equations, which becomes increasing large with a greater difference between wall and inlet temperature. The -160 C temperature points are the only situation where the test-based overall heat transfer coefficient (blue) predictions are colder than the numerically-based (green) predictions. This is from the larger exponential term in Equation 67 compared to Equation 64. For all other inputs, the coefficient in Equation 67 leads to a lower outlet temperature, but in the case of large surface area or LMTD terms, Equation 67 actually predicts a greater temperature difference.

It is difficult to compare the four variables in determining which had the greatest effect on the outlet temperature prediction. While each variable was altered by a factor of two, the temperature changes were not as great of a factor as the change in area or mass flow rate, since the temperatures were doubled relative to their Celsius inputs, which is a fairly small change when considering the absolute

value of the change. Also, the area was recalculated and scaled for each of the separate inputs. While the overall range of estimated areas stayed the same for each input, some of the scales were significantly greater than others. This was most evident in the large scaling factor from the increase in mass flow rate.

Given the available data, the changes to the inlet and wall temperature seem to cause the greatest change to the predicted outlet temperatures. The wall temperature appears to affect the outlet temperature predictions the most. This is especially evident with the coldest wall temperature, where both the range and average temperature of the working fluid was dramatically altered from the trends shown in Figure 25. However, it is difficult to say that the inlet temperature would have caused more or less of an effect, since the range of sensitivity analysis was much greater with the wall temperature than the inlet temperature.

While the surface area exposed within the SRHX was the term with the greatest uncertainty in predicting the outlet temperatures, the surface area variability does not appear to affect the outlet temperature predictions as much as the three test inputs. Therefore, the term with the greatest uncertainty within the predictions is not the parameter which causes the greatest uncertainty in the answers. This is good for calculations and predictions, because the three inputs can be controlled very well with the test, while the surface area cannot.

Test Plan

Given the predictions for the SRHX performance, the next step was to actually test the hardware. The physical test of the SRHX hardware was conducted in Wheat Ridge, Colorado at the TDA laboratory with test points based off CU research. The following test plan was given to TDA to test the SRHX:

1. Chill the test bath to the T_{wall} temperature
2. Chill the water to the T_{in} temperature
3. Attach the water tubes to the inlet of the SRHX
4. Attach the outlet tubes to the outlet of the SRHX
5. Place the SRHX hardware within the test bath
6. Wait five minutes for the SRHX to chill to the test bath temperature
7. Set the mass flow rate
8. Allow the water to flow through the SRHX until the T_{out} and ΔP measurements are no longer changing in time
9. Record the T_{out} and ΔP measurements
10. Repeat steps 7-9 until all mass flow rate tests have been completed
11. Repeat steps 2-10 until all T_{in} tests have been completed
12. Repeat steps 1-11 until all T_{wall} tests have been completed

The physical layout of the SRHX test bed and the thesis author is shown below in Figure 30.

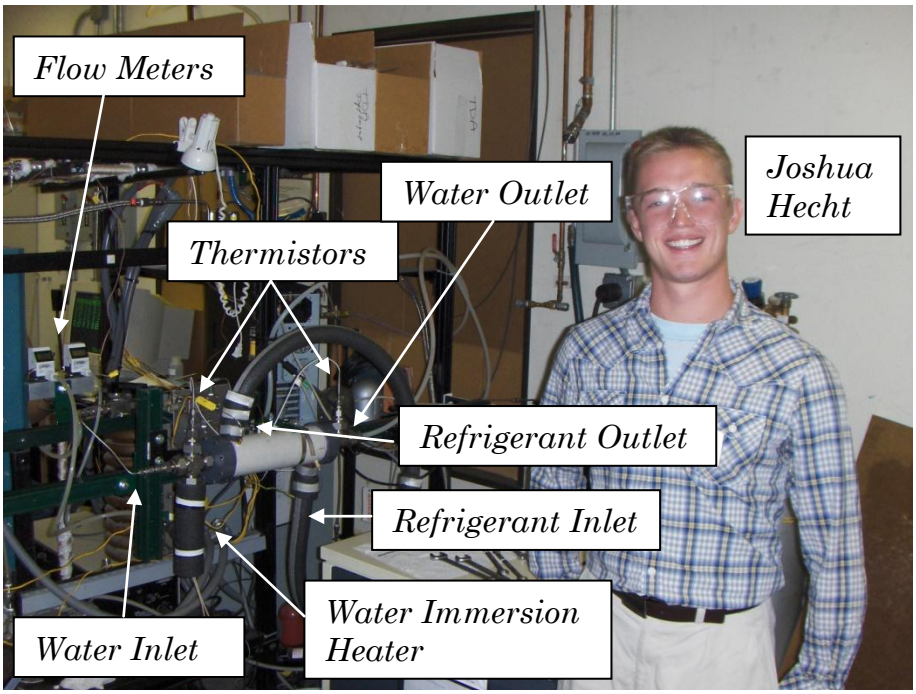

Figure 30: SRHX Test Bed and Author

The water is transferred to the water immersion heater through the water inlet to heat up the working fluid to the inlet temperature. The heated water goes into the SRHX within the PVC coolant shroud, which cools down the wall of the SRHX to the desired temperature. The wall is cooled down through a refrigerant that flows around the SRHX. The refrigerant enters the PVC coolant shroud from the refrigerant inlet, and is pumped out through the refrigerant outlet once it absorbs the heat from the SRHX. After the water flows through the SRHX, it is pumped out through the water outlet. The flow meters are used to measure the mass flow rate through the SRHX, and the thermistors are used to measure the inlet, outlet, and wall temperature of the SRHX test.

The SRHX hardware that was tested is shown in Figure 31.

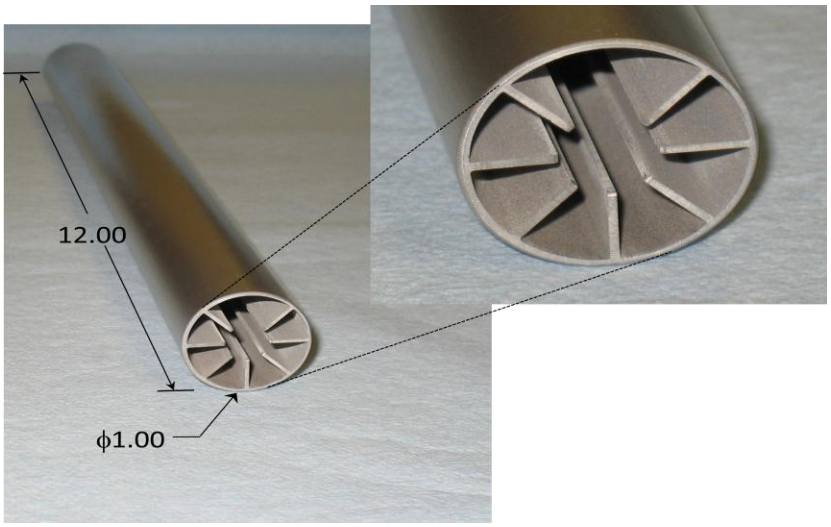

Figure 31: Full Layout and Zoomed in Cross-Section of the SRHX Test Apparatus

The SRHX shown in Figure 31 is constructed of Al6061-T6 aluminum. It was milled out of a single, solid rod, so that the connectivity between the fins and the outer shell would be maximized. The dimensions of the SRHX shown in Figure 31 are in inches. During the actual test, the top portion of the SRHX was insulated, and the middle portion allowed for the volumetric expansion of ice. This test apparatus was placed within the PVC coolant shroud shown in Figure 30 for testing.

Test Results

The fourth aim (Aim 4) of the thesis was to compare the predicted outputs of the SRHX against test results to assess feasibility. As of the time of this writing, the full steady state testing with the 27 test inputs discussed earlier has not been completed. However, a set of preliminary tests have been conducted with the SRHX

hardware to ready for the full set of steady state testing. The results of the preliminary testing are shown in Table 30.

Table 30: Test Outputs from Preliminary SRHX Testing

Test	mdot (kg/sec)	Tin (ºC)	Twall (ºC)	Tout (ºC)	ΔP (Pa)
1	0.0135	18.97	-4.5	14.38	275.6
2	0.0252	18.92	-4.6	14.43	275.6
3	0.0056	19.49	-16.6	18.34	Not Given
4	0.0036	20.30	-17.0	18.50	Not Given
5	0.0314	18.97	-4.5	14.38	Not Given
6	0.0253	18.92	-4.6	14.43	Not Given
7	0.0331	17.95	-2.9	14.47	Not Given
8	0.0228	18.42	-3.9	14.04	Not Given
9	0.0158	18.97	-12.3	14.28	Not Given
10	0.0328	18.01	2.5	13.98	Not Given
11	0.0244	18.50	1.9	14.37	Not Given
12	0.0191	19.63	1.5	13.39	Not Given

Table 30 lists the three independent variables (m_{dot}, T_{in}, T_{wall}), and the two measured dependent variables (T_{out}, ΔP). The change in pressure measurements were only collected for the first two tests, since the test apparatus was being modified at the time. While the inputs (independent variables) to the tests were not the same as those analyzed in Tables 18-29, the results can be used to compare the theoretical performance predictions to the hardware testing. By using the same

independent variables in modeling that were used during testing, one can obtain three predictions for the outputs by using the thermodynamic, and the two overall heat transfer coefficient equations to predict the SRHX outputs. The working fluid model was not compared to the physical test results, since the working fluid model does not take the three independent variables into account in estimating an outlet temperature.

The output temperatures for the hardware tests were compared to the theoretical output temperatures. The output temperature predictions were compared to the test results in two ways: by modifying the area as per Equation 75, and one that does not take the modified area into account. The predicted output temperatures with the Equation 75 modification are presented in Figure 32.

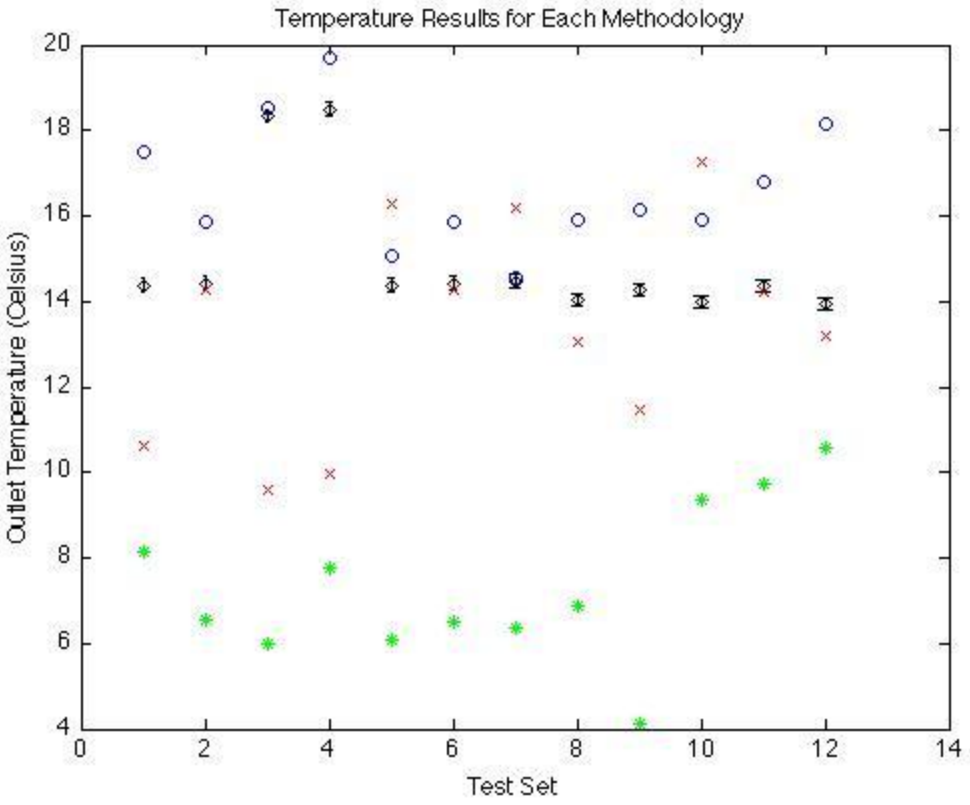

Figure 32: Outlet Temperature Test Results and Model Predictions with Modified Area

The physical test results listed in Table 30 are shown as black diamonds, with the associated .125 °C error bar. The results are compared to the thermodynamic (red), test-based (blue), and numerically-based (green) outlet temperature predictions. The results show the test-based estimates generally overestimate the outlet temperature by a few degrees, the thermodynamic predictions are distributed at varying intervals from the physical test results, and the numerically-based predictions noticeably underestimate the outlet temperature. This indicates that the numerical model over predicts the amount of heat rejected from the water, the test-based equations underestimate the amount of heat rejected from the water, and the thermodynamic estimates provide variable results. From

preliminary testing, the test-based modeling appears to be the best estimator of the physical performance of the SRHX. However, with the limited preliminary tests, it is difficult to determine whether the predictions and the associated trends would continue to be close to, or would fall away from the SRHX test results with the full set of test inputs.

To verify that the predictions agreed with the general trending of the test results, the Equation 75 modifier was removed for the same set of test inputs and predictions. The outlet temperature predictions when the area was not modified are displayed in Figure 33.

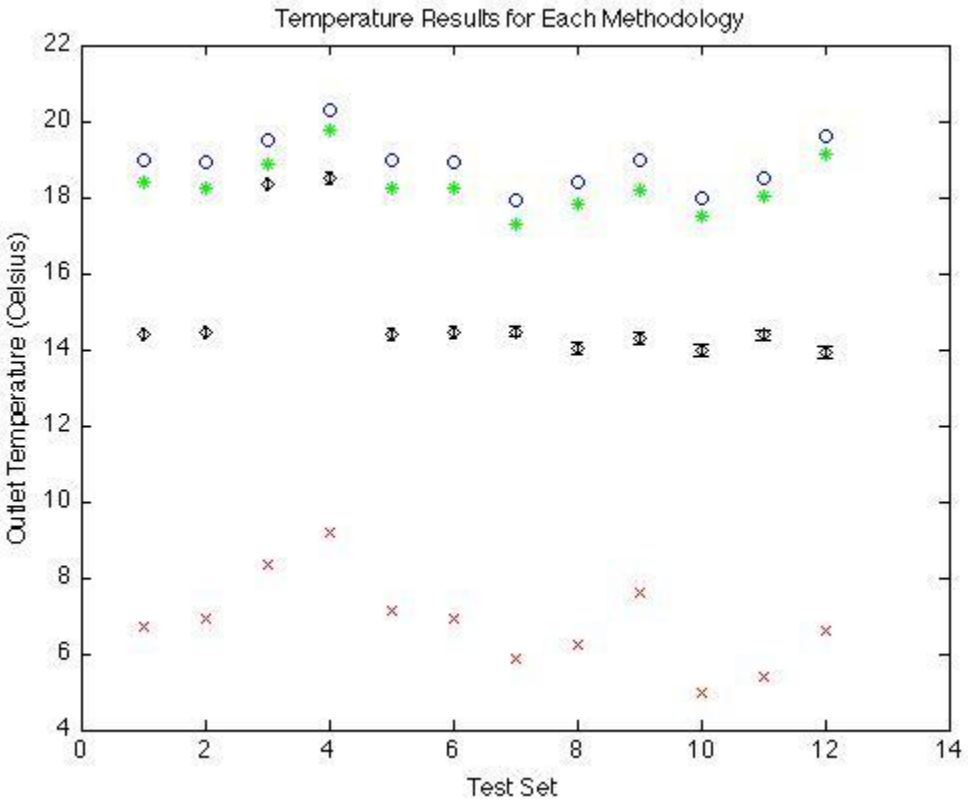

Figure 33: Outlet Temperature Test Results and Model Predictions with Non-Modified Area

In Figure 33, both the numerically-based and test-based predictions overestimate the outlet temperatures, while the thermodynamic predictions underestimate the outlet temperatures. By comparing Figure 32 and 33 one can see the effect of modifying the effective surface area, as per Equation 75. It appears that using the calculated area (excluding Equation 75, Figure 33) bounds the results to a range of ~10 C, whereas by using the modified area (using Equation 75, Figure 32), the outlet predictions conform better with the test results, albeit with increased uncertainty. Overall, Figure 33 demonstrates that each of the three prediction methodologies match up with the trends seen from the test results. This indicates that the equations used to estimate the SRHX performance are suitable to predict the trending on a first order analysis.

A pressure difference comparison was likewise conducted between the predicted change in pressure and the physical test results (where they were given) with the given set of test inputs. The results of the comparison are shown on Figure 34.

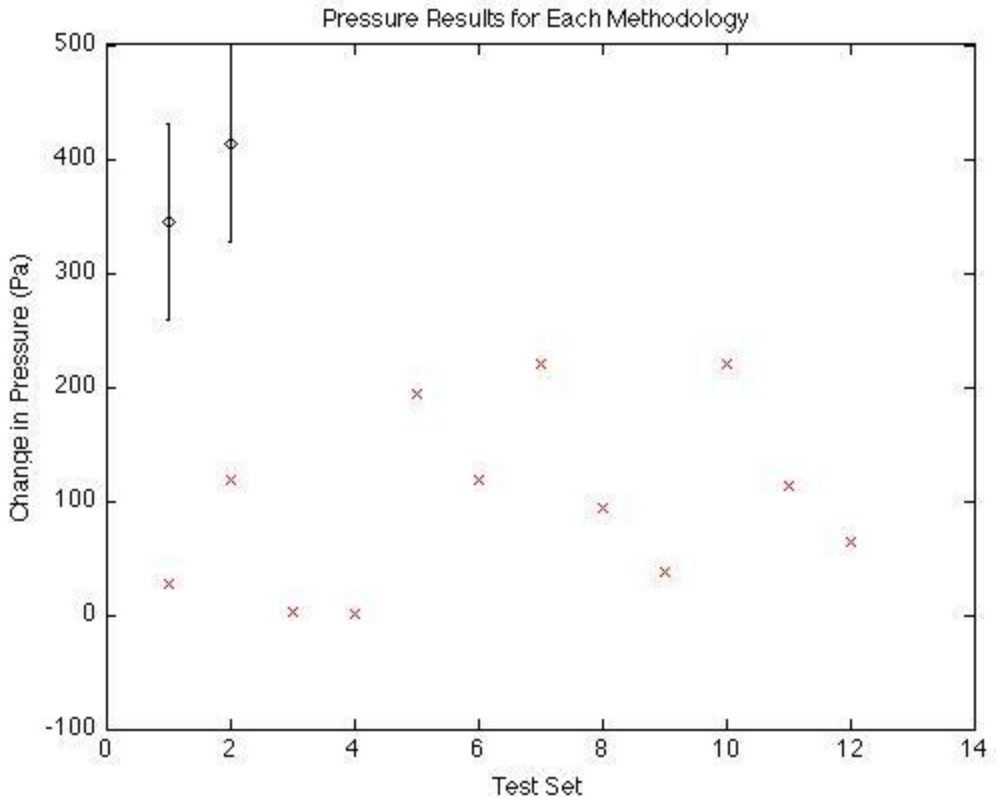

Figure 34: Outlet Change in Pressure Test Results and Model Predictions with Modified Area

The physical test results are shown as a black diamond with the associated instrument uncertainty, and the predicted pressure difference is shown as red markers. Equation 75 was used to modify the surface area in calculating the pressure difference. There is only one set of predictions shown, since the pressure difference prediction is the same for all three of the methodologies because the predicted surface area exposed and mass flow rate are the same for each of the three methodologies. The predictions underestimate the physical test results for the two given test outputs. This was expected, since the idealized flow assumptions generally led to minimal changes in pressure. While the results seem to be

relatively close to the predictions, and agree with the trending, it is difficult to tell the degree of accuracy the predictions provide with the limited amount of data.

The preliminary testing showed that the outlet temperature and pressure difference predictions are in general agreement with the physical hardware test results. The full set of test inputs will provide a greater range of results to compare the theoretical methods to the physical outputs. Once the full range of test data has been obtained, it is possible that an efficiency or weighting factor can be included to improve the equations used to predict the SRHX outputs.

Future Tests

The steady state results gave an indication of the SRHX heat rejection capability. The dynamic test involves evaluating how well the SRHX can regulate its heat rejection when the inlet temperature is changing, or when the mass flow rate is changing. The dynamic tests will better represent the expected inputs to the SRHX in a LEO spacecraft, where the heat loads will change based on the variable environments that the spacecraft encounters. While the dynamic tests are outside of the scope of the thesis, the predicted results have been modeled. For all models, the outlet temperature is assumed to be constant throughout the orbit.

The inlet temperature is expected to change linearly to the incoming heat load trends shown in Figure 6. The changing inlet temperature was calculated based on the assumption of a constant outlet temperature, a constant mass flow rate, and the orbital loads modeled previously.

For a constant mass flow rate and a changing inlet temperature, the temperature trends would look similar to that in Figure 35.

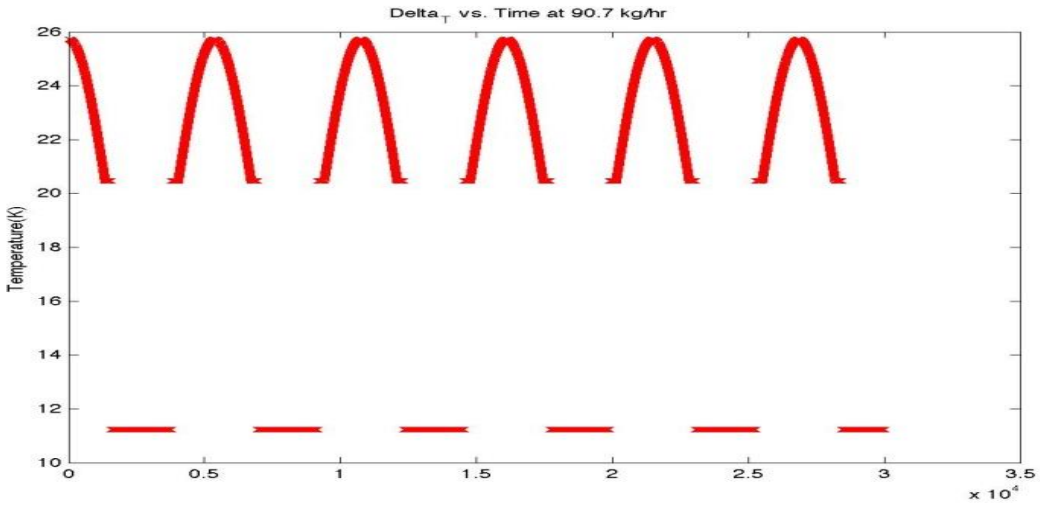

Figure 35: Change in Inlet Temperature Over Six Orbits for a Constant Mass Flow Rate (90.7 kg/hr)

The change in temperature is linearly proportional to the change in heat load shown in Figure 6. For such a condition, it would be expected that the ice would melt to expose more surface area within the SRHX to absorb the increased heat load.

Another means of dynamically testing the SRHX is through varying the mass flow rate. A mass flow rate change requires a bypass tube, which increases the complexity of the ATCS, but there is a possibility that an improved performance would be worth the increased complexity of the system. With a bypass tube, the inlet temperature of the water flowing into the SRHX could remain constant, even though the heat load into the spacecraft is dynamically changing.

With a constant inlet temperature, and changing mass flow rate, the mass flow rate trends would look similar to that shown in Figure 36.

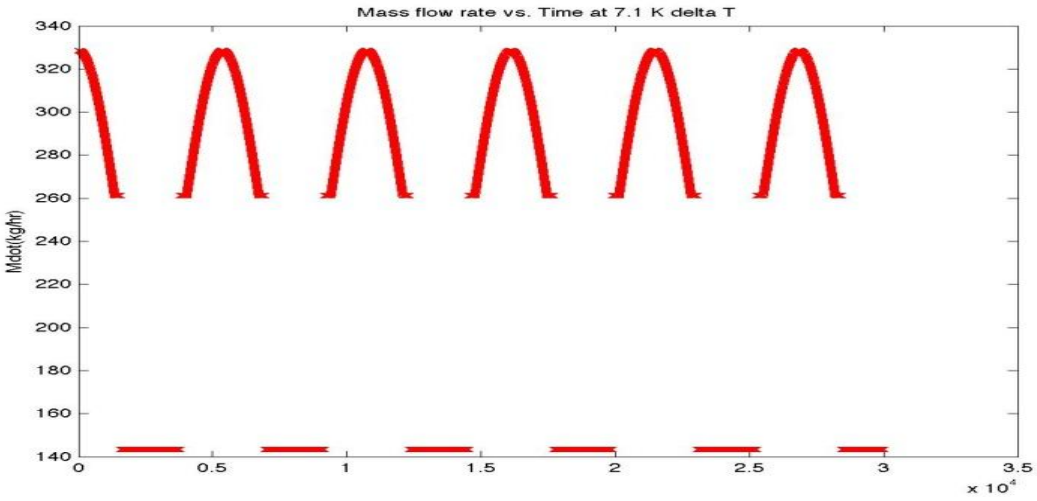

Figure 36: Change Mass Flow Rate Over Six Orbits for a Constant Temperature Change (7.1 °C)

Again, the change in mass is linearly proportional to the change in heat load shown in Figure 6. The ice presence within the SRHX would again be expected to decrease with the lower mass flow rate, since more heat is rejected from the spacecraft to maintain thermal equilibrium.

There is also a possible use of the SRHX where both the temperature and the mass flow rate changes, but this also requires a bypass tube. However, this option would enable the greatest degree of heat rejection variability from the SRHX. If both the mass flow rate and the inlet temperature changed simultaneously, the trends would look similar to that shown in Figure 37.

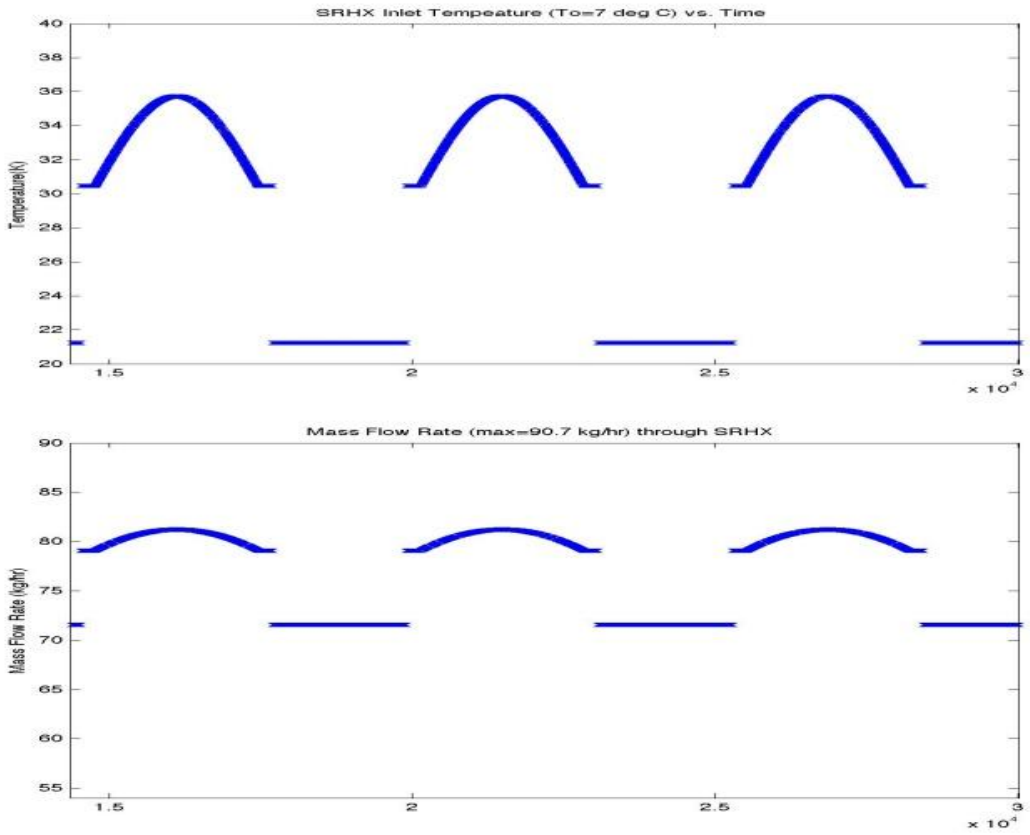

Figure 37: Change in Both Mass Flow Rate and Temperature Over Six Orbits

Both the mass flow rate and inlet temperature trends reflect heat load trends seen in Figure 6. However, neither the temperature nor the mass flow rate is as drastic as those shown in Figures 35 and 36, since both are acting to regulate the heat load simultaneously.

If these points were to be tested, the inlet temperatures or mass flow rates would mimic those of that shown in the Figures 35-37. Dynamic testing would be tested at the TDA laboratory in Wheat Ridge, Colorado, similar to the steady state tests. These tests would validate the dynamic heat regulation of the SRHX if the outlet temperature is maintained at a constant temperature throughout the

changing inlet conditions. This would indicate the use of the SRHX in a dynamic setting to maintain thermal equilibrium is a feasible means of using the technology.

Feasibility Analysis of the SRHX

The feasibility of the SRHX was based on whether the SRHX could use water as the working fluid, and whether the hardware could reject heat loads from the water as it passed through. The feasibility of using water of the working fluid is partially validated through the hardware functionality of the SRHX. The water was able to flow through during testing, indicating that ice formation did not block the water passage, and the expansion of water did not damage the SRHX. A full validation requires a full set of steady state and dynamic tests with the same criteria.

The second means of validation is assessed by determining the amount of heat the water was able to reject through the SRHX. This is primarily a function of the outlet temperature, since the change from inlet temperature indicates the heat rejected from the working fluid. The heat rejection capabilities ranged from 473 W to 605 W in the steady state configuration. The orbital model indicated heat rejection ranges from 1190.1 W to 2463.7 W were required to maintain thermal equilibrium. Since the SRHX heat rejection capabilities are less than the estimated range for the spacecraft orbital model, the hardware is not fully validated in its capability of rejecting the predicted heat loads. However, the steady state tests are

preliminary at this point, and the range will likely increase when the full set of input parameters are tested.

Effectiveness Analysis of the SRHX

The final aim (Aim 5) of the thesis is to evaluate the effectiveness of utilizing the SRHX within the spacecraft. The effectiveness of the SRHX is based on three factors. First, the system could be considered effective if the mass of the entire ATCS could be reduced. Secondly, the system could be considered effective if the complexity is reduced by the SRHX. Lastly, the system could be considered effective if the safety of the system is improved. The mass reduction, simplification, and additional safety of the ATCS are evaluated through a preliminary ESM.

Equivalent System Mass

A preliminary ESM is used to compare the masses, complexities, and safety of otherwise two identical systems with a single component substitution (Quinn, 2011). The component switch has a ripple effect, causing other changes to the overall system that can be characterized in the analysis. For instance, replacing a heavy pump with a lighter one might seem good initially, until the power is taken into account. If the lighter pump requires more power, then the battery or solar panels would have to increase in size and mass, thus increasing the radiator size, which ultimately can offset the initial mass savings benefit. A simplified ESM was conducted on each alternative architecture, as shown in Figures 11-18. The architectures provide the necessary assumptions to estimate the component size required to reject the heat loads.

The first ESM analysis involves the replacement of the entire water/ammonia ATCS system (Figure 9) with the SRHX. In the first alternative architecture schematic (Figure11) a bypass tube is included though, as mentioned in the 'Future Tests' section, the bypass tube would not be necessary if the mass flow rate were to remain constant throughout the orbit, and the SRHX could regulate the dynamic heat loads passively. In the first alternative architecture, the mass reduction comes from removing the water heat exchanger, removing the ammonia heat exchanger, and reducing the radiator size. The radiator size reduction can be determined by referring to the SRHX heat rejection modeling (Chapter III) and determining the maximum amount of heat that must be transported from the fins to the radiator during the dayside portion of the orbit.

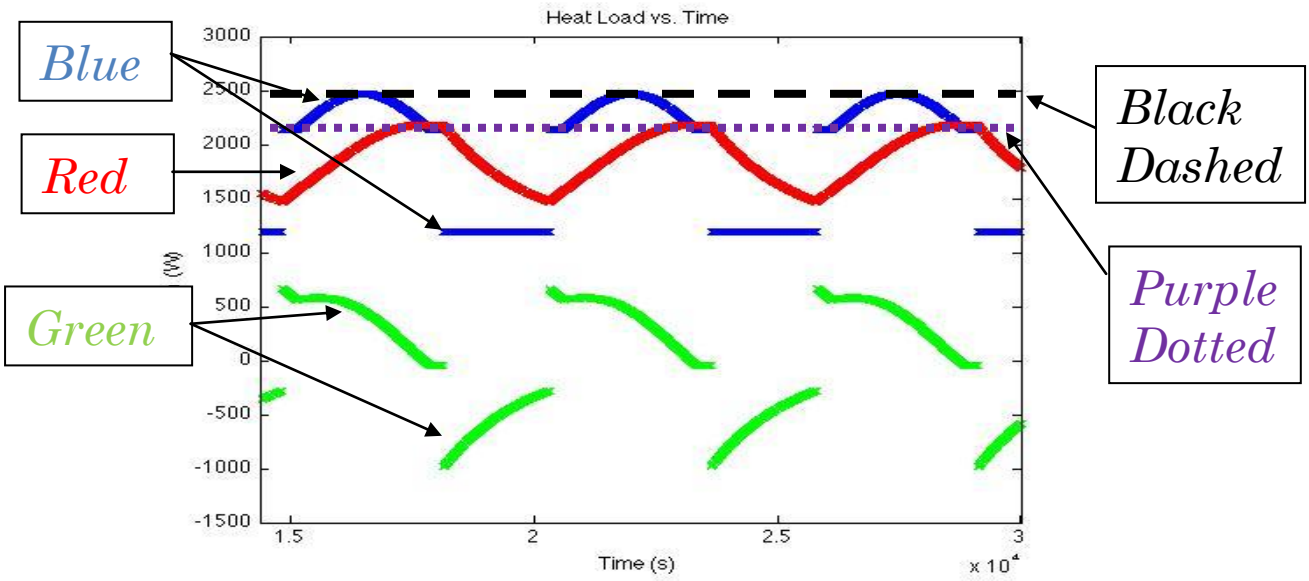

Figure 38: SRHX and PCM Heat Rejection Use in Reducing Radiator Size

In Figure 38, the black dashed line represents the required radiator heat rejection if no PCM (or other heat rejection device) is onboard the spacecraft. To

maintain thermal equilibrium at all points on orbit, the radiator has to be sized for the worst case heat load condition. In this example, the maximum heat load is 2464 W. If a PCM is included in the SRHX, the heat is rejected through the SRHX to the radiator, and the remaining heat is rejected through the melting of the PCM. As the ice melts, more SRHX area is exposed, allowing more heat to be rejected to the SRHX. Once the incoming heat load equals the SRHX heat rejection, steady state thermal equilibrium has been achieved.

The purple dashed line represents the required radiator heat rejection when a PCM is included onboard the spacecraft. The purple line goes through the intersection of the heat input and SRHX heat rejection, at 2154 Watts. This intersection is the maximum amount of heat that needs to be rejected from the SRHX to the radiator before the ice begins to freeze up again. Beyond that point, the incoming heat load is less than the SRHX heat rejection, and the radiator provides excess heat rejection.

A second ESM was conducted for alternative architecture 2 (Figure 14) where the SRHX replaces the entire water heat exchanger with the SRHX. In this configuration, the bypass valve is eliminated from the ammonia side, since the heat transfer is regulated on the SRHX side. The heat coming into the spacecraft can be buffered in the same fashion as in alternative architecture 1, with the PCM absorbing a portion of the heat load. The primary benefit to this architecture comes from less ammonia being needed in the ATCS, since the PCM absorbs a portion of the heat load. Therefore, the entire ammonia loop can be reduced in alternative

architecture 2. While the exact amount of mass reduction was not calculated, it was assumed that the size reduction of the ammonia loop was approximately half of the baseline loop mass.

The last alternative architecture (Figure 16) shows the water loop being augmented by the SRHX. In this configuration, the water and ammonia heat exchanger remain intact, along with the bypass tube. The addition of the PCM within the SRHX allows for a radiator size reduction. Unlike alternative architecture 1, the heat rejection to the radiator is not regulated by the presence of ice. Instead, the ice is used as a buffer for the maximum heat loads during the spacecraft orbit. A schematic of this use is shown below in Figure 39.

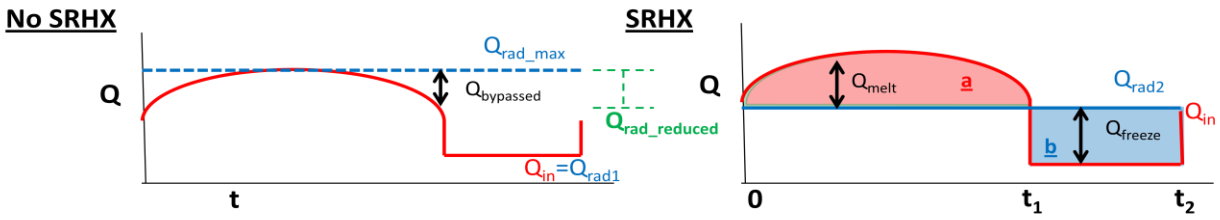

Figure 39: Maximum Radiator Reduction Through Utilizing a PCM

Both graphs show the same representative heat load over one orbit. As mentioned in alternative architecture one, in the baseline architecture (no SRHX) the radiator has to be sized for the maximum heat load. This is shown on the left graph with the blue dashed line. With the SRHX included, the radiator output can be decreased ($Q_{rad\_reduced}$), since the PCM absorbs a portion of the heat load. During the hot portions of the orbit, the excess heat load can be absorbed by the PCM, as shown by Q_{melt}. In the cold portions of the orbit, the excess radiator rejection can be used to freeze the ice, as shown by Q_{freeze}. The minimum radiator size can be

determined when the energy rejected from melting the ice (integral of Q_{melt}) equals the energy from freezing the ice (integral of Q_{freeze}). This occurs at the average of the heat load into the spacecraft, which in this case is 1977 W.

For each architecture, a first order mass estimate is predicted for each component within the ATCS. The radiator size is calculated from Equation 4, and the maximum estimated heat rejection for the given architecture. It is assumed that the radiator temperature is -40 ºC, and an emissivity of 0.88. To account for inefficiencies in the ATCS, the radiator size is increased from its regular value by 28% (James and Wiley, 1999). It is estimated that each square meter of radiator equals approximately 4kg of mass (James and Wiley, 1999). The masses for the heat exchanger loops shown in Figure 9 are predicted based on shuttle data (Sarraf, 2006). The bypass valve and associated valves are assumed to be one quarter of the associated heat exchanger.

The ESM methodology described above is a quantitative measure of reducing the mass of the spacecraft. The safety and complexity consequences of implementing the SRHX must be assessed qualitatively. The safety of the system can be enhanced by using water as the working fluid for the SRHX. As discussed earlier, one of the primary benefits of utilizing water as the working fluid is its safe, non-toxic properties should there be a leak in the cabin. While ammonia is not as toxic as Freon-21, there is still a level of danger in utilizing it within a human based spacecraft. Therefore, if less ammonia is present in the spacecraft, the safety will be improved.

The complexity of the architecture can be assessed by looking at the amount of components needed within the ATCS. An ATCS with two or more heat exchangers is considered more complex than those one with only one. The removal of the bypass valve also reduces the complexity, since the working fluid does not have to be actively diverted when in cold conditions. Lastly, the system can be considered less complex if the radiator size is reduced, since that will decrease the exterior size of the spacecraft.

The preliminary ESM used to compare the baseline architecture and the three alternative architectures is shown below.

Table 31: Preliminary Equivalent System Mass For the Baseline and Alternative Architectures

Characteristic	Baseline	Alt. Arch. 1	Alt. Arch. 2	Alt. Arch. 3
Required Radiator Size	18.79 m^2	16.14 m^2	16.14 m^2	13.44 m^2
Increased Radiator Size	24.05 m^2	20.66 m^2	20.66 m^2	17.20 m^2
Radiator	84.18 kg	72.31 kg	72.31 kg	60.21 kg
H2O HX	4 kg	0 kg	0 kg	4 kg
Ammonia HX	4 kg	0 kg	2 kg	4 kg
SRHX	0	3.62	3.26 kg	9.78 kg
Bypass Valve	1 kg	0 kg	.5 kg	1 kg
Pumps	2 kg	1 kg	2 kg	3 kg
Total Mass	95.18 kg	76.93 kg	80.07 kg	81.99 kg
Complexity	• Contains 2 loops • Contains bypass valve	• Contains 1 loop • No bypass valve required	• Contains 2 loops • No bypass valve required	• Contains 3 loops • Bypass valve required to SRHX
Safety	• Half Ammonia	• Water	• Decreased Ammonia	• Decreased Ammonia

In Table 31, the while cells show the required and increased radiator sizes. The orange cells contain the masses of each component, and the total mass. The green cells describe the qualitative complexity concerns. The blue cells contain the safety considerations.

Each of the architectures option has pros and cons to consider when implementing the architecture into the ATCS. In terms of mass, all of the alternative architectures provide a reduction in overall mass, primarily due to a reduction in radiator mass. Alternative architecture 3 provides the greatest reduction in radiator mass, even though no ATCS components were removed from the baseline architecture. However, alternative architecture 3 does not provide additional simplicity to the ATCS heat exchanger loops, since three heat exchangers are required to the overall architecture. In terms of simplicity, alternative architecture 1 is the least complex option, since only the SRHX loop is required to reject the incoming heat load. Alternative architecture 1 also benefits in that it is the safest option to implement onboard, since ammonia has been removed entirely from the ATCS system. It also provides the most overall mass savings. Alternative architecture 2 falls between the two options. It is simpler than alternative architecture 3, but provides less mass savings than alternative architecture 1. Alternative architecture 2 also contains ammonia, but less than the amount in alternative architecture 3, since the size of the loop is reduced. Overall, the SRHX can theoretically be implemented effectively within a spacecraft ATCS.

CHAPTER V

CONCLUSION

The objective of the thesis was to determine if the SRHX is a feasible and effective technology to implement onboard a spacecraft ATCS. This was partially validated through the experimental results and analysis. The validation came from the steady state performance of the SRHX, where the hardware was shown to be capable of utilizing water as the working fluid, and that heat could be rejected from the heat exchanger. A dynamic test with changing mass flow rates or inlet temperatures would have fully validated the performance of the SRHX in an orbital heat load simulation. The effectiveness of the SRHX was shown with a preliminary ESM analysis. Implementing the SRHX reduced the overall ATCS mass through radiator size reduction, and could provide attritional safety and simplification to the system if implemented in the correct architecture. The validation was a combined analysis through modeling the expected heat loads from an LEO spacecraft, investigating potential architectures, and providing the test points to characterize the SRHX.

Modeling Validity

Three Aims were created to set up the feasibility and effectiveness analysis: Aim 1 was to determine the LEO heat loads into a spacecraft, Aim 2 evaluated the possible means of implementing the SRHX into an ATCS architecture, and Aim 3 theoretically predicted the SRHX outputs. Each Aim was accomplished through modeling and was validated through heuristics or physical hardware testing.

The orbital loads were determined based on a one-meter radius, white painted, spherical spacecraft operating at a 350 km, 0 beta angle orbit. The orbit selection provided maximum time in eclipse, and a maximum heat load at orbit noon. These parameters set the extreme boundary for SRHX testing. The orbital models were constructed based on typical Keplerian equations, and using average values for the heat loads encountered on orbit. The results of the heat load modeling were validated through looking at previous orbital models and corresponding heat loads.

The next step was to evaluate the architecture trends expected from implementing the SRHX to a spacecraft ATCS. The SRHX was considered as a means of supporting or improving the baseline architecture ATCS. The baseline architecture was considered to be a two-loop system, containing ammonia and water separately, that transported heat through a counter flowing heat exchanger to the radiator. Three alternative configurations were considered feasible in implementing the SRHX to the baseline architecture. The first alternative architecture replaced the entire water/ammonia heat exchanger system, the second replaced only the water heat exchanger loop, and the third architecture utilized the SRHX to augment the water loop. Additional architectures were evaluated where the SRHX augmented the ammonia loop, but were determined to be non-feasible for a water based SRHX. Each configuration contained individual temperature and mass flow rate trends for each fluid passing through the loops. The trends were validated by

looking at previous mission data. The mass flow rates and temperature ranges were considered to be appropriate for a typical human rated spacecraft.

Lastly, the performance of the SRHX was modeled to estimate the outlet temperature and change in pressure for specified input parameters in hardware testing. Three inputs to the system were specified: the inlet water temperature, the mass flow rate of the water, and the wall temperature of the heat exchanger. Three test points were chosen for each input, leading to 27 tests overall. The test points were chosen based on required environmental control conditions of the cabin, and heuristics from previous missions.

The change in temperature was estimated through three methodologies: estimating the required heat rejection for a working fluid, utilizing thermodynamics equations, and through the utilization of previous SRHX findings. The results were similar, but there were notable differences between the separate methodologies. The three methodologies were used to bound the predicted range of outlet temperatures from the SRHX testing. The thermodynamic and test-based overall heat transfer coefficient methodologies were shown to be closest to the actual test results, though with the limited set of test data it is difficult to say how well the models predict the full range of SRHX performance. None of the methodology results matched up exactly with the expected test values. The difference between the predictions and the results could be used as an efficiency or weighting factor for future modeling. Overall, the results were close enough to the test results to validate the first-order estimates in predicting the SRHX heat rejection performance.

The change in pressure was determined through utilizing Bernoulli's equation with the expected change in flow area from the inlet to the outlet of the SRHX. The change in pressure results were the same for all three of the methodologies, since the exposed area was assumed for each test case. The change in pressure predictions was lower than the test results, though the set of test results were limited.

The pressure difference modeling will likely continue underestimate the actual test results, based on previous test results where the change in pressure is multiple PSI (Nabity, 2006). This indicates that the ice melt model used in pressure difference predictions is too simplistic for the geometry present within the SRHX. It is also possible that the use of Bernoulli's equation does not take enough turbulent and higher order fluid dynamics into account. Lastly, it is possible that the pressure sensors were located in non-ideal locations. As noted earlier, a similar area on the inlet and outlet side of the SRHX should provide a minimal pressure difference. However, the pressure sensor is outside of the inlet of the SRHX, and records a much lower Pin than a pressure sensor located just inside the inlet in high ice freeze conditions. Due to the discrepancy between the predicted and actual test results, the pressure difference calculations cannot be considered validated.

SRHX Testing

The fourth aim (Aim 4) of the thesis was to compare the SRHX predicted outputs against physical test results to assess feasibility. The preliminary steady state tests of the SRHX were conducted in October through November 2012. The

results were expected earlier than this time, so that the hardware outputs could be used to improve the SRHX models. However, due to time constraints the models could not be updated as per the original intention. If more time were allotted to the research, an equation might have been constructed, similar to that shown in Equations 64 and 67 where the test data was used to construct a heat exchanger coefficient prediction. This information could have provided coefficients for the conduction and convection equations, so that the thermodynamic equations would also predict reasonable results. However, the testing did fall close to the expected ranges of the outlet temperatures, indicating that the equations are a good first order estimate for the SRHX testing.

A full validation of the hardware use could have been accomplished if dynamic tests of the hardware could have been accomplished. The dynamic tests would have changed the inputs to the SRHX during the test to represent the changing heat loads a spacecraft might experience on orbit. The variable input conditions would have caused the PCM within the SRHX to freeze or melt while the test was being conducted, as opposed to being at a steady state. Since the self-regulating aspect of the SRHX comes from the ice presence within the heat exchanger, the rate of the ice formation and melt would have given an indication of the maximum rate of heat increase/decrease the SRHX could provide. This test will likely be conducted in the future, and the code within APPENDIX A gives the predicted inputs required for such a dynamic test.

A further test will be conducted with a SRHX containing carbon fiber fins and an aluminum shell. The carbon fiber fins have a thermal conductivity of 540 W/mK, which is significantly higher than the aluminum fins 167 W/mK. The higher conductivity indicates that the SRHX will be capable of absorbing more heat loads from the working fluid with the same exposed fin area. The test will demonstrate that the SRHX hardware performance can be varied as a function of the material selected for the SRHX structure.

The final aim (Aim 5) of the thesis was to evaluate the effectiveness of utilizing the SRHX within the spacecraft. The results from the SRHX testing were utilized in constructing a preliminary ESM and architecture comparison. The preliminary results indicate that the SRHX can theoretically add a benefit to the spacecraft in mass reduction, complexity reduction, and a reduction in ammonia onboard.

Discussion

The overall purpose of the thesis was

Determine if the self-regulating freezable heat exchanger is a *feasible* and *effective* technology to implement in a spacecraft active thermal control system.

The purpose was accomplished with the following Aims:

Aim 1. Determine the typical heat load of a human rated spacecraft in LEO

The thermal loads were established for typical LEO profiles with representative metabolic and avionic heat loads. The predicted thermal loads were used to determine the range of heat loads that the SRHX must reject.

Aim 2. Evaluate the possible means of implementing the SRHX into the spacecraft ATCS

The orbital heat loads were used to predict the theoretical temperatures and mass flow rates through the SRHX as the spacecraft propagates through its orbit. The hardware limitations were used to determine where the SRHX could be implemented within the ATCS architecture.

Aim 3. Theoretically predict the steady state outputs of the SRHX

The steady state prediction applied constant inputs to the SRHX model until a constant output was maintained. The inputs were chosen using the ATCS architecture predictions, the range of the predicted thermal loads, and the required cabin air temperature. The required heat load rejection, thermodynamic equilibrium, and previous testing data were used to predict four sets of SRHX outputs. The predictions were compared to one another to show the variable range in results from the different methods, along with the sensitivity of each input.

Aim 4. Compare the SRHX model against test results under theoretical scenarios to assess feasibility

The SRHX hardware was physically tested and the test outputs were compared to the predicted results. While the entire range of input parameters were not

analyzed, the preliminary analysis gave an indication that the SRHX was a feasible technology to reject heat from the spacecraft.

Aim 5. Evaluate the effectiveness of utilizing the SRHX within the spacecraft

The effectiveness of the SRHX was based on whether the SRHX provides a net benefit to the ATCS (and overall spacecraft) versus existing technology. The benefits were categorized into mass savings, simplifying the overall architecture, or by making the system safer and more reliable. A preliminary equivalent system mass was presented and compared the mass, complexity, and safety of each potential architecture for SRHX use. The study determined that the SRHX would provide sufficient benefit to outweigh the costs in implementation to a spacecraft ATCS

Overall, the feasibility and effectiveness were analyzed for the SRHX. The feasibility was partially validated, though more testing must be completed to fully ascertain that the technology is suitable for the full range of predicted heat loads. The preliminary ESM showed that there are numerous benefits to utilizing the SRHX within an ATCS system, but the overall costs and benefits of the technology cannot be fully understood until the hardware is tested under dynamic test inputs.

<u>Recommendations</u>

The primary recommendation is to fully validate the SRHX performance by conducting dynamic tests with the hardware. By simulating on orbit heat loads with variable inputs, the hardware can demonstrate its self-regulating capabilities. The

dynamic tests would also give an indication of how well the SRHX can utilize the PCM to buffer heat loads in hot environments. The dynamic tests would ultimately prove that the SRHX is a feasible and effective technology to implement onboard a human rated spacecraft.

Another test that could help characterize the SRHX usage would be to attach multiple SRHX together to dissipate the heat load. There are many ways to implement multiple SRHX in the ATCS. If the SRHX were utilized in parallel, each SRHX would have variable amounts of ice within the SRHX, which could be used to further regulate the heat rejection. If the SRHX were used in series, the additional PCM could be used to buffer a larger heat load from the spacecraft.

The range of the SRHX heat rejection capabilities could be determined through iteration of various beta angles on orbit. This analysis would help to determine the range of heat loads the technology might be expected to withstand. Higher beta angles would reduce the time in eclipse, giving less time for the cold conditions to allow the ice to freeze up. Also, the higher beta angles would lead to less albedo heat loading on the dayside portion of the orbit, which would reduce the maximum heat rejection the SRHX would be expected to absorb. From these findings, it would be possible to find an appropriate range of beta angles where the SRHX could be utilized.

The technology could be evaluated for use in a lunar or Martian based mission. For extra-vehicular activities on a planetary surface, the heat loads an astronaut experiences varies rapidly, depending on whether the astronaut is in the

Sun, or in the shade, and the heat rejection must be regulated accordingly. The PCM within the SRHX could be used to buffer and increase the heat loads in the sunlit portions of the surface. In the shaded regions, the heat load drops significantly and the water could again freeze, and store energy within its solid ice state (Nunneley, 1970).

The equations used to predict the test outputs should be re-evaluated. The convective heat transfer coefficient was not within the typical range for water, indicating that the methodology used in finding the term might be erroneous. The high value led to unreasonable answers for the surface area exposed within the SRHX. To work around this problem, the analysis was conducted with scaled values for the exposed surface area, rather than a computational solution. This assumption provided reasonable results, but it would have been better if the area could have been mathematically determined, rather than empirically. Also, the pressure differences predicted based on Bernoulli's equation proved to be lower than the test results. A higher order fluid model should be used to predict the ice formation, and the fluid dynamics within the SRHX, so as to improve the predictions.

The convective heat transfer coefficient was calculated as a function of the Rayleigh number. The Rayleigh number has a gravitational term within its calculation. In the absence of gravity, the Rayleigh number goes to zero. This would ultimately lead to a lower value for the convective heat transfer coefficient, meaning the water would be able to transport less heat loads for the same conditions as were tested on Earth. If the SRHX was used in a spacecraft, it would be necessary to re-

calculate the heat transfer coefficient, so that the gravitational term would be removed.

Overall, the analysis and testing provided a partial validation of the hardware for use in a human rated spacecraft. Further testing needs to be done to fully validate the hardware, but the steady state experiments provides a good first order estimate on the performance capabilities of the SRHX. The models used to create the test points and predict the SRHX output were mostly validated, if not altogether utilized. The updated heat transfer coefficient equations from the SRHX testing should be used to update expected SRHX performance models, which will improve the predicted SRHX outputs.

An abstract of this work has been submitted for consideration as part of the AIAA 2013 43rd International Conference on Environmental Systems (ICES). Pending acceptance and follow on effort, it is expected that these results will be presented at this forum in July 2013 and published as a peer-reviewed AIAA conference proceeding.

REFERENCES

Alvidres, H., D. Hoetger. *(1995), "Thermal Control."* Ed. M. Fisher.

Brown, C. D. (2002). *Elements of spacecraft design*. Aiaa.

Bulut, M., Sozbir, N., Gulgonul, S. (2008). *Thermal Control Design of TUSAT*. 6th. International Energy Conversion Engineering Conference (IECEC), Cleveland, OH.

Cengel, Y. A., (2003), *Heat and Mass Transfer: A Practical Approach, 3rd Edition,* Boston: McGraw Hill.

Churchill, S. W., Chu, H. H. (1975). *Correlating equations for laminar and turbulent free convection from a vertical plate*. International Journal of Heat and Mass Transfer, 18(11), 1323-1329.

Coulson, J. M. (1996). *Coulson & Richardson's Chemical Engineering: Fluid Flow*. Heat Transfer and Mass Transfer.

Curtis, H. (2009). *Orbital mechanics for engineering students*. Butterworth-Heinemann.

Grossmann, S., Lohse, D. (2002). *Prandtl and Rayleigh number dependence of the Reynolds number in turbulent thermal convection*. Physical Review E, 66(1), 016305.

Hanford, A.J. (2006), *Advanced Life Support Baseline Values and Assumptions Document.* Purdue University. ALS/NSCORT Specialized Center of Research and Training: Advanced Life Support.

Hanford, A.J., Ewert, M.K., (1996), *Advanced Active Thermal Control System Architecture Study*, NASA Technical Memorandum 104822.

Incropera, F., & DeWitt, D. (1985). *Introduction to heat transfer.*

James, R. W., Wiley, J. L. (1999). *Space mission analysis and design*. Kluwer Academic Publishers, London, USA.

Kakac, S., Pramuanjaroenkij, A., & Liu, H. (2012). *Heat exchangers: selection, rating, and thermal design*. CRC press.

Khaniki, H. B. (1994) "Thermal Design and Analysis of a Small Satellite." Applied Science and Research Association.

Kondepudi, D. (2008). *Introduction to modern thermodynamics*. Wiley.

La Placa, S. J., & Post, B. (1960). *Thermal expansion of ice*. Acta Crystallographica, 13(6), 503-505.

Leimkuhler, T. Stephan, R. Hawkins-Reynolds, E. (2010), *Testing and Failure Mechanisms of Ice Phase Change Material Heat Exchangers.*

Lide, D. R. (1990). *Handbook of chemistry and physics*, *1991*. CRC.

Lillibridge, S. Navarro, M. (2011) *Freezable Radiator Model Coorelation Improvements and Fluids Study*. NASA Johnson Space Center. Jacobs Engineering.

Metals Handbook, Vol.2 - Properties and Selection: Nonferrous Alloys and Special-Purpose Materials, ASM International 10th Ed. 1990.

Nabity, J.A., G.R. Mason, R.J. Copeland and L.A. Trevino, (2008), *A Freezable Heat Exchanger for Space Suit Radiator Systems*, SAE 2008-01-2111, 38th International Conference on Environmental Systems, July 2008. Republished as SAE Int. J. Aerospace April 2009 1:355-363.

NASA (2005), *NASA's Exploration Systems Architecture Study* Rep. no. NASA-TM-2005-214062.

NASA Preferred Reliability Practices (1995). "Spacecraft Thermal Control Coatings Design and Application."

Nunneley, S. A. (1970). Water cooled garments: a review. *Origins of Life and Evolution of Biospheres*, *2*(3), 335-360.

Qiu, X. L., Tong, P. (2001). *Onset of coherent oscillations in turbulent Rayleigh-Bénard convection*. Physical review letters, 87(9), 94501.

Quinn, G., Hodgson, E., and Stephan, R., (2011) *"Phase Change Material Trade Study: A Comparison between Wax and Water for Manned Spacecraft."* 41st International Conference on Environmental System

Sarraf, D.B. (2006) *Heat Pipe Heat Exchanger with Two Levels of Isolation for Environmental Control of Manned Spacecraft Crew Compartment*

Stephan, R. (2011), "Overview of NASA's Thermal Control System Development for

Exploration." 41st International Conference on Environmental systems. Portland, Oregon.

The Aluminum Association, Inc. from Aluminum Standards and Data 2000 and/or International Alloy Designations and Chemical Composition Limits for Wrought Aluminum and Wrought Aluminum Alloys (Revised 2001).

VanOutryve, C., (2008), *"A Thermal Analysis and Design Tool For Small Spacecraft."* Thesis to Mech/Aero Engineering at San Jose State University

Watson, J. T. R., Basu, R. S., Sengers, J. V. (1980). *An improved representative equation for the dynamic viscosity of water substance*. American Chemical Society and the American Institute of Physics.

Wieland, P. O. (2005). *Designing for human presence in space: an introduction to environmental control and life support systems (ECLSS).*

Williams, A. Palo, S. (2006), "Issues and Implications of the Thermal Control Systems on the "Six Day Spacecraft' ". 4th Responsive Space Conference. AIAA.

APPENDIX A:
CODE USED FOR ANALYSIS

Heat Load Calculations and SRHX Response

```
%Joshua Hecht
%July 2012
%Graduate Thesis Heat Exchanger Study


clear all
close all

%Define spacecraft size and internal heat
load for HEAT LOAD MODELING
sc_size=1;
internal_heat=1000;

r=6378.1+350; %For baseline case, assume 350
km, no beta
v=sqrt(398600/r); %Circular Orbit

time=[0:1:30000];
RO=[r 0 0];
VO=[0 0 v];
XO2=[RO VO];

tol=1e-12;
options=odeset('RelTol',tol,'AbsTol',[tol
tol tol tol tol tol]);

%ode45 matlab integrator - type "help ode45"

[t,X2]=ode45('two_body',time,XO2,options);

for j=1:length(X2)

posijk=[X2(j,1);X2(j,2);X2(j,3)];
velijk=[X2(j,4);X2(j,5);X2(j,6)];

[a(j),e(j),i(j),Omega(j),w(j),nu(j)] =
elorb(posijk,velijk);

r_orbit=posijk;

sc_volume=(4/3)*sc_size^3;

%theta=acos(posijk(1)/6628.1)*(180/pi);

transmitted_heat=1; %Assume no thermal lag
and instant heat transfer

a=0.22; %Assume white paint.

A_perp=pi*sc_size^2; %Assume spherical
surface area

ISun=1365; %Assume maximum intensity of Sun.
(1414 W/M2) CHANGED TO AVG

albedo=0.35; %Assume maximum. (0.52) CHANGED
TO AVG

Fs=posijk(1)/6628.1;

if Fs < 0
    Fs=0;
end

IEarth=275; %W/m^2 assume maximum

QSun=a*A_perp*ISun;

if posijk(3) < 6378.1
    if posijk(3) > -6378.1
        if posijk(1) < 0
            QSun=0;
        end
    end
end

transmittance=1; %This is what klaus was
talking about with the incident heat not
equaling absorbed heat

Qalbedo=albedo*Fs*QSun*transmittance;

QEarth=a*A_perp*IEarth*transmittance;

Qinternal=internal_heat;

Qin(j)=QSun+Qalbedo+QEarth+Qinternal;

end

plot(t,Qin(:),'bX'), title('Heat Load vs.
Time'), ylabel('Qin (W)'), xlabel('Time
(s)')
%print -djpeg heat_load_vs_time

%SRHX HW DEFINITION: DEFINE LENGTH OF SRHX
BASED ON GRAD T LIMIT

%Find the required length and ice
freeze/thaw rates for a given radius SRHX

% k=540; %W/m*K from Nabity's paper
% r=.0254/2; %Assume 1 inch. To meters
% l=.3048*2; %Assume 1 foot. To meters
%
% ice_density=916.7; %kg/m^3
%
% Hfus=334000; %J/kg
%
% for j=1:1000
%
%     l(j)=j*.005;
%
% grad_T=max(Qin(:))/(12*k*r*l(j)); %Will go
down with increasing l
%
% r_flow_min=min(Qin(:))/(12*k*grad_T*l(j));
%Set to some minimum value?
%
% %Ice melt/freeze calculations
% for i=1:length(Qin)
%
%     r_flow(1)=r_flow_min;
%     drdt(i)=(Qin(i)-
(12*k*grad_T*l(j)*r_flow(i)))/(ice_density*l
(j)*r_flow(i)*2*pi*Hfus);
%
% r_flow(i+1)=r_flow(i)+drdt(i);
%
% end
%
% if grad_T < 60 %Based off the 20 deg C to
-40 deg C fluid vs wall T in 2.7 kW test
case
```

```
%
% grad_T
% heat_pipe_length=l(j)*39.37
% break
%
% end
%
% end
% figure
%
plot((1:20:(20*length(r_flow))),r_flow(:).*3
9.37,'bX'), title('Flow Radius vs. Time'),
ylabel('Flow_radius(in)');
%
% figure
%
plot((1:20:(20*length(drdt))),drdt(:).*39.37
,'bX'), title('Change in Radius vs. Time'),
ylabel('Flow_radius change(in/sec)');

%Find the tempearture trends for the HX
architecture

% mass_flow=0.1197; %Use STS value
% cp=4204; %Water
% Tc=276; %Kelvin
% Tsrhx=273;
%
% for i = 1:length(Qin)
%     Th(i)=Tc+(Qin(i)/(mass_flow*cp));
%     mass_flow_srhx(i)=Qin(i)/(cp*(Th(i)-
Tsrhx));
% end
%
% figure
% plot((1:20:(20*length(Th))),(Th(:)),'bX'),
title('H2O Hot side Tempeature vs. Time'),
ylabel('Temperature(K)');
%
% figure
%
plot((1:20:(20*length(mass_flow_srhx))),mass
_flow_srhx(:),'bX'), title('Mass Flow
through SRHX'), ylabel('Mass Flow Rate
(kg/s)');
%
% %Find amount of ice necessary for
Qrad=Qavg w/ PCM buffer

% Qrad=avg(Qin(:))
% for 1 : length Qin(:) > Qrad
%     Qin-Qrad

%FIND THE GRAD T, DELTA T, AND M DOT W/
SPECIFIED HW LENGTH AND SIZE

k=540; %W/m*K from Nabity's paper
r_tube=.01181;%Assume 1 inch diameter. To
radius. with .035 in wall. To meters
r_fin=.007287; %From assuming 7 fins and
total SA=0.047 m2. This data is from when
l=10.5 in
r_between=.004523; %Space between fins
l=.3048; %Assume 12 inches. To meters

ice_density=916.7; %kg/m^3

Hfus=334000; %J/kg

grad_T=max(Qin(:))/(14*k*r_fin*l); %Will go
down with increasing l. Assume 7 fins

SA_min=min(Qin(:))/(k*grad_T);

r_fin_min=SA_min/(14*l)-r_fin; %Set to some
minimum value?

if r_fin_min < 0

    r_fin_min=0;
    r_in_set=SA_min/l;

    for i=1:length(Qin)

    r_in(1)=r_in_set;
    r_flow_in(1)=r_in(1)+r_between;
    r_out(1)=r_fin_min;
    r_flow_out(1)=r_between;

Qhx(i)=(14*k*grad_T*1*l*(r_in(i)+r_out(i))/2
);
    Qpcm(i)=1190.1-Qhx(i);
    dVdt(i)=Qpcm(i)/(ice_density*Hfus);
    r_in(i+1)=r_in(i)+dVdt(i)/(l*pi);

    if r_in(i+1) > r_fin
        r_in(i+1) = r_fin;
        r_out(i+1) =
r_out(i)+dVdt(i)/(l*pi);

r_flow_out(i+1)=r_out(i+1)+r_between;
        r_flow_in(i+1)=r_fin+r_between;
        if r_out(i+1) < 0
            r_out(i+1) =0;
            r_flow_out(i+1)=r_between;

r_flow_in(i+1)=r_in(i+1)+r_between;
        end
    else
        r_out(i+1)=r_out(i);
        r_flow_out(i+1)=r_between;
        r_flow_in(i+1)=r_in(i+1)+r_between;
    end


dP_dt(i)=(r_flow_in(i)^2)/(r_flow_out(i)^2);

end

end

% %Ice melt/freeze calculations
for i=1:length(Qin)

    r_fin_out(1)=r_fin_min;
    r_flow(1)=r_fin_min+r_between;

Qhx(i)=(14*k*grad_T*l*(r_fin+r_fin_out(i))/2
);
    Qpcm(i)=Qin(i)-Qhx(i);
    dVdt(i)=Qpcm(i)/(ice_density*Hfus);
%     drdt(i)=(Qin(i)-
Qhx(i))/(ice_density*l*r_flow(i)*2*pi*Hfus);
    dflow_min_dt(i)=dVdt(i)/(l*pi);
%
Qpcm(i)=(ice_density*l*2*pi*r_flow(i)*Hfus*d
rdt(i));

r_flow(i+1)=r_flow(i)+dflow_min_dt(i);
r_fin_out(i+1)=r_flow(i+1)-r_between;

dP_dt(i)=((r_tube^2)^2)/((r_flow(i)^2)^2);
```

```
end

hold on
plot((1:length(Qhx)),Qhx(:),'rX'),
title('Heat Load vs. Time'), ylabel('Qin
(W)');
hold on
plot((1:length(Qpcm)),Qpcm(:),'gX'),
title('Heat Load vs. Time'), ylabel('Qin
(W)')
axis([14354 30001 -1500 3000])
print -djpeg heat_load_vs_time

figure
plot((1:1:(1*length(r_flow_in))),r_flow_in(:
).*39.37,'rX'), title('Flow Radius vs.
Time'), ylabel('Flow_radius(in)');
axis([14354 30001 0 .93/2])
print -djpeg flow_radius_vs_time

hold on
plot((1:1:(1*length(r_flow_out))),r_flow_out
(:).*39.37,'bX'), title('Flow Radius vs.
Time'), ylabel('Flow_radius(in)');
axis([14354 30001 0 .93/2])
print -djpeg flow_radius_vs_time


figure
plot((1:1:(1*length(dP_dt))),dP_dt(:),'bX'),
title('Change in Pressure vs. Time'),
ylabel('Pressure Gradient');
axis([14354 30001 0 30])
print -djpeg pressure_gradient_vs_time

% figure
%
plot((1:1:(1*length(drdt))),drdt(:).*39.37,'
bX'), title('Change in Radius vs. Time'),
ylabel('Flow_radius change(in/sec)');
% print -djpeg change_in_flow_radius_vs_time

mass_flow=0.02519; %Use TDA value for 2700 W
HX
cp=4204; %Water
Tc=283; %Kelvin assume 10 deg C
Tsrhx=280; %Kelvin assume 7 deg C

%VARIABLE DELTA T AND M DOT. FOR REAL HX
PERFORMANCE

for i = 1:length(Qin)
    Th(i)=Tc+(Qin(i)/(mass_flow*cp));
    Th_celcius(i)=Th(i)-273;
    delta_T(i)=(Qin(i)/(mass_flow*cp));
    mass_flow_srhx(i)=Qin(i)/(cp*(Th(i)-
Tsrhx));
end

figure
plot((1:1:(1*length(Th))),(Th_celcius(:)),'b
X'), title('SRHX Inlet Tempeature (To=7 deg
C) vs. Time'), ylabel('Temperature(K)');
axis([14354 30001 20 40])
print -djpeg srhx_inlet_tempeature_vs_time

figure
plot((1:1:(1*length(mass_flow_srhx))),mass_f
low_srhx(:).*3600,'bX'), title('Mass Flow
Rate (max=90.7 kg/hr) through SRHX'),
ylabel('Mass Flow Rate (kg/hr)');
axis([14354 30001 0.015*3600 .025*3600])
print -djpeg srhx_flow_rate_vs_time

%TEST POINTS ASSUMING M DOT, DELTA T, OR T
WALL (GRAD T) IS CONSTANT

mdot=[.025194,0.025194*2,0.025194*4]; %4.54,
90.7, and 907 kg/hr

for i=1:3
    for j=1:length(Qin)
        Delta_T(i,j)=(Qin(j)/(mdot(i)*cp));
    end
end

figure
plot((1:length(Delta_T(1,:))),(Delta_T(1,:))
,'bX'), title('Delta_T vs. Time at 90.7
kg/hr'), ylabel('Temperature(K)');
print -djpeg delta_T_1

figure
plot((1:length(Delta_T(2,:))),(Delta_T(2,:))
,'rX'), title('Delta_T vs. Time at 90.7*2
kg/hr'), ylabel('Temperature(K)');
print -djpeg delta_T_2

figure
plot((1:length(Delta_T(3,:))),(Delta_T(3,:))
,'gX'), title('Delta_T vs. Time at 90.7*4
kg/hr'), ylabel('Temperature(K)');
print -djpeg delta_T_3

%%Keep Delta T as the constant variable

del_T=[4.0,7.1,17]; %All tested from the .75
in X 10.5 in HX

for i=1:3
    for j=1:length(Qin)

flow_rate(i,j)=(Qin(j)/(del_T(i)*cp));
    end
end
%
% figure
%
plot((1:length(flow_rate(1,:))),(flow_rate(1
,:).*(3600)),'bX'), title('Mass flow rate
vs. Time at 4.0 K delta T'),
ylabel('Mdot(kg/hr)');
% print -djpeg mass_flow_1
%
figure
plot((1:length(flow_rate(2,:))),(flow_rate(2
,:).*(3600)),'rX'), title('Mass flow rate
vs. Time at 7.1 K delta T'),
ylabel('Mdot(kg/hr)');
print -djpeg mass_flow_2
%
% figure
%
plot((1:length(flow_rate(3,:))),(flow_rate(3
,:).*(3600)),'gX'), title('Mass flow rate
vs. Time at 17 K delta T'),
ylabel('Mdot(kg/hr)');
% print -djpeg mass_flow_3
```

```
%Find amount of ice necessary for Qrad=Qavg          w/ PCM buffer
```

Overall Heat Transfer Coefficient Comparison

```
As_max=.047/10;

mu=.001002;
dens=1000;
D=.0254;
cp=4204;
k_fin=167;
k_tube=167;
k=(k_fin+k_tube)/2;
L=.3048;
x_tube=.000889;
r_fin=.00762;
n_fins=6;

Pr=(cp*mu)/k;
Re=[25.1 50.2 75.3];
Ti=[15+273 20+273 25+273];

%Equations
for i=1:length(Re)
    for j=1:length(Ti);
        Ra(i)=(11.76*Re(i))^2.198;

h_fin=(k_fin/L)*(0.825+(.387*(Ra(i)^(1/6)))/
((1+(.492/Pr)^(9/16))^(8/27)))^2;
        h_tube=2*k_tube/((D-
x_tube)*log(D/(D-x_tube)));
        h=1/(1/h_fin+1/h_tube);
        To1(i,j)=Ti(j)-(k*(Ti(j)-
273))/(n_fins*r_fin*h);
    end
end

Q=[1190.1 2133.5 2463.7];
Tw=[-20+273 -40+273 -80+273];
mdot=[.025194 .050389 .100779];

            %Ti1, mdot1

h_fin=(k_fin/L)*(0.825+(.387*(Ra(1)^(1/6)))/
((1+(.492/Pr)^(9/16))^(8/27)))^2;
            h_tube=2*k_tube/((D-
x_tube)*log(D/(D-x_tube)));
            h=1/(1/h_fin+1/h_tube);

Const1=((Q(1)/528)^(1/2.33))/(mdot(1)*cp/h);
            for m=1:250000
                To=m/100+273;
                Const2=(Ti(1)-
To)/log((Ti(1)-Tw(1))/(To-Tw(1)));
                if Const2 > Const1
                    To111=To
                    break
                end
            end


h_fin=(k_fin/L)*(0.825+(.387*(Ra(1)^(1/6)))/
((1+(.492/Pr)^(9/16))^(8/27)))^2;
            h_tube=2*k_tube/((D-
x_tube)*log(D/(D-x_tube)));
            h=1/(1/h_fin+1/h_tube)

Const1=((Q(1)/528)^(1/2.33))/(mdot(1)*cp/h);
            for m=1:25000
                To=m/100+273;
                Const2=(Ti(1)-
To)/log((Ti(1)-Tw(2))/(To-Tw(2)));
                if Const2 > Const1
                    To112=To
                    break
                end
            end


h_fin=(k_fin/L)*(0.825+(.387*(Ra(1)^(1/6)))/
((1+(.492/Pr)^(9/16))^(8/27)))^2;
            h_tube=2*k_tube/((D-
x_tube)*log(D/(D-x_tube)));
            h=1/(1/h_fin+1/h_tube);

Const1=((Q(1)/528)^(1/2.33))/(mdot(1)*cp/h);
            for m=1:25000
                To=m/100+273;
                Const2=(Ti(1)-
To)/log((Ti(1)-Tw(3))/(To-Tw(3)));
                if Const2 > Const1
                    To113=To
                    break
                end
            end

            %Ti1, mdot2

h_fin=(k_fin/L)*(0.825+(.387*(Ra(2)^(1/6)))/
((1+(.492/Pr)^(9/16))^(8/27)))^2;
            h_tube=2*k_tube/((D-
x_tube)*log(D/(D-x_tube)));
            h=1/(1/h_fin+1/h_tube);

Const1=((Q(1)/528)^(1/2.33))/(mdot(2)*cp/h);
            for m=1:250000
                To=m/100+273;
                Const2=(Ti(1)-
To)/log((Ti(1)-Tw(1))/(To-Tw(1)));
                if Const2 > Const1
                    To121=To
                    break
                end
            end


h_fin=(k_fin/L)*(0.825+(.387*(Ra(2)^(1/6)))/
((1+(.492/Pr)^(9/16))^(8/27)))^2;
            h_tube=2*k_tube/((D-
x_tube)*log(D/(D-x_tube)));
            h=1/(1/h_fin+1/h_tube)

Const1=((Q(1)/528)^(1/2.33))/(mdot(2)*cp/h);
            for m=1:25000
                To=m/100+273;
                Const2=(Ti(1)-
To)/log((Ti(1)-Tw(2))/(To-Tw(2)));
                if Const2 > Const1
                    To122=To
                    break
                end
            end
```

```
h_fin=(k_fin/L)*(0.825+(.387*(Ra(2)^(1/6)))/
((1+(.492/Pr)^(9/16))^(8/27)))^2;
            h_tube=2*k_tube/((D-
x_tube)*log(D/(D-x_tube)));
            h=1/(1/h_fin+1/h_tube);

Const1=((Q(1)/528)^(1/2.33))/(mdot(2)*cp/h);
            for m=1:25000
                To=m/100+273;
                Const2=(Ti(1)-
To)/log((Ti(1)-Tw(3))/(To-Tw(3)));
                if Const2 > Const1
                    To123=To
                    break
                end
            end

            %Ti1, mdot3

h_fin=(k_fin/L)*(0.825+(.387*(Ra(3)^(1/6)))/
((1+(.492/Pr)^(9/16))^(8/27)))^2;
            h_tube=2*k_tube/((D-
x_tube)*log(D/(D-x_tube)));
            h=1/(1/h_fin+1/h_tube);

Const1=((Q(1)/528)^(1/2.33))/(mdot(3)*cp/h);
            for m=1:250000
                To=m/100+273;
                Const2=(Ti(1)-
To)/log((Ti(1)-Tw(1))/(To-Tw(1)));
                if Const2 > Const1
                    To131=To
                    break
                end
            end


h_fin=(k_fin/L)*(0.825+(.387*(Ra(3)^(1/6)))/
((1+(.492/Pr)^(9/16))^(8/27)))^2;
            h_tube=2*k_tube/((D-
x_tube)*log(D/(D-x_tube)));
            h=1/(1/h_fin+1/h_tube)

Const1=((Q(1)/528)^(1/2.33))/(mdot(3)*cp/h);
            for m=1:25000
                To=m/100+273;
                Const2=(Ti(1)-
To)/log((Ti(1)-Tw(2))/(To-Tw(2)));
                if Const2 > Const1
                    To132=To
                    break
                end
            end


h_fin=(k_fin/L)*(0.825+(.387*(Ra(3)^(1/6)))/
((1+(.492/Pr)^(9/16))^(8/27)))^2;
            h_tube=2*k_tube/((D-
x_tube)*log(D/(D-x_tube)));
            h=1/(1/h_fin+1/h_tube);

Const1=((Q(1)/528)^(1/2.33))/(mdot(3)*cp/h);
            for m=1:25000
                To=m/100+273;
                Const2=(Ti(1)-
To)/log((Ti(1)-Tw(3))/(To-Tw(3)));
                if Const2 > Const1
                    To133=To
                    break
                end
            end

%%%%%%%%%%%%%%%%%%%%%%%%%%%%%%%%%%%%%%%%%%%%%%%%
%%%%%%%%%%%%

            %Ti1, mdot1

h_fin=(k_fin/L)*(0.825+(.387*(Ra(1)^(1/6)))/
((1+(.492/Pr)^(9/16))^(8/27)))^2;
            h_tube=2*k_tube/((D-
x_tube)*log(D/(D-x_tube)));
            h=1/(1/h_fin+1/h_tube);

Const1=((Q(1)/2524)^(1/1.332))/(mdot(1)*cp/h
);
            for m=1:250000
                To=m/100+273;
                Const2=(Ti(1)-
To)/log((Ti(1)-Tw(1))/(To-Tw(1)));
                if Const2 > Const1
                    To111=To
                    break
                end
            end


h_fin=(k_fin/L)*(0.825+(.387*(Ra(1)^(1/6)))/
((1+(.492/Pr)^(9/16))^(8/27)))^2;
            h_tube=2*k_tube/((D-
x_tube)*log(D/(D-x_tube)));
            h=1/(1/h_fin+1/h_tube)

Const1=((Q(1)/2524)^(1/1.33))/(mdot(1)*cp/h)
;
            for m=1:25000
                To=m/100+273;
                Const2=(Ti(1)-
To)/log((Ti(1)-Tw(2))/(To-Tw(2)));
                if Const2 > Const1
                    To112=To
                    break
                end
            end


h_fin=(k_fin/L)*(0.825+(.387*(Ra(1)^(1/6)))/
((1+(.492/Pr)^(9/16))^(8/27)))^2;
            h_tube=2*k_tube/((D-
x_tube)*log(D/(D-x_tube)));
            h=1/(1/h_fin+1/h_tube);

Const1=((Q(1)/2524)^(1/1.33))/(mdot(1)*cp/h)
;
            for m=1:25000
                To=m/100+273;
                Const2=(Ti(1)-
To)/log((Ti(1)-Tw(3))/(To-Tw(3)));
                if Const2 > Const1
                    To113=To
                    break
                end
            end

            %Ti1, mdot2

h_fin=(k_fin/L)*(0.825+(.387*(Ra(2)^(1/6)))/
((1+(.492/Pr)^(9/16))^(8/27)))^2;
            h_tube=2*k_tube/((D-
x_tube)*log(D/(D-x_tube)));
            h=1/(1/h_fin+1/h_tube);
```

```
Const1=((Q(1)/2524)^(1/1.33))/(mdot(2)*cp/h)
;
            for m=1:250000
                To=m/100+273;
                Const2=(Ti(1)-
To)/log((Ti(1)-Tw(1))/(To-Tw(1)));
                if Const2 > Const1
                    To121=To
                    break
                end
            end


h_fin=(k_fin/L)*(0.825+(.387*(Ra(2)^(1/6)))/
((1+(.492/Pr)^(9/16))^(8/27)))^2;
            h_tube=2*k_tube/((D-
x_tube)*log(D/(D-x_tube)));
            h=1/(1/h_fin+1/h_tube)

Const1=((Q(1)/2524)^(1/1.33))/(mdot(2)*cp/h)
;
            for m=1:25000
                To=m/100+273;
                Const2=(Ti(1)-
To)/log((Ti(1)-Tw(2))/(To-Tw(2)));
                if Const2 > Const1
                    To122=To
                    break
                end
            end


h_fin=(k_fin/L)*(0.825+(.387*(Ra(2)^(1/6)))/
((1+(.492/Pr)^(9/16))^(8/27)))^2;
            h_tube=2*k_tube/((D-
x_tube)*log(D/(D-x_tube)));
            h=1/(1/h_fin+1/h_tube);

Const1=((Q(1)/2524)^(1/1.33))/(mdot(2)*cp/h)
;
            for m=1:25000
                To=m/100+273;
                Const2=(Ti(1)-
To)/log((Ti(1)-Tw(3))/(To-Tw(3)));
                if Const2 > Const1
                    To123=To
                    break
                end
            end

            %Ti1, mdot3

h_fin=(k_fin/L)*(0.825+(.387*(Ra(3)^(1/6)))/
((1+(.492/Pr)^(9/16))^(8/27)))^2;
            h_tube=2*k_tube/((D-
x_tube)*log(D/(D-x_tube)));
            h=1/(1/h_fin+1/h_tube);

Const1=((Q(1)/2524)^(1/1.33))/(mdot(3)*cp/h)
;
            for m=1:250000
                To=m/100+273;
                Const2=(Ti(1)-
To)/log((Ti(1)-Tw(1))/(To-Tw(1)));
                if Const2 > Const1
                    To131=To
                    break
                end
            end


h_fin=(k_fin/L)*(0.825+(.387*(Ra(3)^(1/6)))/
((1+(.492/Pr)^(9/16))^(8/27)))^2;
            h_tube=2*k_tube/((D-
x_tube)*log(D/(D-x_tube)));
            h=1/(1/h_fin+1/h_tube)

Const1=((Q(1)/2524)^(1/1.33))/(mdot(3)*cp/h)
;
            for m=1:25000
                To=m/100+273;
                Const2=(Ti(1)-
To)/log((Ti(1)-Tw(2))/(To-Tw(2)));
                if Const2 > Const1
                    To132=To
                    break
                end
            end


h_fin=(k_fin/L)*(0.825+(.387*(Ra(3)^(1/6)))/
((1+(.492/Pr)^(9/16))^(8/27)))^2;
            h_tube=2*k_tube/((D-
x_tube)*log(D/(D-x_tube)));
            h=1/(1/h_fin+1/h_tube);

Const1=((Q(1)/2524)^(1/1.33))/(mdot(3)*cp/h)
;
            for m=1:25000
                To=m/100+273;
                 Const2(m)=(Ti(1)-
To)/log((Ti(1)-Tw(3))/(To-Tw(3)));
%                   if Const2 > Const1
%                       To133=To
%                       break
%                   end
            end

            plot(1:length(To),Const2(1:m))
```

Outlet Temperature and Pressure Difference Calculations

```
clc

As_max=.047;

g=9.81;
mu=.001002;
dens=1000;
v=mu/dens;
D=.0254;
cp=4204;
k_fin=167;
k_tube=167;
k=(k_fin+k_tube)/2;
L=.3048;
x_tube=.000889;
r_fin=.00762;
n_fins=6;
A_max=pi*(D/2)^2;
A_min=pi*(r_fin/2)^2;
A_diff=A_max-A_min;

Pr=(cp*mu)/k;
```

```
Re=[25.1 50.2 75.3];
%Re=[45 90 135];
Ti=[15+273 20+273 25+273];

Q=[1190.1 2133.5 2463.7];
Tw=[-20+273 -40+273 -80+273];
mdot=[.025194 .050389 .100779];

As2(:,:,1)=[0.02585 0.0282 0.03055; 0.0282
0.03055 0.0329; 0.0329 0.03525 0.0376];
As2(:,:,2)=[0.02115 0.0235 0.02585; 0.02535
0.02585 0.0282; 0.0282 0.03055 0.0329];
As2(:,:,3)=[0.01175 0.0141 0.01645; 0.0141
0.01645 0.0188; 0.0188 0.02115 0.0235];

%Equations
for i=1:length(Re)
    for j=1:length(Ti);
        for l=1:length(Tw);
        %Ra(i)=(11.76*Re(i))^2.198;
        B(j)=1/Ti(j);
        Grfin(i,j,l)=(g*B(j)*(Ti(i)-
Tw(l))*L^3)/(v^2);
        Grtube(i,j,l)=(g*B(j)*(Ti(i)-
Tw(l))*D^3)/(v^2);

Gr(i,j,l)=(1/Grfin(i,j,l)+1/Grtube(i,j,l))^-
1;
        Ra(i,j,l)=Gr(i,j,l)*Pr;

h_fin(i,j,l)=(k_fin/L)*(0.825+(.387*(Ra(i,j,
l)^(1/6)))/((1+(.492/Pr)^(9/16))^(8/27)))^2;
        h_tube=2*k_tube/((D-
x_tube)*log(D/(D-x_tube)));

h(i,j,l)=1/(1/h_fin(i,j,l)+1/h_tube);
        As1(i,j,l)=mdot(i)*cp/h(i,j,l);
        V1=mdot(i)/(dens*A_max);

V2=mdot(i)/(dens*(((abs((As1(i,j,l)/As_max)*
.5-.5*As_max))*A_diff/.5)+A_min));
        DP1(i,j,l)=dens*(V1^2-V2^2)/2;
        To1(i,j,l)=Ti(j)-(k*(Ti(j)-((Tw(l)-
273)*(As2(i,j,l)))/As_max+273)))/(r_fin*n_fin
s*2*h(i,j,l)*2)-273;
        end
    end
end

Tw=[-20+273 -40+273 -80+273];

%%Tw=-20, mdot1
            %Ti1, mdot1
            for m=1:250000
                To=Ti(1)-m/100;
                Const1=mdot(1)*2*cp*(Ti(1)-
To);
                As=mdot(1)*cp/h(1);

Const2=528*(As_max*(.55)*(Ti(1)-
To)/log((Ti(1)-Tw(1))/(To-Tw(1))))^2.33;
                V1=mdot(1)/(dens*A_max);
                V2=mdot(1)/(dens*(((.55-
.5)*A_diff/.5)+A_min));
                DP111=dens*(V1^2-V2^2)/2;
                if Const2 - Const1 < .001
                    To111=To;
                    break
                end
            end
            %Ti2, mdot1
            for m=1:250000
                To=Ti(2)-m/100;
                Const1=mdot(1)*2*cp*(Ti(2)-
To);
                As=mdot(1)*cp/h(1);

Const2=528*(As_max*(.6)*(Ti(2)-
To)/log((Ti(2)-Tw(1))/(To-Tw(1))))^2.33;
                V1=mdot(1)/(dens*A_max);
                V2=mdot(1)/(dens*(((.6-
.5)*A_diff/.5)+A_min));
                DP112=dens*(V1^2-V2^2)/2;
                if Const2 - Const1 < .001
                    To112=To;
                    break
                end
            end

            %Ti3, mdot1
            for m=1:250000
                To=Ti(3)-m/100;
                Const1=mdot(1)*2*cp*(Ti(3)-
To);
                As=mdot(1)*cp/h(1);

Const2=528*(As_max*(.65)*(Ti(3)-
To)/log((Ti(3)-Tw(1))/(To-Tw(1))))^2.33;
                V1=mdot(1)/(dens*A_max);
                V2=mdot(1)/(dens*(((.65-
.5)*A_diff/.5)+A_min));
                DP113=dens*(V1^2-V2^2)/2;
                if Const2 - Const1 < .001
                    To113=To;
                    break
                end
            end

%%Tw=-20, mdot2
            %Ti1
            for m=1:250000
                To=Ti(1)-m/100;
                Const1=mdot(2)*2*cp*(Ti(1)-
To);
                As=mdot(2)*cp/h(2);

Const2=528*(As_max*(.6)*(Ti(1)-
To)/log((Ti(1)-Tw(1))/(To-Tw(1))))^2.33;
                V1=mdot(2)/(dens*A_max);
                V2=mdot(2)/(dens*(((.6-
.5)*A_diff/.5)+A_min));
                DP121=dens*(V1^2-V2^2)/2;
                if Const2 - Const1 < .001
                    To121=To;
                    break
                end
            end

            %Ti2
            for m=1:250000
                To=Ti(2)-m/100;
                Const1=mdot(2)*2*cp*(Ti(2)-
To);
                As=mdot(2)*cp/h(2);

Const2=528*(As_max*(.65)*(Ti(2)-
To)/log((Ti(2)-Tw(1))/(To-Tw(1))))^2.33;
                V1=mdot(2)/(dens*A_max);
                V2=mdot(2)/(dens*(((.65-
.5)*A_diff/.5)+A_min));
                DP122=dens*(V1^2-V2^2)/2;
```

```
                if Const2 - Const1 < .001
                    To122=To;
                    break
                end
            end

            %Ti3
            for m=1:250000
                To=Ti(3)-m/100;
                Const1=mdot(2)*2*cp*(Ti(3)-
To);
                As=mdot(2)*cp/h(2);

Const2=528*(As_max*(.7)*(Ti(3)-
To)/log((Ti(3)-Tw(1))/(To-Tw(1))))^2.33;
                V1=mdot(2)/(dens*A_max);
                V2=mdot(2)/(dens*(((.7-
.5)*A_diff/.5)+A_min));
                DP123=dens*(V1^2-V2^2)/2;
                if Const2 - Const1 < .001
                    To123=To;
                    break
                end
            end

%%Tw=-20, mdot3
            %Ti1
            for m=1:250000
                To=Ti(1)-m/100;
                Const1=mdot(3)*2*cp*(Ti(1)-
To);
                As=mdot(3)*cp/h(3);

Const2=528*(As_max*(.7)*(Ti(1)-
To)/log((Ti(1)-Tw(1))/(To-Tw(1))))^2.33;
                V1=mdot(3)/(dens*A_max);
                V2=mdot(3)/(dens*(((.7-
.5)*A_diff/.5)+A_min));
                DP131=dens*(V1^2-V2^2)/2;
                if Const2 - Const1 < .001
                    To131=To;
                    break
                end
            end

            %Ti2
            for m=1:250000
                To=Ti(2)-m/100;
                Const1=mdot(3)*2*cp*(Ti(2)-
To);
                As=mdot(3)*cp/h(3);

Const2=528*(As_max*(.75)*(Ti(2)-
To)/log((Ti(2)-Tw(1))/(To-Tw(1))))^2.33;
                V1=mdot(3)/(dens*A_max);
                V2=mdot(3)/(dens*(((.75-
.5)*A_diff/.5)+A_min));
                DP132=dens*(V1^2-V2^2)/2;
                if Const2 - Const1 < .001
                    To132=To;
                    break
                end
            end

            %Ti3
            for m=1:250000
                To=Ti(3)-m/100;
                Const1=mdot(3)*2*cp*(Ti(3)-
To);
                As=mdot(3)*cp/h(3);

Const2=528*(As_max*(.8)*(Ti(3)-
To)/log((Ti(3)-Tw(1))/(To-Tw(1))))^2.33;
                V1=mdot(3)/(dens*A_max);
                V2=mdot(3)/(dens*(((.8-
.5)*A_diff/.5)+A_min));
                DP133=dens*(V1^2-V2^2)/2;
                if Const2 - Const1 < .001
                    To133=To;
                    break
                end
            end

To1_1wall=[To111,To112,To113;
           To121,To122,To123;
           To131,To132,To133]

DP1_1wall=[DP111,DP112,DP113;
           DP121,DP122,DP123;
           DP131,DP132,DP133]

%%Tw=-40, mdot1
            %Ti1
            for m=1:250000
                To=Ti(1)-m/100;
                Const1=mdot(1)*2*cp*(Ti(1)-
To);

Const2=528*(As_max*(.45)*(Ti(1)-
To)/log((Ti(1)-Tw(2))/(To-Tw(2))))^2.33;
                V1=mdot(1)/(dens*A_max);
                V2=mdot(1)/(dens*(((.55-
.5)*A_diff/.5)+A_min));
                DP211=dens*(V1^2-V2^2)/2;
                if Const2 - Const1 < .001
                    To211=To;
                    break
                end
            end

            %Ti2, mdot1
            for m=1:250000
                To=Ti(2)-m/100;
                Const1=mdot(1)*2*cp*(Ti(2)-
To);

Const2=528*(As_max*(.5)*(Ti(2)-
To)/log((Ti(2)-Tw(2))/(To-Tw(2))))^2.33;
                V1=mdot(1)/(dens*A_max);
                V2=mdot(1)/(dens*(((.5-
.5)*A_diff/.5)+A_min));
                DP212=dens*(V1^2-V2^2)/2;
                if Const2 - Const1 < .001
                    To212=To;
                    break
                end
            end

            %Ti3, mdot1
            for m=1:250000
                To=Ti(3)-m/100;
                Const1=mdot(1)*2*cp*(Ti(3)-
To);

Const2=528*(As_max*(.55)*(Ti(3)-
To)/log((Ti(3)-Tw(2))/(To-Tw(2))))^2.33;
                V1=mdot(1)/(dens*A_max);
                V2=mdot(1)/(dens*(((.55-
.5)*A_diff/.5)+A_min));
                DP213=dens*(V1^2-V2^2)/2;
                if Const2 - Const1 < .001
```

```
                    To213=To;
                    break
                end
            end

%%Tw=-40, mdot2
            %Ti1
            for m=1:250000
                To=Ti(1)-m/100;
                Const1=mdot(2)*2*cp*(Ti(1)-
To);

Const2=528*(As_max*(.5)*(Ti(1)-
To)/log((Ti(1)-Tw(2))/(To-Tw(2))))^2.33;
                V1=mdot(2)/(dens*A_max);
                V2=mdot(2)/(dens*(((.5-
.5)*A_diff/.5)+A_min));
                DP221=dens*(V1^2-V2^2)/2;
                if Const2 - Const1 < .001
                    To221=To;
                    break
                end
            end

            %Ti2
            for m=1:250000
                To=Ti(2)-m/100;
                Const1=mdot(2)*2*cp*(Ti(2)-
To);

Const2=528*(As_max*(.55)*(Ti(2)-
To)/log((Ti(2)-Tw(2))/(To-Tw(2))))^2.33;
                V1=mdot(2)/(dens*A_max);
                V2=mdot(2)/(dens*(((.55-
.5)*A_diff/.5)+A_min));
                DP222=dens*(V1^2-V2^2)/2;
                if Const2 - Const1 < .001
                    To222=To;
                    break
                end
            end

            %Ti3
            for m=1:250000
                To=Ti(3)-m/100;
                Const1=mdot(2)*2*cp*(Ti(3)-
To);

Const2=528*(As_max*(.60)*(Ti(3)-
To)/log((Ti(3)-Tw(2))/(To-Tw(2))))^2.33;
                V1=mdot(2)/(dens*A_max);
                V2=mdot(2)/(dens*(((.6-
.5)*A_diff/.5)+A_min));
                DP223=dens*(V1^2-V2^2)/2;
                if Const2 - Const1 < .001
                    To223=To;
                    break
                end
            end

%%Tw=-40, mdot3
            %Ti1
            for m=1:250000
                To=Ti(1)-m/100;
                Const1=mdot(3)*2*cp*(Ti(1)-
To);

Const2=528*(As_max*(.6)*(Ti(1)-
To)/log((Ti(1)-Tw(2))/(To-Tw(2))))^2.33;
                V1=mdot(3)/(dens*A_max);
                V2=mdot(3)/(dens*(((.6-
.5)*A_diff/.5)+A_min));
                DP231=dens*(V1^2-V2^2)/2;
                if Const2 - Const1 < .001
                    To231=To;
                    break
                end
            end

            %Ti2
            for m=1:250000
                To=Ti(2)-m/100;
                Const1=mdot(3)*2*cp*(Ti(2)-
To);

Const2=528*(As_max*(.65)*(Ti(2)-
To)/log((Ti(2)-Tw(2))/(To-Tw(2))))^2.33;
                V1=mdot(3)/(dens*A_max);
                V2=mdot(3)/(dens*(((.65-
.5)*A_diff/.5)+A_min));
                DP232=dens*(V1^2-V2^2)/2;
                if Const2 - Const1 < .001
                    To232=To;
                    break
                end
            end

            %Ti3
            for m=1:250000
                To=Ti(3)-m/100;
                Const1=mdot(3)*2*cp*(Ti(3)-
To);

Const2=528*(As_max*(.7)*(Ti(3)-
To)/log((Ti(3)-Tw(2))/(To-Tw(2))))^2.33;
                V1=mdot(3)/(dens*A_max);
                V2=mdot(3)/(dens*(((.7-
.5)*A_diff/.5)+A_min));
                DP233=dens*(V1^2-V2^2)/2;
                if Const2 - Const1 < .001
                    To233=To;
                    break
                end
            end

To1_2wall=[To211,To212,To213;
           To221,To222,To223;
           To231,To232,To233]

DP1_2wall=[DP211,DP212,DP213;
           DP221,DP222,DP223;
           DP231,DP232,DP233]

%%Tw=-80, mdot1
             %Ti1
             for m=1:250000
                 To=Ti(1)-m/100;
                 Const1=mdot(1)*2*cp*(Ti(1)-
To);

Const2=528*(As_max*(.25)*(Ti(1)-
To)/log((Ti(1)-Tw(3))/(To-Tw(3))))^2.33;
                 V1=mdot(1)/(dens*A_max);
                 V2=mdot(1)/(dens*(((.75-
.5)*A_diff/.5)+A_min));
                 DP311=dens*(V1^2-V2^2)/2;
                 if Const2 - Const1 < .001
                     To311=To;
                     break
                 end
             end
```

```
            %Ti2, mdot1
            for m=1:250000
                To=Ti(2)-m/100;
                Const1=mdot(1)*2*cp*(Ti(2)-
To);

Const2=528*(As_max*(.3)*(Ti(2)-
To)/log((Ti(2)-Tw(3))/(To-Tw(3))))^2.33;
                V1=mdot(1)/(dens*A_max);
                V2=mdot(1)/(dens*(((.7-
.5)*A_diff/.5)+A_min));
                DP312=dens*(V1^2-V2^2)/2;
                if Const2 - Const1 < .001
                    To312=To;
                    break
                end
            end

            %Ti3, mdot1
            for m=1:250000
                To=Ti(3)-m/100;
                Const1=mdot(1)*2*cp*(Ti(3)-
To);

Const2=528*(As_max*(.35)*(Ti(3)-
To)/log((Ti(3)-Tw(3))/(To-Tw(3))))^2.33;
                V1=mdot(1)/(dens*A_max);
                V2=mdot(1)/(dens*(((.65-
.5)*A_diff/.5)+A_min));
                DP313=dens*(V1^2-V2^2)/2;
                if Const2 - Const1 < .001
                    To313=To;
                    break
                end
            end

%%Tw=-80, mdot2
            %Ti1
            for m=1:250000
                To=Ti(1)-m/100;
                Const1=mdot(2)*2*cp*(Ti(1)-
To);

Const2=528*(As_max*(.3)*(Ti(1)-
To)/log((Ti(1)-Tw(3))/(To-Tw(3))))^2.33;
                V1=mdot(2)/(dens*A_max);
                V2=mdot(2)/(dens*(((.7-
.5)*A_diff/.5)+A_min));
                DP321=dens*(V1^2-V2^2)/2;
                if Const2 - Const1 < .001
                    To321=To;
                    break
                end
            end

            %Ti2
            for m=1:250000
                To=Ti(2)-m/100;
                Const1=mdot(2)*2*cp*(Ti(2)-
To);

Const2=528*(As_max*(.35)*(Ti(2)-
To)/log((Ti(2)-Tw(3))/(To-Tw(3))))^2.33;
                V1=mdot(2)/(dens*A_max);
                V2=mdot(2)/(dens*(((.65-
.5)*A_diff/.5)+A_min));
                DP322=dens*(V1^2-V2^2)/2;
                if Const2 - Const1 < .001
                    To322=To;
                    break
                end
            end

            %Ti3
            for m=1:250000
                To=Ti(3)-m/100;
                Const1=mdot(2)*2*cp*(Ti(3)-
To);

Const2=528*(As_max*(.4)*(Ti(3)-
To)/log((Ti(3)-Tw(3))/(To-Tw(3))))^2.33;
                V1=mdot(2)/(dens*A_max);
                V2=mdot(2)/(dens*(((.6-
.5)*A_diff/.5)+A_min));
                DP323=dens*(V1^2-V2^2)/2;
                if Const2 - Const1 < .001
                    To323=To;
                    break
                end
            end

%%Tw=-80, mdot3
            %Ti1
            for m=1:250000
                To=Ti(1)-m/100;
                Const1=mdot(3)*2*cp*(Ti(1)-
To);

Const2=528*(As_max*(.4)*(Ti(1)-
To)/log((Ti(1)-Tw(3))/(To-Tw(3))))^2.33;
                V1=mdot(3)/(dens*A_max);
                V2=mdot(3)/(dens*(((.6-
.5)*A_diff/.5)+A_min));
                DP331=dens*(V1^2-V2^2)/2;
                if Const2 - Const1 < .001
                    To331=To;
                    break
                end
            end

            %Ti2
            for m=1:250000
                To=Ti(2)-m/100;
                Const1=mdot(3)*2*cp*(Ti(2)-
To);

Const2=528*(As_max*(.45)*(Ti(2)-
To)/log((Ti(2)-Tw(3))/(To-Tw(3))))^2.33;
                V1=mdot(3)/(dens*A_max);
                V2=mdot(3)/(dens*(((.55-
.5)*A_diff/.5)+A_min));
                DP332=dens*(V1^2-V2^2)/2;
                if Const2 - Const1 < .001
                    To332=To;
                    break
                end
            end

            %Ti3
            for m=1:250000
                To=Ti(3)-m/100;
                Const1=mdot(3)*2*cp*(Ti(3)-
To);

Const2=528*(As_max*(.5)*(Ti(3)-
To)/log((Ti(3)-Tw(3))/(To-Tw(3))))^2.33;
                V1=mdot(3)/(dens*A_max);
                V2=mdot(3)/(dens*(((.5-
.5)*A_diff/.5)+A_min));
                DP333=dens*(V1^2-V2^2)/2;
                if Const2 - Const1 < .001
```

```
                    To333=To;
                    break
                end
            end

To1_3wall=[To311,To312,To313;
           To321,To322,To323;
           To331,To332,To333]

DP1_3wall=[DP311,DP312,DP313;
           DP321,DP322,DP323;
           DP331,DP332,DP333]

%%%%%%%%%%%%%%%%%%%%%%%%%%%%%%%%%%%%%%%%%%%%%%%%%%%%%%%%%%%%%%%%%%%%%%%%%%%%%%%%
%%%%%%%%%%%%%%%%%%%%%%%%
%%Tw=-20, mdot1
            %Ti1, mdot1
            for m=1:250000
                To=Ti(1)-m/100;
                Const1=mdot(1)*2*cp*(Ti(1)-
To);
                As=mdot(1)*cp/h(1);

Const2=2524*(As_max*(.55)*(Ti(1)-
To)/log((Ti(1)-Tw(1))/(To-Tw(1))))^1.33;
                if Const2 - Const1 < .001
                    To111=To;
                    break
                end
            end

            %Ti2, mdot1
            for m=1:250000
                To=Ti(2)-m/100;
                Const1=mdot(1)*2*cp*(Ti(2)-
To);
                As=mdot(1)*cp/h(1);

Const2=2524*(As_max*(.6)*(Ti(2)-
To)/log((Ti(2)-Tw(1))/(To-Tw(1))))^1.33;
                if Const2 - Const1 < .001
                    To112=To;
                    break
                end
            end

            %Ti3, mdot1
            for m=1:250000
                To=Ti(3)-m/100;
                Const1=mdot(1)*2*cp*(Ti(3)-
To);
                As=mdot(1)*cp/h(1);

Const2=2524*(As_max*(.65)*(Ti(3)-
To)/log((Ti(3)-Tw(1))/(To-Tw(1))))^1.33;
                if Const2 - Const1 < .001
                    To113=To;
                    break
                end
            end

%%Tw=-20, mdot2
            %Ti1
            for m=1:250000
                To=Ti(1)-m/100;
                Const1=mdot(2)*2*cp*(Ti(1)-
To);
                As=mdot(2)*cp/h(2);

Const2=2524*(As_max*(.6)*(Ti(1)-
To)/log((Ti(1)-Tw(1))/(To-Tw(1))))^1.33;
                if Const2 - Const1 < .001
                    To121=To;
                    break
                end
            end

            %Ti2
            for m=1:250000
                To=Ti(2)-m/100;
                Const1=mdot(2)*2*cp*(Ti(2)-
To);
                As=mdot(2)*cp/h(2);

Const2=2524*(As_max*(.65)*(Ti(2)-
To)/log((Ti(2)-Tw(1))/(To-Tw(1))))^1.33;
                if Const2 - Const1 < .001
                    To122=To;
                    break
                end
            end

            %Ti3
            for m=1:250000
                To=Ti(3)-m/100;
                Const1=mdot(2)*2*cp*(Ti(3)-
To);
                As=mdot(2)*cp/h(2);

Const2=2524*(As_max*(.7)*(Ti(3)-
To)/log((Ti(3)-Tw(1))/(To-Tw(1))))^1.33;
                if Const2 - Const1 < .001
                    To123=To;
                    break
                end
            end

%%Tw=-20, mdot3
            %Ti1
            for m=1:250000
                To=Ti(1)-m/100;
                Const1=mdot(3)*2*cp*(Ti(1)-
To);
                As=mdot(3)*cp/h(3);

Const2=2524*(As_max*(.7)*(Ti(1)-
To)/log((Ti(1)-Tw(1))/(To-Tw(1))))^1.33;
                if Const2 - Const1 < .001
                    To131=To;
                    break
                end
            end

            %Ti2
            for m=1:250000
                To=Ti(2)-m/100;
                Const1=mdot(3)*2*cp*(Ti(2)-
To);
                As=mdot(3)*cp/h(3);

Const2=2524*(As_max*(.75)*(Ti(2)-
To)/log((Ti(2)-Tw(1))/(To-Tw(1))))^1.33;
                if Const2 - Const1 < .001
                    To132=To;
                    break
                end
            end

            %Ti3
            for m=1:250000
                To=Ti(3)-m/100;
```

```
                Const1=mdot(3)*2*cp*(Ti(3)-
To);
                As=mdot(3)*cp/h(3);

Const2=2524*(As_max*(.8)*(Ti(3)-
To)/log((Ti(3)-Tw(1))/(To-Tw(1))))^1.33;
                if Const2 - Const1 < .001
                    To133=To;
                    break
                end
            end

To2_1wall=[To111,To112,To113;
           To121,To122,To123;
           To131,To132,To133]

%%Tw=-40, mdot1
            %Ti1
            for m=1:250000
                To=Ti(1)-m/100;
                Const1=mdot(1)*2*cp*(Ti(1)-
To);

Const2=2524*(As_max*(.45)*(Ti(1)-
To)/log((Ti(1)-Tw(2))/(To-Tw(2))))^1.33;
                if Const2 - Const1 < .001
                    To211=To;
                    break
                end
            end

            %Ti2, mdot1
            for m=1:250000
                To=Ti(2)-m/100;
                Const1=mdot(1)*2*cp*(Ti(2)-
To);

Const2=2524*(As_max*(.5)*(Ti(2)-
To)/log((Ti(2)-Tw(2))/(To-Tw(2))))^1.33;
                if Const2 - Const1 < .001
                    To212=To;
                    break
                end
            end

            %Ti3, mdot1
            for m=1:250000
                To=Ti(3)-m/100;
                Const1=mdot(1)*2*cp*(Ti(3)-
To);

Const2=2524*(As_max*(.55)*(Ti(3)-
To)/log((Ti(3)-Tw(2))/(To-Tw(2))))^1.33;
                if Const2 - Const1 < .001
                    To213=To;
                    break
                end
            end

%%Tw=-40, mdot2
            %Ti1
            for m=1:250000
                To=Ti(1)-m/100;
                Const1=mdot(2)*2*cp*(Ti(1)-
To);

Const2=2524*(As_max*(.5)*(Ti(1)-
To)/log((Ti(1)-Tw(2))/(To-Tw(2))))^1.33;
                if Const2 - Const1 < .001
                    To221=To;
                    break
                end
            end

            %Ti2
            for m=1:250000
                To=Ti(2)-m/100;
                Const1=mdot(2)*2*cp*(Ti(2)-
To);

Const2=2524*(As_max*(.55)*(Ti(2)-
To)/log((Ti(2)-Tw(2))/(To-Tw(2))))^1.33;
                if Const2 - Const1 < .001
                    To222=To;
                    break
                end
            end

            %Ti3
            for m=1:250000
                To=Ti(3)-m/100;
                Const1=mdot(2)*2*cp*(Ti(3)-
To);

Const2=2524*(As_max*(.6)*(Ti(3)-
To)/log((Ti(3)-Tw(2))/(To-Tw(2))))^1.33;
                if Const2 - Const1 < .001
                    To223=To;
                    break
                end
            end

%%Tw=-40, mdot3
            %Ti1
            for m=1:250000
                To=Ti(1)-m/100;
                Const1=mdot(3)*2*cp*(Ti(1)-
To);

Const2=2524*(As_max*(.6)*(Ti(1)-
To)/log((Ti(1)-Tw(2))/(To-Tw(2))))^1.33;
                if Const2 - Const1 < .001
                    To231=To;
                    break
                end
            end

            %Ti2
            for m=1:250000
                To=Ti(2)-m/100;
                Const1=mdot(3)*2*cp*(Ti(2)-
To);

Const2=2524*(As_max*(.65)*(Ti(2)-
To)/log((Ti(2)-Tw(2))/(To-Tw(2))))^1.33;
                if Const2 - Const1 < .001
                    To232=To;
                    break
                end
            end

            %Ti3
            for m=1:250000
                To=Ti(3)-m/100;
                Const1=mdot(3)*2*cp*(Ti(3)-
To);

Const2=2524*(As_max*(.7)*(Ti(3)-
To)/log((Ti(3)-Tw(2))/(To-Tw(2))))^1.33;
                if Const2 - Const1 < .001
                    To233=To;
                    break
```

```
            end
        end

To2_2wall=[To211,To212,To213;
          To221,To222,To223;
          To231,To232,To233]

%%Tw=-80, mdot1
        %Ti1
        for m=1:250000
            To=Ti(1)-m/100;
            Const1=mdot(1)*2*cp*(Ti(1)-
To);

Const2=2524*(As_max*(.25)*(Ti(1)-
To)/log((Ti(1)-Tw(3))/(To-Tw(3))))^1.33;
            if Const2 - Const1 < .001
                To311=To;
                break
            end
        end

        %Ti2, mdot1
        for m=1:250000
            To=Ti(2)-m/100;
            Const1=mdot(1)*2*cp*(Ti(2)-
To);

Const2=2524*(As_max*(.3)*(Ti(2)-
To)/log((Ti(2)-Tw(3))/(To-Tw(3))))^1.33;
            if Const2 - Const1 < .001
                To312=To;
                break
            end
        end

        %Ti3, mdot1
        for m=1:250000
            To=Ti(3)-m/100;
            Const1=mdot(1)*2*cp*(Ti(3)-
To);

Const2=2524*(As_max*(.35)*(Ti(3)-
To)/log((Ti(3)-Tw(3))/(To-Tw(3))))^1.33;
            if Const2 - Const1 < .001
                To313=To;
                break
            end
        end

%%Tw=-80, mdot2
        %Ti1
        for m=1:250000
            To=Ti(1)-m/100;
            Const1=mdot(2)*2*cp*(Ti(1)-
To);

Const2=2524*(As_max*(.3)*(Ti(1)-
To)/log((Ti(1)-Tw(3))/(To-Tw(3))))^1.33;
            if Const2 - Const1 < .001
                To321=To;
                break
            end
        end

        %Ti2
        for m=1:250000
            To=Ti(2)-m/100;
            Const1=mdot(2)*2*cp*(Ti(2)-
To);

Const2=2524*(As_max*(.35)*(Ti(2)-
To)/log((Ti(2)-Tw(3))/(To-Tw(3))))^1.33;
            if Const2 - Const1 < .001
                To322=To;
                break
            end
        end

        %Ti3
        for m=1:250000
            To=Ti(3)-m/100;
            Const1=mdot(2)*2*cp*(Ti(3)-
To);

Const2=2524*(As_max*(.4)*(Ti(3)-
To)/log((Ti(3)-Tw(3))/(To-Tw(3))))^1.33;
            if Const2 - Const1 < .001
                To323=To;
                break
            end
        end

%%Tw=-80, mdot3
        %Ti1
        for m=1:250000
            To=Ti(1)-m/100;
            Const1=mdot(3)*2*cp*(Ti(1)-
To);

Const2=2524*(As_max*(.4)*(Ti(1)-
To)/log((Ti(1)-Tw(3))/(To-Tw(3))))^1.33;
            if Const2 - Const1 < .001
                To331=To;
                break
            end
        end

        %Ti2
        for m=1:250000
            To=Ti(2)-m/100;
            Const1=mdot(3)*2*cp*(Ti(2)-
To);

Const2=2524*(As_max*(.45)*(Ti(2)-
To)/log((Ti(2)-Tw(3))/(To-Tw(3))))^1.33;
            if Const2 - Const1 < .001
                To332=To;
                break
            end
        end

        %Ti3
        for m=1:250000
            To=Ti(3)-m/100;
            Const1=mdot(3)*2*cp*(Ti(3)-
To);

Const2=2524*(As_max*(.5)*(Ti(3)-
To)/log((Ti(3)-Tw(3))/(To-Tw(3))))^1.33;
            if Const2 - Const1 < .001
                To333=To;
                break
            end
        end

To2_3wall=[To311,To312,To313;
          To321,To322,To323;
          To331,To332,To333]

Twf=[3.8,-0.1,1.7;
```

```
    9.4,9.9,13.4;
    12.2,14.9,19.2]

for i=1:3
    for j=1:3
plot(1,Twf(i,j),'kx')
hold on
plot(2,Twf(i,j),'ko')
hold on
plot(3,Twf(i,j),'k*')
hold on
plot(4,To1(i,j,1),'rx')
hold on
plot(5,To1(i,j,2),'ro')
hold on
plot(6,To1(i,j,3),'r*')
hold on
plot(7,To1_1wall(i,j)-273,'bx')
hold on
plot(8,To1_2wall(i,j)-273,'bo')
hold on
plot(9,To1_3wall(i,j)-273,'b*')
hold on
plot(10,To2_1wall(i,j)-273,'gx')
hold on
plot(11,To2_2wall(i,j)-273,'go')
hold on
plot(12,To2_3wall(i,j)-273,'g*')
    end
end

title('Temperature Bounds for Each
Methodology')
xlabel('Test Set')
ylabel('Temperature (Celsius)')
```

APPENDIX B:
OVERALL HEAT TRANSFER COEFFICIENT COMPARISON

Fully_melted, Tin=15, Tw=-20

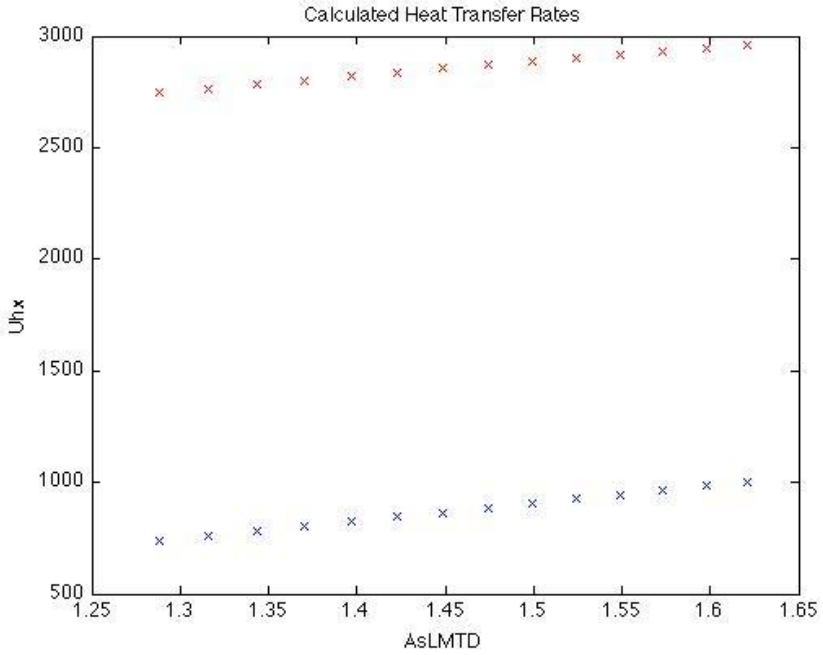

Half_melted, Tin=15, Tw=-20

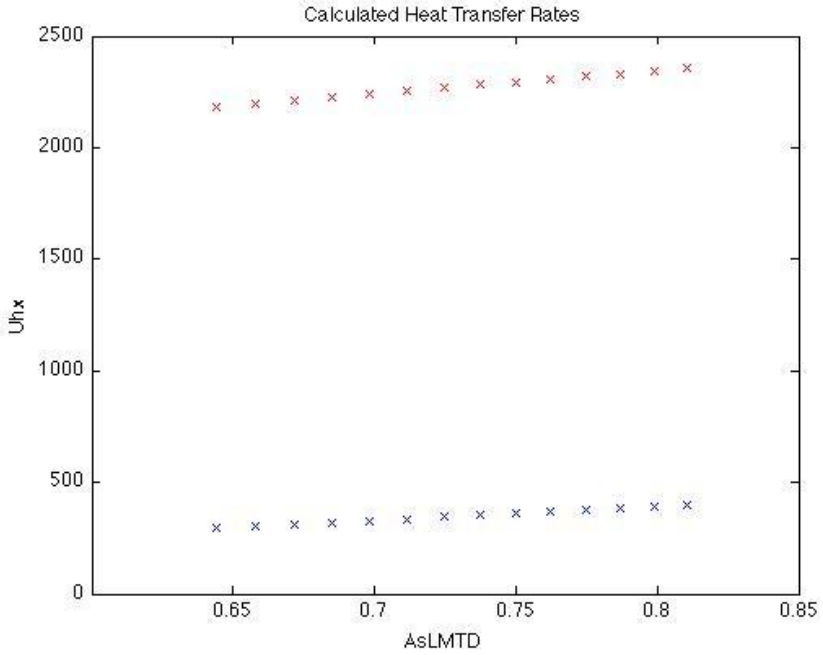

1/10 Max Area, Tin=15, Tw=-20

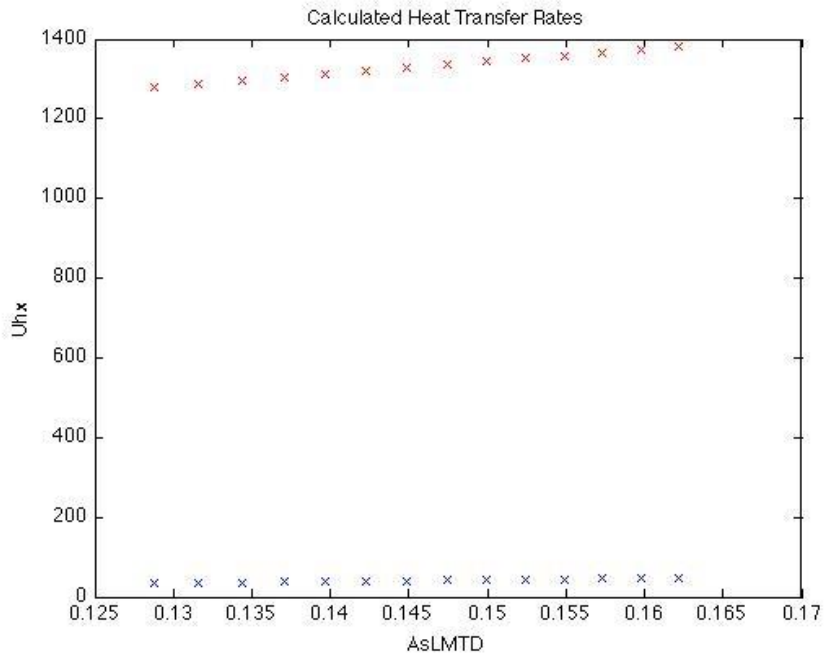

Fully melted, Tin=25, Tw=-80

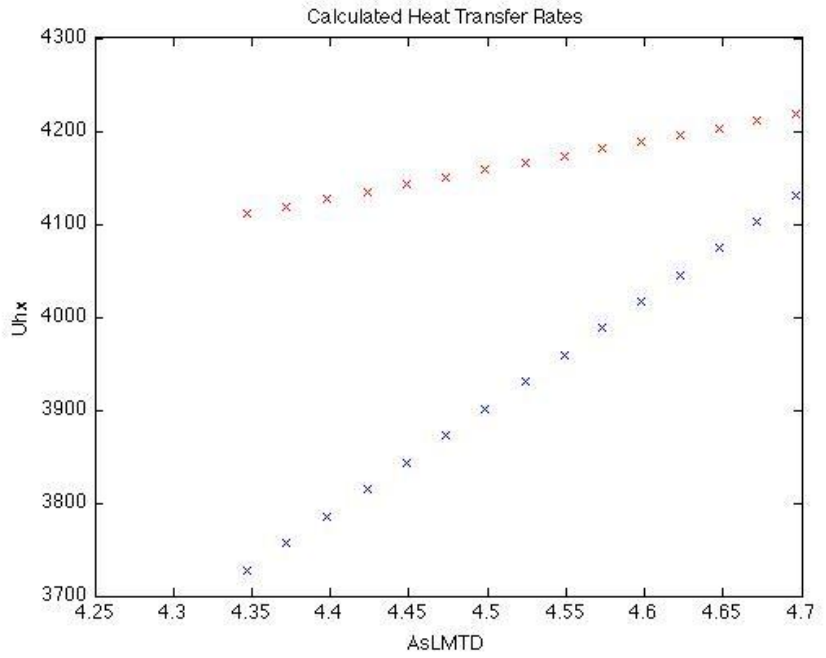

Half melted, Tin=25, Tw=-80

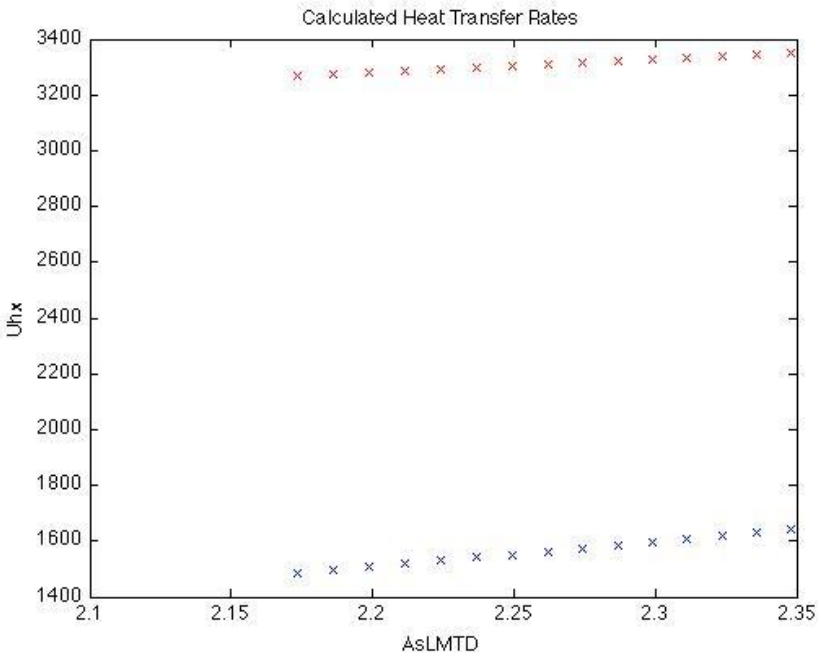

1/10 Max Area, Tin=25, Tw=-80

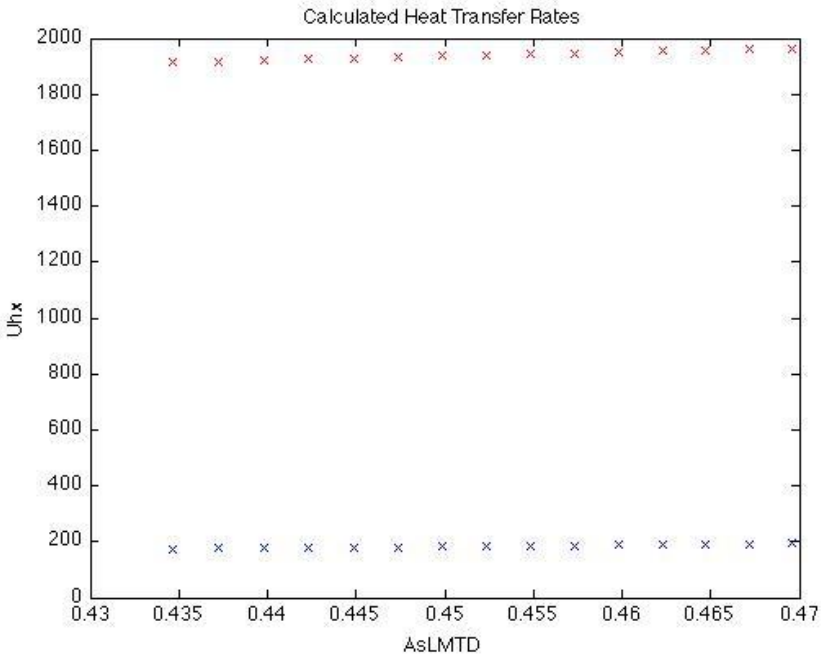

APPENDIX C:
VARIABLE DEFINITIONS AND UNCERTAINTIES

Table AC: Variable Definitions and Uncertainties

Variable	Description	Units	Measured, Controlled, Calculated, Given	Value	Uncertainty
m_{wf}	Mass flow rate of the working fluid (water) through the heat exchanger	kg/sec	Controlled	.02519/.05038/ .10077	.000333
T_{in}	Temperature moving into the heat exchanger	C	Controlled	15 / 20 / 25	0.15
T_{out}	Temperature moving out of the heat exchanger	C	Measured		0.15
c_p	Specific heat of liquid water	J/kg	Given	4204	20
Q_{wf}	Heat transferred from the working fluid	Watt	Calculated		2.6-12.3 %
T_{wall}	Temperature of the heat exchanger shell	C	Controlled	-20/-40/-80	2.2
A_s	Surface area of the heat exchanger exposed to the working fluid	m^2	Calculated		
Q_{hx}	Heat transferred to the heat exchanger	Watts	Calculated		5.7-27.5 %
ρ_{water}	Density of the water	kg/m^3	Given	1000	5
$R_{between}$	Distance between the fins in the heat exchanger	meters	Given	.0045	0.0001
R_{fins}	Length of the fins	meters	Given	.0073	0.0001
R_{in}	Cross sectional flow radius into the heat exchanger	meters	Calculated		20.7-31.7 %
R_{out}	Cross sectional flow radius out of the heat exchanger	meters	Calculated		20.7-31.7 %
A_{c_in}	Cross sectional area into the heat exchanger	m^2	Calculated		58.5-89.6 %
A_{c_out}	Cross sectional area out of the heat exchanger	m^2	Calculated		58.5-89.6 %
V_{in}	Velocity of water into the heat exchanger	m/s	Calculated		58.5-89.6 %
V_{out}	Velocity of water out of the heat exchanger	m/s	Calculated		58.5-89.6 %
ΔP	Change in pressure across the heat	psi	Measured		.0125

	exchanger				
V	Volumetric flow rate through the heat exchanger	L/s	Controlled		.000333
N_{fins}	Number of fins within the heat exchanger	unitless	Given	7	0
k	Thermal conductivity of the heat exchanger	W/m-K	Given	167	1
∇T	Temperature gradient	K/m	Calculated		1.29 %
l	Length of heat exchanger	m	Given	0.305	.001
m_{ice}	Melt or freeze rate of ice	kg/sec	Calculated		12.5-60.2 %
H_{fus}	Heat of fusion of water	J/kg	Given	334000	1000